Data-Driven Scanning Probe Microscopy for Understanding Carrier Dynamics in Lead Halide Perovskite Semiconductors

Madeleine D. Breshears

A dissertation

submitted in partial fulfillment of the

requirements for the degree of

Doctor of Philosophy

University of Washington

2025

Reading Committee:

David S. Ginger, Chair

Dan Fu

Cody Schlenker

Program Authorized to Offer Degree:

Department of Chemistry

University of Washington

Abstract

Data-Driven Scanning Probe Microscopy for Understanding Carrier Dynamics in Lead Halide Perovskite Semiconductors

Madeleine D. Breshears

Chair of the Supervisory Committee:
David Ginger
Department of Chemistry

Scanning probe microscopy (SPM) plays a pivotal role in advancing our understanding of semiconductor materials by enabling nanoscale characterization of structural and functional properties. Dynamic SPM techniques provide insight into transient charge carrier dynamics in semiconducting materials. Time-resolved electrostatic force microscopy (trEFM) is one such dynamic SPM method which measures nanoscale surface potential dynamics with high spatial and temporal resolution, providing information about key properties such as local photovoltaic quantum efficiency, electronic carrier recombination, and ion motion.

The multi-dimensional datasets obtained from trEFM—combining both spatial and temporal information—are ripe opportunities for the application of data science and machine learning (ML) techniques. The application of ML methods, such as neural networks, can significantly enhance the extraction of meaningful dynamics from noisy experimental data, allowing for a more accurate understanding of the spatial heterogeneity of electronic and ionic carrier phenomena.

In this work, we examine lead halide perovskites with trEFM. Lead halide perovskites are an exciting class of semiconducting materials with applications in photovoltaics, light emission, and radiation detection. Their ability to achieve high efficiencies, combined with solution-processability and defect tolerance, has led to rapid advancements in perovskite-based

optoelectronic devices. The performance of these materials is influenced by the intricate interplay between their crystallographic and morphological features, which often span from nanometers to micrometers in size. Using trEFM, we can gain detailed insights into how local changes in surface potential relate to the structural features of perovskite films, ultimately providing a deeper understanding of their optoelectronic behavior. We find that the surface recombination velocity, as modified by defect passivation, and defect-enabled ion motion are the primary factors that influence the spatial heterogeneity we observe in polycrystalline lead halide perovskite. We first present two ML models that enable advanced signal processing for trEFM dynamics, exemplifying the natural harmony between large-data dynamic SPM methods and machine learning. We then explore the factors (surface recombination velocity and ion motion) that govern the trEFM dynamics we observe. Overall, this work demonstrates how combining advanced SPM techniques with ML can significantly enhance our ability to study and optimize next-generation semiconductor materials.

Table of Contents

Chapter 1: Introduction

1.1 Scanning Probe Microscopy

A significant contribution to our understanding of semiconductor materials rests on the application of functional microscopy tools to spatially resolve heterogeneity in structure and function.[1–8] Indeed, disentangling the relationship between structure and function in semiconductors is critical to understanding and improving semiconductor thin films.[4–7,9–11] For example, methylammonium lead triiodide ($MAPbI_3$) exhibits heterogeneous morphological domains, often referred to as "grains." Using confocal photoluminescence (PL) microscopy, deQuilettes et al. found that different grains exhibited varied levels of PL brightness and different PL lifetimes, indicating that the heterogeneous structure of the thin film affected its performance.[7] Organic photovoltaics (OPVs) have also benefited from the application of microscopy to understand how polymer blends affect efficiencies.[1,12–14]

Confocal PL microscopy is a well-established technique for examining optoelectronic samples; however, because it is an optical microscopy technique, the spatial resolution is diffraction-limited.[4,10,15,16] With 405 nm excitation, for example, the highest reliable spatial resolution is approximately 280 nm with an objective that has a numerical aperture (NA) of 0.9. Higher NA objectives may improve this resolution, but ultimately the excitation wavelength limits the features we are able to reliably resolve. As such, when we want to image below the diffraction limit, we must turn to alternative microscopy techniques. Cathodoluminescence (CL) microscopy can resolve nanoscale features and corresponding functional properties such as charge carrier dynamics, but it risks damaging particularly sensitive materials with the electron beam.[5,17,18] Nanoscale X-ray characterization (e.g. nano-X-ray diffraction or nano-X-ray fluorescence) can reveal structural or chemical properties of materials at relatively high spatial resolutions (~50-100 nm),[1,4,18,19] but may also damage samples and often requires synchrotron-based advanced light sources.[6,9]

We turn to scanning probe microscopy (SPM), which is a mechanical microscopy method that uses a metallic, sharp tip on a cantilever to detect variations in the surface of a sample with nanoscale resolution. SPM commonly measures topographic variations in thin film samples, but we can also harness it to extract more advanced functional information, such as local conductivity,[20,21] surface photovoltage,[22–25] and stiffness.[6,26]

Time-resolved electrostatic force microscopy (trEFM) is a dynamic SPM method that measures transient changes in the electrostatic force gradient between the oscillating SPM cantilever and the surface of a semiconducting sample.[12,27–29] Upon photoexcitation of a semiconductor, we generate electronic carriers and, depending on the material, induce ion motion.[2,30,31] The evolution of these charged carriers results in a transient equilibration of the surface potential of the sample.[30] As the surface potential equilibrates under excitation, the frequency of the oscillating cantilever deviates from the drive frequency; the timescale of this deviation reveals much about the semiconductor sample: local external quantum efficiency,[2,12,27] surface recombination velocity,[30] and electronic carrier recombination process.[30] We use trEFM to explore these processes on the nanoscale,

providing valuable insight into how morphological features affect the functional properties of a given sample.

Because trEFM is a dynamic SPM method, we collect time-resolved data at each pixel of an image. Resulting image "datacubes" are rich with spatially resolved and temporally resolved information. As such, we can explore methods and tools that maximize our understanding of samples.[1,32–35] Multi-dimensional SPM datasets are ripe with opportunity to apply machine learning (ML) and data science methods to overcome noise limitations, extract and reconstruct dynamics from complex signals, and understand the significance of correlations.[33,35] The advantageous harmony between multi-dimensional SPM techniques and ML and data science enables us to better understand our materials and advance our research.

1.2 Lead Halide Perovskites

Lead halide perovskites are a class of semiconducting materials with promising applications in various optoelectronic devices, such as light emitters[36,37] (including quantum light emitters[38]), radiation detectors,[39] and photovoltaics.[7,37,40,41] Indeed, single-junction perovskite thin film photovoltaic devices have surpassed 26% efficiency, on par with silicon-based technology.[42]

Perovskites have an ABX_3 crystal structure with corner-sharing octahedra, where the A-site is occupied by a monovalent cation such as methylammonium, formamidinium, or cesium, the B-site is occupied by a divalent cation such as lead(II) or tin(II), and the X-site interstitial space is occupied by a halide ion (like iodide, bromide, or chloride).[43] By exchanging the A-site cation with a bulkier (typically organic) cation such as phenethylammonium or butylammonium, we can scale down the dimensionality of the perovskite, creating quasi-2D or layered perovskite heterostructures of the formula $A'_2A_{n-1}B_nX_{3n-1}$ (where A' is the substituted, larger organic cation).[44] Indeed, by tuning the composition of the perovskite crystal itself, in particular changing the halide composition, we can change the bandgap of the material.[26,40,43,45]

Perovskite semiconductor thin films are particularly exciting because of their solution processability,[37] relative cost effectiveness,[37,45] and defect tolerance.[46–48] However, despite their defect tolerance, eliminating defects is a key goal for the field.[46–51] Ion vacancies, interstitial "extra" ions, and replacements in the crystal lattice are linked to issues with stability under constant illumination or bias.[46,47,50,51] For this reason, chemical additives,[10,52,53] preparation methods,[54] and post-treatments[20,23,54–56] that reduce defects are of great interest to the field at large. Many advanced mixed-cation, mixed-halide perovskite compositions ideal for single- or multi-junction photovoltaic devices exhibit morphological features ranging in size from a hundred nanometers to several micrometers.[2,7,11] These morphological features are commonly referred to as "grains," though intra-"grain" crystallographic domains identified via EBSD suggests that may be an oversimplification.[11,57] Understanding how these morphological features relate to the functional performance of these materials—their conductivity,[20] surface potential,[1,22,23] and more—is paramount to optimizing not only the perovskite material itself, but additives, manufacturing methods, and post-treatments.

In this thesis, we present the application of trEFM to probe perovskite semiconductor surface potential dynamics as a function of excitation intensity and wavelength. In Chapter 2, to improve

on trEFM data processing methods, we apply ML (a feedforward artificial neural network) to extracting cantilever-independent dynamics from the trEFM cantilever frequency signal.[31] We build on this work further in Chapter 3, where we present a more robust convolutional neural network that assumes a single- or bi-exponential underlying function for extracting cantilever-independent dynamics from trEFM frequency signals that better reconstruct experimental signals.[58] Finally, in Chapter 4 we examine what physical processes trEFM captures in mixed-cation, mixed-halide perovskite samples, combining post-treatment with passivating agents, wavelength- and intensity-dependent experiments, and drift-diffusion simulations to present a unified understanding of trEFM.[30]

1.3 References

1. Giridharagopal, R., Cox, P. A. & Ginger, D. S. Functional Scanning Probe Imaging of Nanostructured Solar Energy Materials. *Acc. Chem. Res.* **49**, 1769–1776 (2016).

2. Giridharagopal, R. *et al.* Time-Resolved Electrical Scanning Probe Microscopy of Layered Perovskites Reveals Spatial Variations in Photoinduced Ionic and Electronic Carrier Motion. *ACS Nano* **13**, 2812–2821 (2019).

3. Tennyson, E. M., Gong, C. & Leite, M. S. Imaging Energy Harvesting and Storage Systems at the Nanoscale. *ACS Energy Lett.* **2**, 2761–2777 (2017).

4. Tennyson, E. M., S Doherty, T. A. & Stranks, S. D. Heterogeneity at multiple length scales in halide perovskite semiconductors. *Nat. Rev.* **4**, 573–587 (2019).

5. Tennyson, E. M. *et al.* Correlated Electrical and Chemical Nanoscale Properties in Potassium-Passivated, Triple-Cation Perovskite Solar Cells. *Adv. Mater. Interaces* **7**, 2000515 (2020).

6. Mela, I. *et al.* Revealing Nanomechanical Domains and Their Transient Behavior in Mixed-Halide Perovskite Films. *Adv Funct Mater* **31**, (2021).

7. DeQuilettes, D. W. *et al.* Impact of microstructure on local carrier lifetime in perovskite solar cells. *Science (1979)* **348**, 683–686 (2015).

8. Delport, G., Macpherson, S. & Stranks, S. D. Imaging Carrier Transport Properties in Halide Perovskites using Time-Resolved Optical Microscopy. *Adv. Energy Mater.* **10**, 1903814 (2020).

9. Jones, T. W. *et al.* Lattice strain causes non-radiative losses in halide perovskites. *Energy Environ Sci* **12**, 596–606 (2019).

10. Taddei, M. *et al.* Ethylenediamine Addition Improves Performance and Suppresses Phase Instabilities in Mixed-Halide Perovskites. *ACS Energy Lett.* **7**, 4265–4273 (2022).

11. Jariwala, S. *et al.* Local Crystal Misorientation Influences Non-radiative Recombination in Halide Perovskites. *Joule* **3**, 3048–3060 (2019).

12. Karatay, D. U., Harrison, J. S., Glaz, M. S., Giridharagopal, R. & Ginger, D. S. Fast time-resolved electrostatic force microscopy: Achieving sub-cycle time resolution. *Rev. Sci. Instrum.* **87**, 053702 (2016).

13. Groves, C., Reid, O. G. & Ginger, D. S. Heterogeneity in Polymer Solar Cells: Local Morphology and Performance in Organic Photovoltaics Studied with Scanning Probe Microscopy. (2010) doi:10.1021/ar900231q.

14. Coffey, D. C. & Ginger, D. S. Time-resolved electrostatic force microscopy of polymer solar cells. *Nat. Mater.* **5**, 735–740 (2006).

15. Taddei, M. *et al.* Interpreting Halide Perovskite Semiconductor Photoluminescence Kinetics. *ACS Energy Lett.* **9**, 2508–2516 (2024).

16. Moerman, D., Eperon, G. E., Precht, J. T. & Ginger, D. S. Correlating Photoluminescence Heterogeneity with Local Electronic Properties in Methylammonium Lead Tribromide Perovskite Thin Films. *Chem. Mater.* **29**, 5484–5492 (2017).

17. Bischak, C. G., Sanehira, E. M., Precht, J. T., Luther, J. M. & Ginsberg, N. S. Heterogeneous Charge Carrier Dynamics in Organic−Inorganic Hybrid Materials: Nanoscale Lateral and Depth-Dependent Variation of Recombination Rates in Methylammonium Lead Halide Perovskite Thin Films. *ACS Nano Lett.* **15**, 4799–4807 (2015).

18. Zhou, Y., Herz, L. M., Jen, A. K.-Y. & Saliba, M. Advances and challenges in understanding the microscopic structure–property–performance relationship in perovskite solar cells. *Nat. Energy* **7**, 794–807 (2022).

19. Guthrey, H. & Moseley, J. A Review and Perspective on Cathodoluminescence Analysis of Halide Perovskites. *Adv. Energy Mater.* **10**, 1903840 (2020).

20. Shi, Y. *et al.* (3-Aminopropyl)trimethoxysilane Surface Passivation Improves Perovskite Solar Cell Performance by Reducing Surface Recombination Velocity. *ACS Energy Lett.* **7**, 4081–4088 (2024).

21. Kong, J., Giridharagopal, R., Harrison, J. S. & Ginger, D. S. Identifying Nanoscale Structure-Function Relationships Using Multimodal Atomic Force Microscopy, Dimensionality Reduction, and Regression Techniques. *J. Phys. Chem. Lett.* **9**, 3307–3314 (2018).

22. Jiang, F. *et al.* Scanning Kelvin Probe Microscopy Reveals That Ion Motion Varies with Dimensionality in 2D Halide Perovskites. *ACS Energy Lett.* **6**, 100–108 (2021).

23. Pothoof, J., Westbrook, R. J. E., Giridharagopal, R., Breshears, M. D. & Ginger, D. S. Surface Passivation Suppresses Local Ion Motion in Halide Perovskites. *J. Phys. Chem. Lett* **14**, 6092–6098 (2023).

24. Akrami, F., Jiang, F., Giridharagopal, R. & Ginger, D. S. Kinetic Suppression of Photoinduced Halide Migration in Wide Bandgap Perovskites via Surface Passivation. *J. Phys. Chem. Lett* **14**, 9310–9315 (2023).

25. Birkhold, S. T. *et al.* Interplay of Mobile Ions and Injected Carriers Creates Recombination Centers in Metal Halide Perovskites under Bias. *ACS Energy Lett* **3**, 52 (2018).

26. Sun, S. *et al.* Factors Influencing the Mechanical Properties of Formamidinium Lead Halides and Related Hybrid Perovskites. *ChemSusChem* **10**, 3740–3745 (2017).

27. Giridharagopal, R. *et al.* Submicrosecond time resolution atomic force microscopy for probing nanoscale dynamics. *Nano Lett.* **12**, 893–898 (2012).

28. Harrison, J. S. *et al.* Noncontact Imaging of Ion Dynamics in Polymer Electrolytes with Time-Resolved Electrostatic Force Microscopy. *ACS Nano* **13**, 536–543 (2019).

29. Tirmzi, A. M., Dwyer, R. P., Jiang, F. & Marohn, J. A. Light-Dependent Impedance Spectra and Transient Photoconductivity in a Ruddlesden-Popper 2D Lead-Halide Perovskite Revealed by Electrical Scanned Probe Microscopy and Accompanying Theory. *J. Phys. Chem. C* **124**, 13639–13648 (2020).

30. Breshears, M. D., Pothoof, J., Giridharagopal, R. & Ginger, D. S. Sub-diffraction Imaging of Carrier Dynamics in Halide Perovskite Semiconductors: Effects of Passivation, Morphology, and Ion Motion. *ArXiv* (2024).

31. Breshears, M. D., Giridharagopal, R., Pothoof, J. & Ginger, D. S. A Robust Neural Network for Extracting Dynamics from Electrostatic Force Microscopy Data. *J. Chem. Inf. Model.* **62**, 4342–4350 (2022).

32. Krull, A., Hirsch, P., Rother, C., Schiffrin, A. & Krull, C. Artificial-intelligence-driven scanning probe microscopy. *Commun. Phys.* **3**, (2020).

33. Kalinin, S. V. *et al.* Big, Deep, and Smart Data in Scanning Probe Microscopy. *ACS Nano* **10**, 9068–9086 (2016).

34. Gordon, O. M. & Moriarty, P. J. Machine learning at the (sub)atomic scale: Next generation scanning probe microscopy. *MLST* **1**, 023001 (2020).

35. Azuri, I., Rosenhek-Goldian, I., Regev-Rudzki, N., Fantner, G. & Cohen, S. R. The role of convolutionsl neural networks in scanning probe microscopy: a review. *Beilstein J. Nanotechnol.* **12**, 878–901 (2021).

36. Lin, K. *et al.* Perovskite light-emitting diodes with external quantum efficiency exceeding 20 per cent. *Nature* **562**, (2018).

37. Stranks, S. D. & Snaith, H. J. Metal-halide perovskites for photovoltaic and light-emitting devices. *Nat. Nanotech.* **10**, 391–402 (2015).

38. Nguyen, H. A. *et al.* Design Rules for Obtaining Narrow Luminescence from Semiconductors Made in Solution. *Chem. Rev.* **123**, 7890–7952 (2023).

39. Wei, H. & Huang, J. Halide lead perovskites for ionizing radiation detection. *Nat. Commun.* **10**, 1066 (2019).

40. Eperon, G. E., Horantner, M. T. & Snaith, H. J. Metal halide perovskite tandem and multiple-junction photovoltaics. *Nat. Rev.* **1**, 0095 (2017).

41. Jiang, F. *et al.* Improved reverse bias stability in p-i-n perovskite solar cells with optimized hole transport materials and less reactive electrodes. *Nat. Energy* **9**, 1275–1284 (2024).

42. Best Research-Cell Efficiency Chart. *NREL* (2024).

43. Sutton, R. J. *et al.* Bandgap-Tunable Cesium Lead Halide Perovskites with High Thermal Stability for Effi cient Solar Cells. (2016) doi:10.1002/aenm.201502458.

44. Stoumpos, C. C. *et al.* Ruddlesden-Popper Hybrid Lead Iodide Perovskite 2D Homologous Semiconductors. *Chem. Mater.* **28**, 2852–2867 (2016).

45. Wen, X. & Jia, B. *Fundamental Cause for Superior Optoelectronic Properties in Halide Perovskites*.

46. Kim, G.-W. & Petrozza, A. Defect Tolerance and Intolerance in Metal-Halide Perovskites 2. Defects in Perovskite Solar Cells: Efficiency versus Stability. *Adv. Energy Mater.* **10**, 2001959 (2020).

47. De Keersmaecker, M., Tirado, J., Armstrong, N. R. & Ratcliff, E. L. Defect Quantification in Metal Halide Perovskites Anticipates Photoluminescence and Photovoltaic Performance. *ACS Energy Lett* **9**, 243–252 (2024).

48. Siekmann, J., Ravishankar, S. & Kirchartz, T. Apparent Defect Densities in Halide Perovskite Thin Films and Single Crystals. *ACS Energy Lett.* **6**, 3244–3251 (2021).

49. Ono, L. K., Liu, S. & Qi, Y. Perovskite Solar Cells Reducing Detrimental Defects for High-Performance Metal Halide Perovskite Solar Cells. doi:10.1002/ange.201905521.

50. Sherkar, T. S., Momblona, C., Sessolo, M., Bolink, H. J. & Jan Anton Koster, L. Recombination in Perovskite Solar Cells: Significance of Grain Boundaries, Interface Traps, and Defect Ions. **2**, 43 (2017).

51. Birkhold, S. T. *et al.* Direct Observation and Quantitative Analysis of Mobile Frenkel Defects in Metal Halide Perovskites Using Scanning Kelvin Probe Microscopy. *J. Phys. Chem. C* **122**, 34 (2018).

52. Shen, X. *et al.* Chloride-Based Additive Engineering for Efficient and Stable Wide-Bandgap Perovskite Solar Cells. (2023) doi:10.1002/adma.202211742.

53. Kosmatos, K. O. *et al.* Methylammonium Chloride: A Key Additive for Highly Efficient, Stable, and Up-Scalable Perovskite Solar Cells. *Energy Environ. Mater.* **2**, 79–92 (2019).

54. Taddei, M. *et al.* Diamine Surface Passivation and Post-Annealing Enhance Performance of Silicon-Perovskite Tandem Solar Cells. *ArXiv*.

55. Dequilettes, D. W. *et al.* Photoluminescence Lifetimes Exceeding 8 μs and Quantum Yields Exceeding 30% in Hybrid Perovskite Thin Films by Ligand Passivation. *ACS Energy Lett.* **1**, 438–444 (2016).

56. Wang, J. *et al.* Reducing Surface Recombination Velocities at the Electrical Contacts Will Improve Perovskite Photovoltaics. *ACS Energy Lett.* **14**, 222–227 (2019).

57. Li, W. *et al.* Subgrain special boundaries in halide perovskite thin films restrict carrier diffusion. *ACS Energy Lett* **3**, 2669–2670 (2018).

58. Breshears, M. D., Giridharagopal, R. & Ginger, D. S. Multi-Output Convolutional Neural Network for Improved Parameter Extraction in Time-Resolved Electrostatic Force Microscopy Data. *In Prep.* (2025).

Chapter 2: A Robust Neural Network for Extracting Dynamics from Time-Resolved Electrostatic Force Microscopy

Adapted from: Breshears, M. D., Giridharagopal, R., Pothoof, J. & Ginger, D. S. A Robust Neural Network for Extracting Dynamics from Electrostatic Force Microscopy Data. *J. Chem. Inf. Model.* **62**, 4342–4350 (2022).

2.1 Overview

Advances in scanning probe microscopy (SPM) methods such as time-resolved electrostatic force microscopy (trEFM) now permit the mapping of fast local dynamic processes with high resolution in both space and time, but such methods can be time consuming to analyze and calibrate. Here, we design and train a regression neural network (NN) that accelerates and simplifies the extraction of local dynamics from SPM data directly in a cantilever-independent manner, allowing the network to process data taken with different cantilevers. We validate the NN's ability to recover local dynamics with a fidelity equal to or surpassing conventional, more time-consuming calibrations using both simulated and real microscopy data. We apply this method to extract accurate photoinduced carrier dynamics on n=1 butylammonium lead iodide, a halide perovskite semiconductor film that is of interest for applications in both solar photovoltaics and quantum light sources. Finally, we use SHapley Additive exPlanations (SHAP) to evaluate the robustness of the trained model, confirm its cantilever-independence, and explore which parts of the trEFM signal are important to the network.

2.2 Introduction

Advances in scanning probe microscopy (SPM) have accelerated over the past decade, driven by the need to assess nanoscale structure-function relationships of new materials for applications ranging from energy harvesting to quantum information.[1–3] At the same time, data science capabilities in the physical sciences have undergone a revolution driven by the need for processing, representing, and interpreting vast amounts of data.[1,3–11] The confluence of these advances in SPM and data science has proven extremely beneficial for materials chemists and materials scientists, providing new opportunities in data collection automation and in situ quality control.[9,10,12–14] A variety of SPM techniques provide high-resolution spatial information with many complex functional modes that share common features, such as fast time-resolved electrostatic force microscopy,[2,15,16] "general-mode" Kelvin probe force microscopy,[1,6] and phase-kick electrostatic force microscopy.[17] These techniques result in multidimensional, information-rich data where each pixel in an image contains a complex, time-dependent signal. Furthermore, the resulting data are not always directly plottable or interpretable with a simple physical interpretation. Broadly, researchers are interested in applying these techniques to a variety of systems, from hybrid organic-inorganic metal-halide perovskites to conjugated polymers to study phenomena such as charging and local quantum efficiency or ion dynamics.[1,2,10,11,14,15,18–24] Machine learning (ML) and data science techniques provide us with excellent tools to help process these data and study these systems.[3,14,25–28] Methods of signal boosting,[29–31] dimensionality reduction and representation,[2,11,18,30] and decomposition based in machine learning and data science are being developed to extract information efficiently and accurately from SPM images and signals.[14,25,26,32]

In practice, the use of ML for SPM data processing provides many potential advantages, namely robustness against noise, speed in application, and ease of handling multidimensional data.[3,11,25,28–30,33] Here, we demonstrate the use of a neural network (NN) to process data-rich SPM images from a feedback-free implementation of time-resolved electrostatic force microscopy (trEFM) (Figure 1a).[15,16] trEFM has the ability to extract transient dynamics down to the ~10 ns regime and has been used to study dynamics in systems ranging from organic solar cells[19,34–36] to perovskite semiconductors.[1,2] In this method, a transient perturbation whose characteristic timescale is governed by the cantilever's local dynamic properties induces a change in the SPM cantilever's motion. The exact time-dependent profile of the sample's response to this excitation alters the transient motion of the SPM cantilever, thus encoding details of the short time perturbation that can be discerned by analyzing the evolution of the cantilever at subsequent times.[2,15,16,37] Previously, we have recovered the time dynamics using a straightforward calibration procedure (Note S1).[16] However, this procedure is not only time consuming, but also requires recalibration upon changing the cantilever.[15,16] Furthermore, in practice, the analysis procedure often ignores much of the time-dependent data, which likely degrades the achievable signal/noise under a given set of imaging conditions.

Here, to address these issues, we demonstrate the use of a neural network to infer the early time sample dynamics based on the entirety of the long-time cantilever oscillatory motion. Not only does the network utilize the entire time-dependent cantilever frequency signal, it also naturally incorporates key cantilever parameters like spring constant and quality factor as nodes in the ML process, allowing a single network to process a broad range of data. We apply this network to study both simulated trEFM signals, "model" trEFM signals, and practical experiments of photoinduced charging on halide perovskite semiconductor samples. We also explore the relationship among the features of our data as learned by the neural network and how those explanations contribute to the robustness of the network as a tool using SHapley Additive exPlanations (SHAP).[38,39]

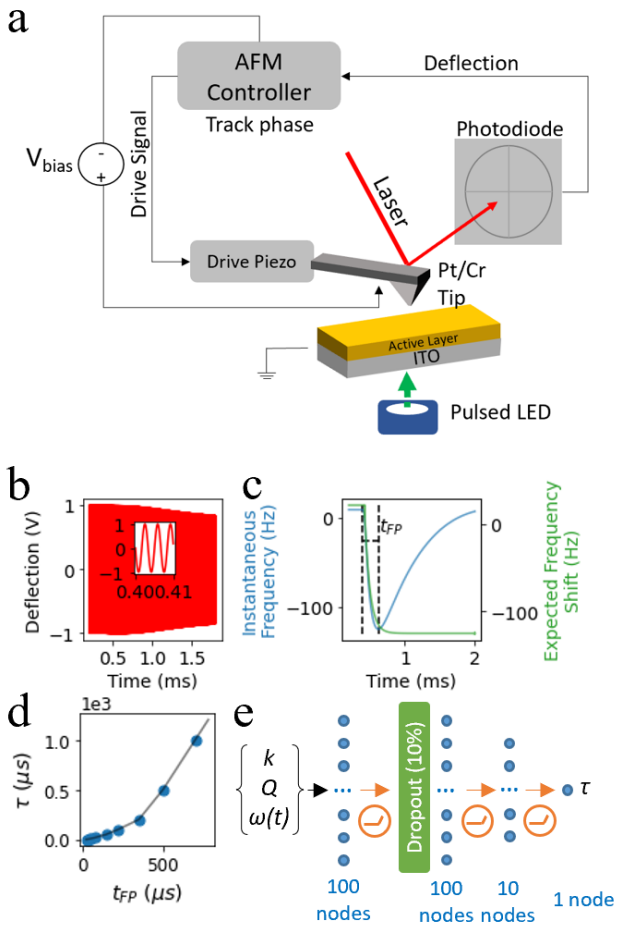

Figure 1: (a) Schematic of the trEFM workflow process. Optical pulses induce transient photocarriers in the sample, which in turn create transient perturbations of the electrostatic force gradient experienced by the oscillating tip; this change is captured by (b) the evolving raw cantilever deflection *vs*. time where the inset is a sample of the deflection from 0.40 to 0.41 ms. Using a STFT[40] we extract (c) the instantaneous frequency *vs*. time (blue), whereas we would expect to see the frequency shift with respect to time behave like a single-exponential (green) as discussed in the text, but due to convolution with cantilever physics, those dynamics described by a single exponential are hidden. The time to first peak, t_{FP}, can be empirically calibrated to extract the characteristic time constant τ that describes the expected single exponential behavior using (d) a cantilever-specific calibration curve.[15,16] We compare this traditional approach against the use of a neural network (e) to extract τ. After each fully connected layer (blue), there is a rectified linear unit activation (orange).

trEFM has been discussed in detail by our group in previous work.[15,16] Briefly, during trEFM measurements, the cantilever is initially driven at its resonance frequency by a shake piezo (Figure 1a) and its entire motion is digitized. At a defined point in time, we trigger a transient excitation that induces a time-dependent change in the electrostatic force gradient between the conducting tip and the sample. The nature of this excitation depends on the desired application; for example, an illumination source for studying photocharging in photovoltaics[2] or a voltage pulse for studying ion motion (Appendix A Figure S1a).[19,41] The resulting time-dependent electrostatic force gradient between the cantilever tip and the sample therefore captures the dynamics of interest in the sample.

The perturbation in the electrostatic force gradient changes the cantilever's resonance frequency,[15,16,42,43] meaning these dynamics are reflected in the instantaneous frequency of the cantilever oscillation (Figures 1b and 1c).[15,16]

Given the instantaneous frequency as a function of time, we can calculate the time to first peak, t_{FP} (Figure 1c), which is the time it takes for the frequency shift to reach its maximum magnitude after the charging trigger event prior to returning to steady-state (the drive frequency). A long t_{FP} indicates slow charging behavior while a short t_{FP} indicates fast charging behavior.[16] However, for a fixed sample response, the exact t_{FP} depends on the cantilever parameters[15,16] like spring constant (k, N/m) and quality factor (Q), meaning that each cantilever would need to be independently calibrated. Note S1 discusses the need for cantilever calibration in more detail, specifying that given the case where the excitation is a single exponential as is common in many physical phenomena, the expected change in resonance frequency would also be a single exponential (Figure 1c, green). However, this is not what we observe; instead, we observe a convolution of the cantilever physics with the sample response to the perturbation (Figure 1c, blue). This poses a challenge when extracting the characteristic charging constant, τ (Equations S1 and S2, Figure 1d), for empirical comparison across experiments.

Here, we replace the calibration step with a neural network that has been trained on a range of simulated cantilever data. Specifically, after demodulating the experimental cantilever deflection vs. time using a short-time Fourier transform (STFT) to obtain the instantaneous cantilever frequency vs. time, we use a regression-style NN to reconstruct the dynamics of perturbation that affects the sample (Figure 1e). The NN consists of 8 layers: 4 fully connected layers, 3 rectified linear unit (ReLU) layers, and 1 random dropout layer for regularization (dropping 10% of the data at random, Figure 1e). We trained the network using the L1-loss function to measure the absolute difference between the network output and the target value. We built our network using the PyTorch Lightning framework.[44] Our NN is a simple feedforward architecture that takes as input the cantilever parameters (k, Q) and instantaneous frequency signal; at each pixel of an image, we pass these data to the NN, which then returns the time constant. This network provides robust, accurate trEFM data interpretation in a cantilever-independent manner and can ultimately be applied to automated data interpretation once integrated into the imaging software.

2.3 Methods

Synthesis of butylammonium lead iodide: n-butylammonium lead iodide (BAPI) films were prepared on indium tin oxide (ITO) substrates purchased from Thin Film Devices (resistivity of 20 ± 2 Ω; work function of -4.8 to -5.0 eV; and surface roughness of ≤ 7 Å RMS). The ITO substrates were sonicated in baths of detergent in de-ionized water, acetone, and 2-propanol. BA_2PbI_4 perovskite solution was prepared by dissolving 1.8 M n-butylammonium iodide (BAI, GreatCell Solar Ltd.) and 0.9 M lead (II) iodide (PbI_2, Sigma-Aldrich) in dimethylformamide (DMF, Sigma-Aldrich). The solution was stirred for 1 hour and then spin coated on plasma-treated, cleaned ITO substrates at 4000 rpm for 40 s followed by thermal annealing at 100 ºC for 10 minutes.[21] All preparation was in a nitrogen glovebox.

UV-Vis absorbance measurement: spectra of BAPI films on glass (prepared as above) were recorded on an Agilent 8453 UV-Vis Spectrometer over 400 – 800 nm with an integration time of 0.5 s.

Time-resolved electrostatic force microscopy (trEFM) measurements: The trEFM measurement technique and experimental setup have been discussed in detail.[2,15,16] Measurements were performed on an Asylum Research MFP3D. All measurements used Pt-coated cantilevers (Mikromasch HQ:NSC15/Pt) driven at resonance frequency (~300 kHz). The sample was kept under active nitrogen in a sealed flow cell. The cantilever oscillation was recorded using a 16-bit A/D digitizer (Dynamic Signals/GaGe Razor Express CSE1622), typically at 5 MS/s, and synced to the cantilever oscillation phase (180º) using custom trigger electronics (detailed circuit information can be found in Supporting Information in our previous reports; additional information available upon request).[15,16] Data were recorded over the course of 2 ms, during which a voltage pulse was applied to the cantilever of 10 V at approximately 0.1 ms (Appendix A Figure S1a). For the BAPI samples, we measured photocharging using a 455 nm LED (LEDEngin) excitation pulse triggered at 0.4 ms, inducing charging behavior in the active layer.[2] This wavelength was used because it is well within the absorbance of BAPI (Appendix A Figure S2). The LED was focused via a bottom objective on an inverted optical microscope and co-aligned with the cantilever tip. The illumination intensity was measured using a calibrated photodiode and calculated based on the LED illumination area; four intensities were used: 42.1, 109.9, 160.8, and 203.6 W/m^2. For conventional trEFM, thirty scans were collected at each pixel and averaged to increase the signal-to-noise ratio. Raw cantilever deflection data were used to extract the instantaneous frequency by demodulating the time-dependent cantilever amplitude using a short-time Fourier transform (STFT) and then using a parabolic estimation of the peak frequency (ridge finding) per time segment. This code is freely available online via the FFTA Python package (https://github.com/GingerLabUW/FFTA).

Setup and training of the neural network: NNs are sensitive to biases introduced through the training process, such as skewed or unrealistic distributions of training data leading to poor performance on test data.[27,28,33,45,46] To combat such bias, we simulated a training dataset with target τ values ranging from 1 to 500 µs with a precision of 10 ns. We used uniform distribution of the log (base 10) of these target values so that the network had a uniform representation of the three orders of magnitude (see Appendix A Figure S3b). We simulated these data via the aforementioned FFTA package using cantilevers with a uniform distribution of k values (N/m) and Q factors such that the resulting network would be cantilever-independent (Figures S3c and S3d). Additionally, we applied Gaussian noise to each simulated raw deflection before demodulating to instantaneous frequency to create a random signal-to-noise ratio (60, 70 or 80) (Note S2). We randomly selected the Fourier window size (either 60 or 70 µs) for the STFT when extracting the instantaneous frequency, which in practice would change the extracted t_{FP} value for a given τ; this forces the network to not rely on t_{FP} but rather the overall shape of the instantaneous frequency signal. These steps—the varied cantilever parameters, the addition of noise, and the random Fourier time resolutions—ensured that our training data were as realistic as possible.

Each pixel is evaluated by the network independent of its neighbors. The trained model takes as input k, Q, and the instantaneous frequency signal (Figure 1e). To compensate for changes in the tip state causing larger shifts in the frequency shift magnitude (while not changing the actual shape of the frequency signal), we normalized the instantaneous frequency to be between 0 and 1 prior to training. This step ensured that only the shape of the frequency trace was considered by the network within the context of the cantilever parameters. Data scientists calculate certainty for machine learning models in a variety of ways.[46–48] Gal *et al.* postulated that by maintaining dropout in a trained model, the same input will result in slightly different outputs when given to the model

multiple times. By extracting multiple τ values from a network with dropout, we calculated the average output and quantified the standard deviation, which we refer to as quasi-ensembling.[47,48]

2.4 Results and Discussion

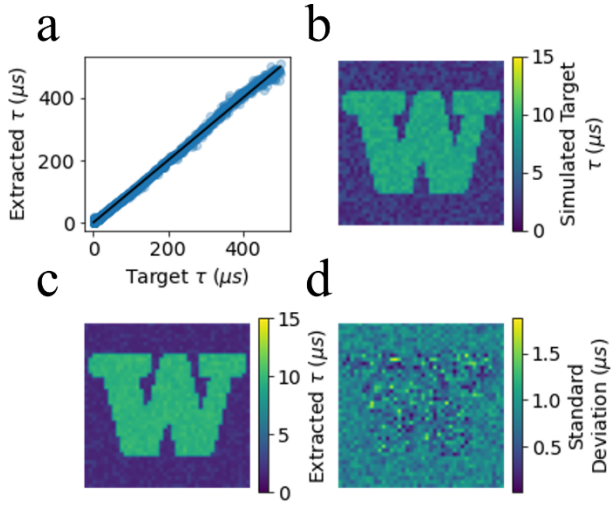

Figure 2: (a) Parity plot of network-extracted τ *vs.* target τ values for 3,000 simulated test instantaneous frequency traces where the black line represents perfect agreement with an R^2 score of 0.89, demonstrating the network's excellent performance on simulated data; (b) separately simulated target τ values used as the basis for the simulation of a trEFM image datacube; (c) the trained network-extracted τ values from data simulated according to (b), showing excellent qualitative agreement with the simulated target values; and (d) standard deviations for the extraction for (c) given quasi-ensembling of 100 network outputs as discussed in the text.

After training the network on 17,000 input arrays (containing k, Q, and the normalized instantaneous frequency traces) for 200 epochs, we test our NN on 3,000 simulated input arrays it had not seen before. Figure 2a shows a parity plot of the network extracted τ values for these 3,000 simulated test inputs plotted against the known τ values for these data, trending very close to perfect agreement (black line) with a mean absolute difference of 2.14 µs (median absolute difference of 0.72 µs) and a mean percent error of 9.64% (median 3.08%). The R^2 score for Figure 2a is 0.89. Using the quasi-ensembling method,[47,48] we quantified the uncertainty associated with the NN prediction on these 3,000 test inputs; the average standard deviation of the network predictions was 3.82 µs (with a median of 1.41 µs). Appendix A Figure S4 shows the distributions of the absolute difference between the network-extracted τ values and target τ values, percent error, and standard deviation for all 3,000 test inputs.

To further evaluate the network's performance on simulated image data, we created a 42 by 42 pixel hyperspectral trEFM image. Figure 2b shows the τ values used for this simulation, longer τ values (~10 µs) composing the letter W on a background of shorter τ values (~3 µs). After simulating the deflection of the cantilever according to these τ values, we added Gaussian noise to the raw cantilever deflection, resulting in a signal-to-noise ratio of 70 (Note S2), demodulated to obtain the instantaneous frequency for each pixel in the image with the same STFT we use for experimental data collection, and normalized these instantaneous frequency signals. The input array for each pixel contained the cantilever parameters k and Q in addition to this normalized frequency trace; we collected the network prediction for these input arrays 100 times and averaged

the extracted τ value for each pixel (Figure 2c) according to the quasi-ensembling method previously discussed. Figure 2d shows the standard deviation calculated from this quasi-ensembling averaging process, revealing an average standard deviation of 0.81 µs (median standard deviation of 0.82 µs).

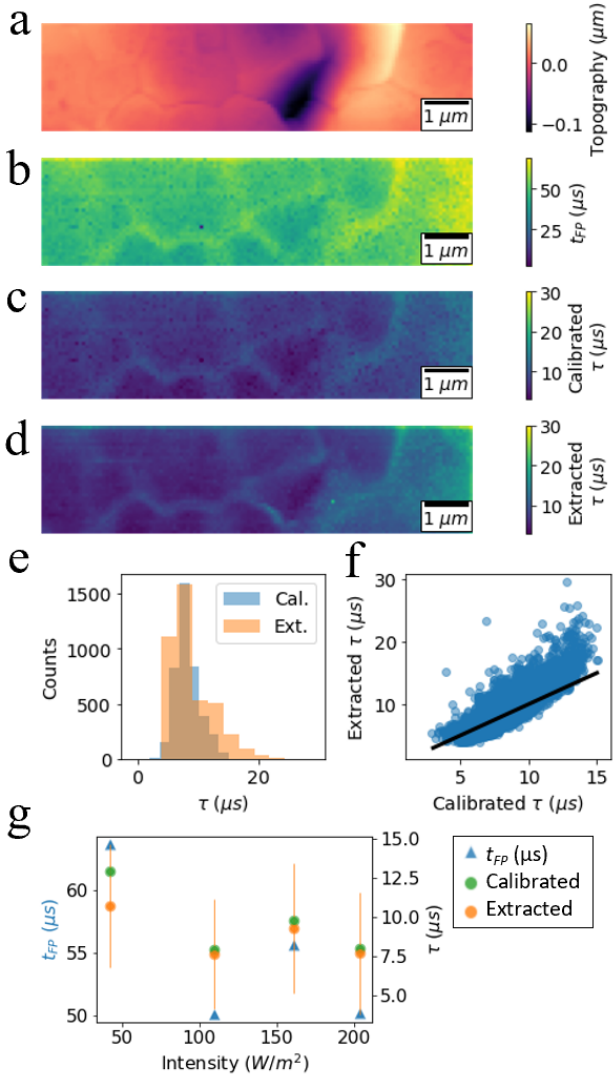

Figure 3: (a) Topography of halide perovskite BAPI showing grain sizes of approximately 2-4 µm; (b) image of t_{FP} values in the same region as (a) calculated from instantaneous frequency traces following excitation with 455 nm photoexcitation at 109.9 W/m^2; (c) image of the τ values calibrated from the t_{FP} data (b) using the manual calibration according to the calibration curve seen in Figure 1d (Note S1); (d) image of the τ values extracted using the neural network described in the text, showing good qualitative agreement with (c); (e) overlaid histograms of calibrated and extracted τ values revealing overall agreement between the order of magnitude of calibrated and network-extracted τ values; (f) parity plot comparing network-extracted τ values against calibrated τ values showing qualitative agreement between the two where the black line is 1-to-1 correlation (perfect agreement) with an R^2 score of 0.61; and (g) summary plot of average t_{FP}, average calibrated τ values, and average extracted τ values on BAPI at varied light intensities where error

bars are the standard deviation, showing expected shift to faster dynamics at higher light intensities.

In addition to the tests on simulated data, we applied our NN to experimental trEFM data on n=1 butylammonium lead iodide (BAPI) films. BAPI is a layered Ruddlesden-Popper halide perovskite material with a large exciton binding energy of 400-500 meV[49,50] and good surface passivating properties that are currently of interest in optoelectronics applications.[51] We then compared the network's results to the images obtained via the traditional calibration method (Note S1). Figure 3a shows the topography of the BAPI film, where we observe morphological features, possibly grains, approximately 2-4 μm across. Figure 3b shows the heterogeneity in t_{FP} across the presumed grains and grain boundaries. Consistent with previous reports,[2] grain centers appear to generally have a shorter t_{FP} than grain boundaries, on the order of 42.1 μs as compared to 49.6 μs. We performed a traditional calibration on our cantilever giving us a t_{FP}-τ calibration curve (as seen in Figure 1d), which allowed us to extract τ values from the data as shown in Figure 3c. The calibrated τ values are within the same order of magnitude as previous work on BAPI.[2,17]

Figure 3d shows the NN's extracted τ values calculated using the quasi-ensembling method previously described by averaging 100 network outputs to obtain each τ value (with a mean standard deviation of 1.17 μs and a median standard deviation of 1.00 μs). Our current calibration procedure, either via a simulated cantilever or separate calibration with voltage pulses according to Equation S2, takes 30-60 minutes compared to less than 1 minute with the NN, representing a significant benefit to using a network approach (with the additional benefit of not requiring the unloading and preservation of the cantilever). Figure 3d also demonstrates how the NN is less sensitive to noisy instantaneous frequency data and Figure 3e shows the distributions of the calibrated and network-extracted τ values. Appendix A Figure S5 shows corresponding images of the absolute difference, percent error, and standard deviation, confirming overall agreement between the calibrated τ values and the network extracted τ values. During the traditional calibration process, t_{FP} is calculated from the instantaneous frequency via curve fitting, which can cause occasional fitting errors and result in more scattered noisy pixels. As such, slight deviations in t_{FP} may lead to erroneous τ assignments that degrade the overall image quality. Because here we used the entire instantaneous frequency signal as input to the NN, our output image is less susceptible to these errors, resulting in higher signal-to-noise.

By plotting the NN-extracted τ values against the calibrated τ values in Figure 3f, we observe where the network disagrees with the calibration, giving us an R^2 score of 0.61. We hypothesize that this disagreement may be due to: (i) poorly calibrated τ values in Figure 3c due to the sensitivity of t_{FP} calculation; and/or (ii) the network trained on simulated data to which we applied varying levels of Gaussian noise, and it is possible that the noise we observe experimentally is not well represented by Gaussian noise, and thus would lead to the network having an inaccurate representation of realistic frequency signals. Noise produced by the jitter in the trigger may not be accurately simulated in the training data, either.

To further confirm the validity of the NN process, we collected data on the BAPI sample in the same region at various light intensities in a non-sequential order. The charging dynamics of the halide perovskite system are expected to be faster with increasing incident light intensity (shorter τ values and thus shorter t_{FP}).[2] Figure 3g shows how the neural network-extracted τ values follow the same trend as the t_{FP} and calibrated τ values. The network-extracted τ values are in good agreement with the calibrated τ values and, as expected, when we increase the light intensity, the network correctly identifies faster photoinduced charging dynamics. Figures S6-S8 show the

topography, t_{FP}, calibrated τ value, network-extracted τ value, and error metric images for these varied light intensities; Table S1 summarizes these data as well. Overall, Figure 3 demonstrates an excellent application of the robust NN to experimental data.

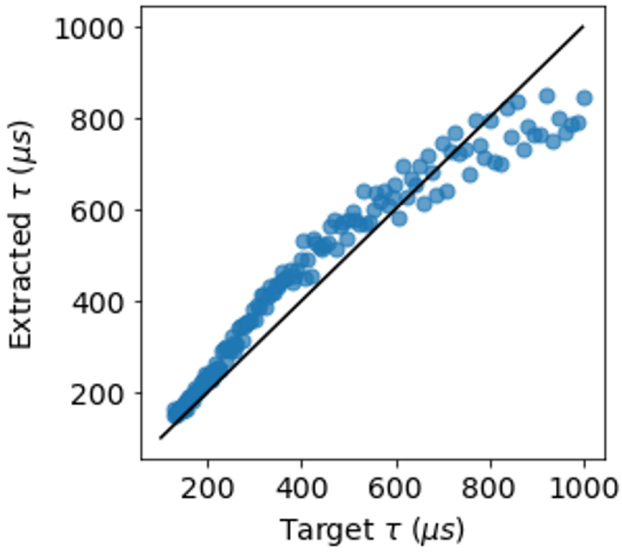

Figure 4: Parity plot comparing the network extracted τ values *vs*. the target, known τ values collected via feeding voltage pulses according to Equation S2 into ITO and processing the cantilever response. The black line is 1-to-1 correlation or perfect agreement between the extracted and calibrated τ values; we observe deviation from perfect agreement as target τ values grow greater than the limit of the range of training τ values (500 µs) but overall good regression in the longer time regime. The R^2 score for these data is 0.89.

The data we collected on BAPI are well within the range of target values the NN trained on (ranging from 1 to 500 µs). To further evaluate the robustness of our approach, we test the model's performance on experimental data beyond its training range by performing a cantilever calibration with 150 voltage pulses to ITO with τ values ranging from 100 to 1,000 µs. Figure 4 shows the NN's performance on these data. Overall, the network-extracted τ values trend close with unity (the black line, 1-to-1 correlation), deviating more from perfect agreement as the target values surpassed 500 µs; the R^2 score for these data is 0.89. Distributions of the absolute difference, percent error, and standard deviations for each of these predictions are provided in Appendix A Figure S9. Some disagreement in the longer time-regime is expected due to the network's lack of information for this timescale during training, however Figure 4 shows promising results for the model's ability to extrapolate and regress on such long-timescale data. Indeed, the network's increased performance—higher R^2 score—as compared to the results on BAPI may be explained by BAPI's dynamics not being well represented by single exponential behavior because of the combination of trap-mediated motion, carrier motion, and potential ion motion in these materials.[2,22] Future iterations on this neural network may include biexponential and stretch exponential classification capabilities to address this issue. The R^2 value for the network-extracted τ values on BAPI is a comparison of the network's performance and the traditional t_{FP}-τ calibration method, whereas the R^2 value for the network extracted τ values on ITO is a comparison of the network's performance and known τ values that follow single exponential behavior. Fundamentally these R^2 values are measuring agreement between two different "ground truths," meaning while interesting that the voltage pulses to ITO are more correctly interpreted by the

network than the measured photocharging dynamics of BAPI, ultimately these metrics are not the same.

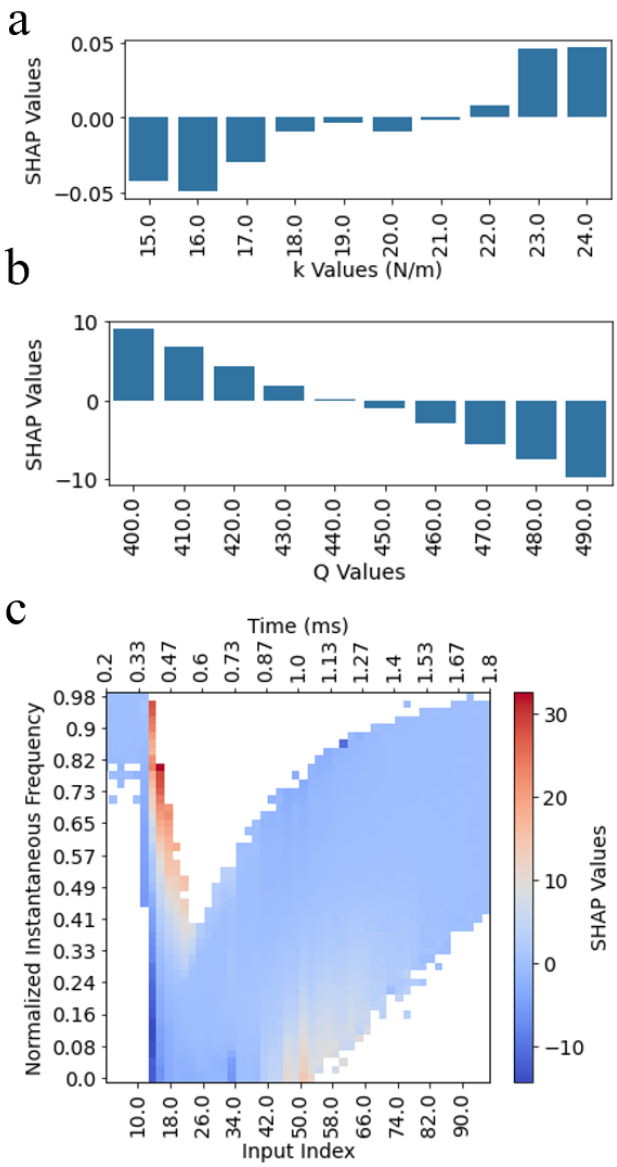

Figure 5: (a) SHAP value distribution according to variations in k (N/m) at index 0 of prepared, simulated input test data and (b) SHAP value distribution according to variations in Q at index 1 of prepared, simulated input test data, which together demonstrate the network's cantilever independence, seeing as it identifies significant and varied contributions from the cantilever parameters on subsequent signal interpretation; and (c) heatmap of instantaneous frequency traces ranging from 1 to 500 µs colored by SHAP value, revealing that initial frequency shift and subsequent cantilever relaxation are identified as important to the network's interpretation of the data on the whole.

Finally, we attempted to understand how the NN functions as a tool and explain its performance.[38,39,46,52,53] To this end, we used SHapley Additive exPlanations (SHAP) to explore how the network interprets individual features within the data.[38] SHAP values were developed in

the context of cooperative game theory as a measure of the contributions of individual players (features) to the outcome of the game (predictions), and have emerged as useful quantifiers of the importance of various features to a particular machine-learning model that make them one of the most widely used methods for model interpretation today.[38,39] A SHAP value given for a particular feature may be positive or negative, indicating which direction—above or below the mean model output—a feature "pushes" the NN prediction. SHAP values cannot attribute any causal relationships that underly the features and targets.[38,39,52,53] Further detailed discussion of SHAP as it applies to explainable ML can be found in Note S3.[38,39]

We use SHAP values to interpret the features contributing to the network-extracted τ values across the simulated test dataset. In the present case, our features include the spring constant k, the cantilever quality factor Q, and instantaneous frequency *vs*. time trace, $\omega(t)$. Because we know that k and Q affect the cantilever dynamics,[54] we use SHAP values to determine how they impact the network output. Figures 5a and 5b show the distribution of SHAP values assigned to the input indices containing the cantilever spring constant, k (N/m), and the cantilever quality factor, Q, respectively. The SHAP value distribution across both input feature values is asymmetrical, indicating that the NN has learned the significance of the cantilever parameters on the subsequent signal interpretation. Both k and Q provide necessary context to the resulting frequency signal, confirming what we have understood and addressed via individual cantilever calibration in the past. The confirmation that the NN has learned the importance of these parameters bolsters confidence in its performance since it is a conclusion supported by the physics of the damped driven harmonic oscillator approximation of the cantilever and simulated evidence.[2,15,16]

Finally, we use SHAP to investigate which time-dependent features in the instantaneous frequency signal affect the resulting τ. Figure 5c demonstrates the distribution of SHAP values for the indices that contain the instantaneous frequency signal. On the x-axis is the input index (translating to approximately 0.2 to 1.8 ms in the experiment). The y-axis is the normalized frequency signal for each index. This plot is a heatmap of the 3,000 simulated test instantaneous frequency traces of varied k and Q parameters, where each bin is colored by the average SHAP value, revealing how the network, on average, interprets the frequency signal at each index. Given a "sharp" or fast frequency shift, indicating a short τ, we should expect the model output to be less than the average model output (83.05 μs), thus such features should be assigned negative SHAP values. Indeed, we observe negative SHAP values concentrated along the steep drop immediately after the trigger event (approximately index 14, 0.4 ms). Conversely, given a slow frequency shift (corresponding to a long τ), we would expect a τ value larger than the average model output (83.05 μs), meaning those frequency signals should have positive SHAP values. We observe positive SHAP values concentrated along frequency signals initial shift from equilibrium at a shallower, slower curve. Importantly, these SHAP data confirm a key hypothesis from previous trEFM data: the instantaneous frequency response represents a convolution of the initial transient response due to the dynamics of interest and the natural cantilever relaxation (due to its inherent k and Q) to its drive frequency. We therefore expect the interesting dynamics to be contained in the time indices nearest the trigger—the SHAP data in Figure 5c indeed confirm this observation, with the largest SHAP value magnitudes occurring at approximately 0.4 to 0.6 ms (indices 14-18).

2.5 Conclusion and Outlook

We designed, trained, and applied a neural network to interpret data-rich time-dependent scanning probe microscopy data, specifically trEFM. We showed that the neural network performs well on

both simulated data and real data, and can even operate, with reduced performance, on data outside its training regime. By replacing tedious calibration of each individual cantilever, the neural network speeds up the experimental workflow. Furthermore, the neural network improves the quality of the extracted data because it makes use of the entire instantaneous frequency *vs*. time signal, making the network a more robust tool. Additionally, the neural network can extract the time constants from experimental data on 2-dimensional halide perovskites; indeed, due to its robustness the model improved the image quality overall and correctly identified the expected trend of faster charging dynamics from data collected with higher light intensities. Finally, we used SHAP values to probe the innerworkings of the trained network, confirming that the cantilever parameters, k (N/m) and Q, influence the interpretation of the frequency signal, providing valuable context for the cantilever-independent model.

Ultimately, we anticipate that the neural network, which is available for download (https://github.com/mdbresh/NN_trEFM), accelerates more widespread use of trEFM and methods like it to study problems in areas ranging from photocarrier dynamics in halide perovskite for solar cells to charge fluctuations in quantum emitters.

2.6 Acknowledgements

Associated Content and Data Availability:

Supporting Information with additional notes discussing simulated noise, demodulation techniques, SHAP values, and additional error metric distributions, and SPM images of the samples shown in this work (PDF).

Code and example data is provided: (https://github.com/mdbresh/NN_trEFM)

Corresponding Author:

* David S. Ginger is the corresponding author: dginger@uw.edu

Funding Sources and Acknowledgements

This article is based primarily on work supported by the Department of Energy (DOE-SC0013957). M.D.B is supported by an NSF Graduate Student Fellowship under Grant No. DGE-2140004. Part of this work was conducted with instrumentation supported by the University of Washington Student Technology Fee at the Molecular Analysis Facility, a National Nanotechnology Coordinated Infrastructure site at the University of Washington, which is a user facility supported in part by the National Science Foundation (Grant ECC-1542101), the University of Washington, the Molecular Engineering & Sciences Institute, the Clean Energy Institute, and the National Institutes of Health. We acknowledge support by the State of Washington through the University of Washington Clean Energy Institute and the Washington Research Foundation.

2.7 References

(1) Giridharagopal, R.; Cox, P. A.; Ginger, D. S. Functional Scanning Probe Imaging of Nanostructured Solar Energy Materials. *Accounts of Chemical Research* **2016**, *49* (9), 1769–1776. https://doi.org/10.1021/acs.accounts.6b00255.

(2) Giridharagopal, R.; Precht, J. T.; Jariwala, S.; Collins, L.; Jesse, S.; Kalinin, S. v.; Ginger, D. S. Time-Resolved Electrical Scanning Probe Microscopy of Layered Perovskites Reveals

Spatial Variations in Photoinduced Ionic and Electronic Carrier Motion. *ACS Nano* **2019**, *13* (3), 2812–2821. https://doi.org/10.1021/acsnano.8b08390.

(3) Belianinov, A.; Kalinin, S. v.; Jesse, S. Complete Information Acquisition in Dynamic Force Microscopy. *Nature Communications* **2015**, *6*, 6550. https://doi.org/10.1038/ncomms7550.

(4) Kalinin, S. v.; Sumpter, B. G.; Archibald, R. K. Big-Deep-Smart Data in Imaging for Guiding Materials Design. *Nature Materials* **2015**, *14* (10), 973–980. https://doi.org/10.1038/nmat4395.

(5) Kelley, K. P.; Ziatdinov, M.; Collins, L.; Susner, M. A.; Vasudevan, R. K.; Balke, N.; Kalinin, S. v; Jesse, S.; Kelley, K. P.; Ziatdinov, M.; Collins, L.; Vasudevan, R. K.; Balke, N.; Kalinin, S. v; Jesse, S.; Susner, M. A. Fast Scanning Probe Microscopy via Machine Learning: Non-Rectangular Scans with Compressed Sensing and Gaussian Process Optimization. *Small* **2020**, *16* (37). https://doi.org/10.1002/smll.202002878.

(6) Martínez, M. J.; Shimpalee, S.; van Zee -, J. W.; Chen, G.; Sun, X.; Wang, J.; -, al; Atkinson, R. W.; Rodgers, J. A.; Hazard, M. W. Imaging via Complete Cantilever Dynamic Detection: General Dynamic Mode Imagingand Spectroscopy in Scanning Probe Microscopy. *Nanotechnology* **2016**, *27* (41), 414003. https://doi.org/10.1088/0957-4484/27/41/414003.

(7) Gordon, O. M.; Moriarty, P. J. Machine Learning at the (Sub)Atomic Scale: Next Generation Scanning Probe Microscopy. *Machine Learning: Science and Technology* **2020**, *1* (2), 023001. https://doi.org/10.1088/2632-2153/AB7D2F.

(8) Jesse, S.; Vasudevan, R. K.; Collins, L.; Strelcov, E.; Okatan, M. B.; Belianinov, A.; Baddorf, A. P.; Proksch, R.; Kalinin, S. v. Band Excitation in Scanning Probe Microscopy: Recognition and Functional Imaging. *The Annual Review of Physical Chemistry* **2014**, *65* (1), 519–536. https://doi.org/10.1146/annurev-physchem-040513-103609.

(9) Krull, A.; Hirsch, P.; Rother, C.; Schiffrin, A.; Krull, C. Artificial-Intelligence-Driven Scanning Probe Microscopy. *Communications Physics* **2020**, *3* (1). https://doi.org/10.1038/S42005-020-0317-3.

(10) Higgins, K.; Lorenz, M.; Ziatdinov, M.; Vasudevan, R. K.; Ievlev, A. v; Lukosi, E. D.; Ovchinnikova, O. S.; Kalinin, S. v; Ahmadi, M.; Higgins, K.; Ahmadi, M.; Lukosi, E. D. Exploration of Electrochemical Reactions at Organic-Inorganic Halide Perovskite Interfaces via Machine Learning in In Situ Time-of-Flight Secondary Ion Mass Spectrometry. *Advanced Functional Materials* **2020**, *30* (2001995). https://doi.org/10.1002/adfm.202001995.

(11) Kim, D.; Muckley, E. S.; Creange, N.; Wan, T. H.; Ann, M. H.; Quattrocchi, E.; Vasudevan, R. K.; Kim, J. H.; Ciucci, F.; Ivanov, I. N.; Kalinin, S. v; Ahmadi, M.; Kim, D.; Ahmadi, M.; Muckley, E. S.; Vasudevan, R. K.; Ivanov, I. N.; Kalinin, S. v. Exploring Transport Behavior in Hybrid Perovskites Solar Cells via Machine Learning Analysis of Environmental-Dependent Impedance Spectroscopy. *Advanced Science* **2021**, *8* (2002510). https://doi.org/10.1002/advs.202002510.

(12) Rashidi, M.; Wolkow, R. A. Autonomous Scanning Probe Microscopy in Situ Tip Conditioning through Machine Learning. *ACS Nano* **2018**, *12* (6), 5185–5189. https://doi.org/10.1021/ACSNANO.8B02208/ASSET/IMAGES/MEDIUM/NN-2018-022083_0006.GIF.

(13) Moerman, D.; Eperon, G. E.; Precht, J. T.; Ginger, D. S. Correlating Photoluminescence Heterogeneity with Local Electronic Properties in Methylammonium Lead Tribromide Perovskite Thin Films. *Chemistry of Materials* **2017**, *29* (13), 5484–5492. https://doi.org/10.1021/acs.chemmater.7b00235.

(14) Srivastava, M.; Howard, J. M.; Gong, T.; Rebello, M.; Dias, S.; Leite, M. S. Machine Learning Roadmap for Perovskite Photovoltaics. *J. Phys. Chem. Lett. 2021* **2021**, *12*, 7866–7877. https://doi.org/10.1021/acs.jpclett.1c01961.

(15) Giridharagopal, R.; Rayermann, G. E.; Shao, G.; Moore, D. T.; Reid, O. G.; Tillack, A. F.; Masiello, D. J.; Ginger, D. S. Submicrosecond Time Resolution Atomic Force Microscopy for Probing Nanoscale Dynamics. *Nano Letters* **2012**, *12* (2), 893–898. https://doi.org/10.1021/nl203956q.

(16) Karatay, D. U.; Harrison, J. S.; Glaz, M. S.; Giridharagopal, R.; Ginger, D. S. Fast Time-Resolved Electrostatic Force Microscopy: Achieving Sub-Cycle Time Resolution. *Review of Scientific Instruments* **2016**, *87* (5), 053702. https://doi.org/10.1063/1.4948396.

(17) Tirmzi, A. M.; Dwyer, R. P.; Jiang, F.; Marohn, J. A. Light-Dependent Impedance Spectra and Transient Photoconductivity in a Ruddlesden-Popper 2D Lead-Halide Perovskite Revealed by Electrical Scanned Probe Microscopy and Accompanying Theory. *Journal of Physical Chemistry C* **2020**, *124* (25), 13639–13648. https://doi.org/10.1021/acs.jpcc.0c04467.

(18) Kong, J.; Giridharagopal, R.; Harrison, J. S.; Ginger, D. S. Identifying Nanoscale Structure-Function Relationships Using Multimodal Atomic Force Microscopy, Dimensionality Reduction, and Regression Techniques. *Journal of Physical Chemistry Letters* **2018**, *9* (12), 3307–3314. https://doi.org/10.1021/acs.jpclett.8b01003.

(19) Harrison, J. S.; Waldow, D. A.; Cox, P. A.; Giridharagopal, R.; Adams, M.; Richmond, V.; Modahl, S.; Longstaff, M.; Zhuravlev, R.; Ginger, D. S. Noncontact Imaging of Ion Dynamics in Polymer Electrolytes with Time-Resolved Electrostatic Force Microscopy. *ACS Nano* **2019**, *13* (1), 536–543. https://doi.org/10.1021/acsnano.8b07254.

(20) Harrison, J. S.; Waldow, D. A.; Cox, P. A.; Giridharagopal, R.; Adams, M.; Richmond, V.; Modahl, S.; Longstaff, M.; Zhuravlev, R.; Ginger, D. S.; Nikiforov, M. P.; Gam, S.; Jesse, S.; Composto, R. J.; Kalinin, S. v. Morphology Mapping of Phase-Separated Polymer Films Using Nanothermal Analysis. *Macromolecules* **2019**, *43* (1), 536–543. https://doi.org/10.1021/acsnano.8b07254.

(21) Jiang, F.; Pothoof, J.; Muckel, F.; Giridharagopal, R.; Wang, J.; Ginger, D. S. Scanning Kelvin Probe Microscopy Reveals That Ion Motion Varies with Dimensionality in 2D

Halide Perovskites. *ACS Energy Letters* **2021**, *6* (1), 100–108. https://doi.org/10.1021/acsenergylett.0c02032.

(22) Liu, Y.; Ievlev, A. v; Borodinov, N.; Lorenz, M.; Xiao, K.; Ahmadi, M.; Hu, B.; Kalinin, S. v; Ovchinnikova, O. S.; Liu, Y.; Ahmadi, M.; Hu, B. Direct Observation of Photoinduced Ion Migration in Lead Halide Perovskites. *Advanced Functional Materials* **2020**, *31* (2008777). https://doi.org/10.1002/adfm.202008777.

(23) Miyahara, Y.; Cockins, L.; Grütter, P. Electrostatic Force Microscopy Characterization of Low Dimensional Systems. In *Kelvin Probe Force Microscopy*; Sadewasser, A., Glatzel, T., Eds.; Springer: Berlin, Heidelberg; Vol. 48, pp 177–199.

(24) Tennyson, E. M.; Gong, C.; Leite, M. S. Imaging Energy Harvesting and Storage Systems at the Nanoscale. *ACS Energy Letters* **2017**, *2*, 2761–2777. https://doi.org/10.1021/acsenergylett.7b00944.

(25) Somnath, S.; Smith, C. R.; Jesse, S.; Laanait, N. Pycroscopy - An Open Source Approach to Microscopy and Microanalysis in the Age of Big Data and Open Science. *Microscopy and Microanalysis* **2017**, *23* (S1), 224–225. https://doi.org/10.1017/s1431927617001805.

(26) Somnath, S.; Smith, C. R.; Laanait, N.; Vasudevan, R. K.; Ievlev, A.; Belianinov, A.; Lupini, A. R.; Shankar, M.; Kalinin, S. v; Jesse, S. *USID and Pycroscopy-Open Frameworks for Storing and Analyzing Spectroscopic and Imaging Data*; 2019.

(27) Kalinin, S. v.; Strelcov, E.; Belianinov, A.; Somnath, S.; Vasudevan, R. K.; Lingerfelt, E. J.; Archibald, R. K.; Chen, C.; Proksch, R.; Laanait, N.; Jesse, S. Big, Deep, and Smart Data in Scanning Probe Microscopy. *ACS Nano* **2016**, *10* (10), 9068–9086. https://doi.org/10.1021/acsnano.6b04212.

(28) Belianinov, A.; Vasudevan, R.; Strelcov, E.; Steed, C.; Yang, S. M.; Tselev, A.; Jesse, S.; Biegalski, M.; Shipman, G.; Symons, C.; Borisevich, A.; Archibald, R.; Kalinin, S. Big Data and Deep Data in Scanning and Electron Microscopies: Deriving Functionality from Multidimensional Data Sets. *Advanced Structural and Chemical Imaging*. Springer December 1, 2015. https://doi.org/10.1186/s40679-015-0006-6.

(29) Borodinov, N.; Neumayer, S.; Kalinin, S. v; Ovchinnikova, O. S.; Vasudevan, R. K.; Jesse, S. Deep Neural Networks for Understanding Noisy Data Applied to Physical Property Extraction in Scanning Probe Microscopy. *npj Computational Materials* **2018**, *25* (25). https://doi.org/10.1038/s41524-019-0148-5.

(30) Jesse, S.; Kalinin, S. v. Principal Component and Spatial Correlation Analysis of Spectroscopic-Imaging Data in Scanning Probe Microscopy. *Nanotechnology* **2009**, *20* (8), 085714. https://doi.org/10.1088/0957-4484/20/8/085714.

(31) Shea, D. E.; Giridharagopal, R.; Ginger, D. S.; Brunton, S. L.; Kutz, J. N. Extraction of Instantaneous Frequencies and Amplitudes in Nonstationary Time-Series Data. *IEEE Access* **2021**, *9*, 83453–83466. https://doi.org/10.1109/ACCESS.2021.3087595.

(32) Borodinov, N.; Bilkey, N.; Foston, M.; Ievlev, A. v; Belianinov, A.; Jesse, S.; Vasudevan, R. K.; Kalinin, S. v; Ovchinnikova, O. S. ARTICLE Application of Pan-Sharpening Algorithm

for Correlative Multimodal Imaging Using AFM-IR. *npj Computational Materials* **2019**, *5* (49). https://doi.org/10.1038/s41524-019-0186-z.

(33) Azuri, I.; Rosenhek-Goldian, I.; Regev-Rudzki, N.; Fantner, G.; Cohen, S. R. The Role of Convolutionsl Neural Networks in Scanning Probe Microscopy: A Review. *Beilstein Journal of Nanotechnology* **2021**, *12*, 878–901. https://doi.org/10.3762/bjnano.12.66.

(34) Coffey, D. C.; Ginger, D. S. Time-Resolved Electrostatic Force Microscopy of Polymer Solar Cells. *Nature Materials* **2006**, *5* (9), 735–740. https://doi.org/10.1038/NMAT1712.

(35) Reid, O. G.; Rayermann, G. E.; Coffey, D. C.; Ginger, D. S. Imaging Local Trap Formation in Conjugated Polymer Solar Cells: A Comparison of Time-Resolved Electrostatic Force Microscopy and Scanning Kelvin Probe Imaging †. *J. Phys. Chem. C.* **2010**, *114* (48), 20672–20677. https://doi.org/10.1021/jp1056607.

(36) Cox, P. A.; Glaz, M. S.; Harrison, J. S.; Peurifoy, S. R.; Coffey, D. C.; Ginger, D. S. Imaging Charge Transfer State Excitations in Polymer/Fullerene Solar Cells with Time-Resolved Electrostatic Force Microscopy. *Journal of Physical Chemistry Letters* **2015**, *6* (15), 2852–2858. https://doi.org/10.1021/ACS.JPCLETT.5B01360.

(37) Thornton, S. T.; Marion, J. B. Classical Dynamics of Particles and Systems. In *Classical Dynamics of Particles and Systems*; Thomsom Brooks/Cole, 2004; pp 100–117.

(38) Lundberg, S.; Lee, S.-I. A Unified Approach to Interpreting Model Predictions. *arXiv* **2017**.

(39) Rozemberczki, B.; Watson, L.; Bayer, P.; Yang, H.-T.; Kiss, O.; Nilsson, S.; Sarkar, R. The Shapley Value in Machine Learning. *arXiv* **2022**.

(40) Boashash, B. Estimating and Interpreting The Instantaneous Frequency of a Signal. I. Fundamentals. *Proceedings of the IEEE* **1992**, *80* (4), 520–538. https://doi.org/10.1109/5.135376.

(41) Schirmeisen, A.; Taskiran, A.; Fuchs, H.; Roling, B.; Murugavel, S.; Bracht, H.; Natrup, F. Probing Ion Transport at the Nanoscale: Time-Domain Electrostatic Force Spectroscopy on Glassy Electrolytes. *Applied Physics Letters* **2004**, *85* (11), 2053–2055. https://doi.org/10.1063/1.1790034.

(42) Dwyer, R. P.; Harrell, L. E.; Marohn, J. A. Lagrangian and Impedance-Spectroscopy Treatments of Electric Force Microscopy. *Physical Review Applied* **2019**, *10* (6), 64020–64052. https://doi.org/10.1103/PhysRevApplied.11.064020.

(43) Silveira, W. R.; Muller, E. M.; Ng, T. N.; Dunlap, D.; Marohn, J. A. High-Sensitivity Electric Force Microscopy of Organic Electronic Materials and Devices. In *Scanning Probe Microscopy: Electrical and Electromechanical Phenomena at the Nanoscale*; Kalinin, S. v., Gruverman, A., Eds.; Springer: New York, 2007; pp 788–832.

(44) Falcon, W.; The Pytorch Lightning Team. PyTorch Lightning. March 30, 2019.

(45) Kalinin, S. v; Ziatdinov, M.; Hinkle, J.; Jesse, S.; Ghosh, A.; Kelley, K. P.; Lupini, A. R.; Sumpter, B. G.; Vasudevan, R. K. Automated and Autonomous Experiments in Electron and

Scanning Probe Microscopy. *ACS Nano* **2021**, *15* (8), 12604–12627. https://doi.org/10.1021/acsnano.1c02104.

(46) Vasudevan, R. K.; Ziatdinov, M.; Vlcek, L.; Kalinin, S. v. Off-the-Shelf Deep Learning Is Not Enough, and Requires Parsimony, Bayesianity, and Causality. *npj Computational Materials*. Nature Research December 1, 2021. https://doi.org/10.1038/s41524-020-00487-0.

(47) Gal, Y.; Ghahramani, Z. Dropout as a Bayesian Approximation: Representing Model Uncertainty in Deep Learning. In *arXiv*; Proceedings of the 33rd International Conference on Machine Learning: New York, NY, 2015. https://doi.org/https://doi.org/10.48550/arXiv.1506.02142.

(48) Ghosh, A.; Sumpter, B. G.; Dyck, O.; Kalinin, S. v.; Ziatdinov, M. Ensemble Learning-Iterative Training Machine Learning for Uncertainty Quantification and Automated Experiment in Atom-Resolved Microscopy. *npj Computational Materials* **2021**, *7* (100). https://doi.org/10.1038/s41524-021-00569-7.

(49) Yaffe, O.; Chernikov, A.; Norman, Z. M.; Zhong, Y.; Velauthapillai, A.; van der Zande, A.; Owen, J. S.; Heinz, T. F. Excitons in Ultrathin Organic-Inorganic Perovskite Crystals. *Physical Review B* **2015**, *92* (045414). https://doi.org/10.1103/PhysRevB.92.045414.

(50) Kataoka, T.; Kondo, T.; Ito, R.; Sasaki, S.; Uchida, K.; Miura, N. Magneto-Optical Study on Excitonic Spectra in (C6H13NH3)2PbI4. *Physical Review B* **1993**, *47* (4), 2010–2018.

(51) Stoumpos, C. C.; Cao, D. H.; Clark, D. J.; Young, J.; Rondinelli, J. M.; Jang, J. I.; Hupp, J. T.; Kanatzidis, M. G. Ruddlesden-Popper Hybrid Lead Iodide Perovskite 2D Homologous Semiconductors. *Chemistry of Materials* **2016**, *28* (8), 2852–2867. https://doi.org/10.1021/acs.chemmater.6b00847.

(52) Yuan, H.; Yu, H.; Wang, J.; Li, K.; Ji, S. On Explainability of Graph Neural Networks via Subgraph Explorations. *Proceedings of te 38th International Conference on Machine Learning* **2021**.

(53) Titan Putri Hartono, N.; Thapa, J.; Tiihonen, A.; Oviedo, F.; Batali, C.; Yoo, J. J.; Liu, Z.; Li, R.; Fuertes Marrón, D.; Bawendi, M. G.; Buonassisi, T.; Sun, S. How Machine Learning Can Help Select Capping Layers to Suppress Perovskite Degradation. *Nature Communications* **2020**, *11*, 4172. https://doi.org/10.1038/s41467-020-17945-4.

(54) Albrecht, T. R.; Grütter, P.; Horne, D.; Rugar, D. Frequency Modulation Detection Using High-Q Cantilevers for Enhanced Force Microscope Sensitivity. *Journal of Applied Physics* **1991**, *69* (668), 668–673. https://doi.org/10.1063/1.347347.

Chapter 3: Multi-Output Convolutional Neural Network

Adapted from: Breshears, M. D., Giridharagopal, R. & Ginger, D. S. Multi-Output Convolutional Neural Network for Improved Parameter Extraction in Time-Resolved Electrostatic Force Microscopy Data. *In Prep.* (2025).

3.1 Overview

Time-resolved scanning probe microscopy methods, like time-resolved electrostatic force microscopy (trEFM), enable imaging of dynamic processes ranging from ion motion in batteries to electronic dynamics in microstructured thin film semiconductors for solar cells. Reconstructing the underlying physical dynamics from these techniques can be challenging due to the interplay of cantilever physics with the actual transient kinetics of interest in the resulting signal. Previously, quantitative trEFM used empirical calibration of the cantilever or feed-forward neural networks trained on simulated data to extract the physical dynamics of interest. Both these approaches are limited by interpreting the underlying signal as a single exponential function, which serves as an approximation but does not adequately reflect many realistic systems. Here, we present a multi-branched, multi-output convolutional neural network (CNN) that uses the trEFM signal in addition to the physical cantilever parameters as input. The trained CNN accurately extracts parameters describing both single-exponential and bi-exponential underlying functions, and more accurately reconstructs real experimental data in the presence of noise. This work demonstrates an application of physics-informed machine learning to complex signal processing tasks, enabling more efficient and accurate analysis of trEFM.

3.2 Introduction

Many systems, from new semiconductors for energy harvesting to new battery electrodes, exhibit electronic and ionic dynamics connected their nanoscale structure.[1–8] Probing these dynamics on natural length scales of the materials in question allows researchers to understand how morphological or structural heterogeneity influence performance.[4,6,9–13] Unlike optical microscopy, scanning probe microscopy (SPM) uses mechanical detection to map both morphological features and electronic properties of materials below the diffraction limit. These electronic properties include conductivity,[14,15] surface photovoltage,[3,5,6,16] and ion motion.[3,5,11] Time-resolved electrostatic force microscopy (trEFM) is a dynamic SPM technique that probes the evolution of the surface potential during photoexcitation in semiconductors, which is influenced by both electronic and ionic dynamics in mixed electronic/ionic conductors.[3,11,17] The perturbation of the surface potential is often assumed to follow a single-exponential response to an excitation, which is a satisfactory first approximation in many situations.[2,17–19] However, we also know that many systems are not well-characterized by a single time constant.[4,20] As a result, extending trEFM signal processing to account for multi-exponential dynamics would greatly extend its utility.

Machine learning (ML) tools have enabled efficient and accurate signal processing,[21–23] interpretation,[18] and reconstruction across a wide range of applications.[24–26] However, many traditional signal processing techniques rely on manual feature extraction[15,27] or domain-specific algorithms[22,28] that limit their ability to handle complex or noisy data. Recent advancements in

deep learning, specifically convolutional neural networks (CNNs), have demonstrated potential for generalizable signal processing that is robust to noise.[22,24,28–30] Specifically, the application of CNNs to learn hierarchical patterns in complex signals poses an opportunity for efficient and accurate parameter estimation in time-series data,[21,24,30] such as signals collected via dynamic SPM methods like trEFM. In the trEFM signal, the transient carrier dynamics we are interested in measuring are intrinsically coupled to the cantilever physics. Previously, we used a single-exponential calibration procedure to extract cantilever-independent time constants to describe the dynamics of interest.[2,17,31] To improve the fit on noisy data, we developed a feedforward neural network that took the relevant cantilever parameters and the frequency signal and output a time constant corresponding to a single-exponential perturbation to the surface potential.[18] However, both of these methods relied on a single-exponential approximation of the underlying dynamics. Here, we present a multioutput convolutional neural network (CNN) trained on simulated and experimental data, and show this approach yields improved parameter extraction for both underlying single- and bi-exponential kinetics and improved robustness to noisy signals.

3.3 Methods

3.3.1 Perovskite sample preparation

All preparation of perovskite samples was performed in a N_2 glovebox. The 1.2 M $Cs_{0.17}FA_{0.83}Pb(I_{0.85}Br_{0.15})_3$ solution was prepared by mixing the correct molar ratio of PbI_2 (TCI), $PbBr_2$ (Alpha Aesar), FAI (Greatcell Solar), and CsI (Alpha Aesar) in a 4:1 solvent ratio of N,N-Dimethylformamide (DMF) and Dimethyl sulfoxide (DMSO). 1.5 cm^2 indium tin oxide (ITO) coated glass substrates were cleaned by sequential sonication in DI water containing ~2% Micro-90 detergent, DI water, acetone, and isopropanol for 10 minutes each. The substrates were ozone-cleaned for 23 minutes prior to spincoating. Me-4PACz (TCI) was dissolved in DMF at a concentration of 50 mg/mL and subsequently diluted to 1 mg/mL in isopropanol. Approximately 60 µL of the 1 mg/mL Me-4PACz solution was deposited on the substrate and spincoated at 5000 rpm for 30 s with an acceleration of 800 rpm/s. The film was annealed at 100°C for 10 minutes. Next, 100 µL of a solution with the ratio 1:150 Al_2O_3 nanoparticles (Sigma Aldrich) to isopropanol was spincoated at 6000 rpm for 30 s with an acceleration of 800 rpm/s to wash off excess Me-4PACz and improve wettability. The substrates were annealed at 100°C for 30 s. Finally, 70 µL of the perovskite precursor solution were deposited on the substrate and spincoated at 1000 rpm for 10 s with an acceleration of 200 rpm/s followed by spinning at 5000 rpm for 35 s with an acceleration of 800 rpm/s; 10 s before the completion of the final spincoating step, 300 µL of anisole was dynamically deposited on the sample. The sample was annealed at 100°C for 45 minutes.

3.3.2 trEFM protocol

trEFM and the required experimental setup have been discussed in detail.[17,31] We performed our measurements on an Asylum Research MFP3D-BIO mounted on a Nikon inverted optical microscope. We used Pt-coated cantilevers (mikroMasch HQ/NSC15/Pt) driven at resonance frequency (~300 kHz) for all measurements. We mounted the sample in an inert glovebox environment in a sealed cell, then imaged under active flowing nitrogen in this sealed cell. We

recorded the cantilever oscillation using a 16-bit A/D digitizer (Dynamic Signals/GaGe Razor Express CSE1622), typically at 5 MS/s, and synced to the cantilever oscillation phase (180°) using custom trigger electronics (detailed circuit information can be found in our previous reports; additional information available upon request).[17,31] In an experimental window of 16 ms, we apply a bias of +10 V to the cantilever at t = 1 ms, we allow the sample to equilibrate for 4 ms. We digitize the cantilever oscillation starting at t = 4.6 ms through t = 8.6 ms, and trigger the laser excitation at t = 5 ms (turning off the laser at t = 7 ms). We used a 705 nm (Omicron PhoxXplus 705-40) continuous wavelength laser at an incident intensity of ~150 mW/cm^2 to excite our samples; we adjust the intensity using neutral density filters and the electrical power via software control. The laser was focused via a bottom objective on an inverted optical microscope and co-aligned with the cantilever tip. We measured the illumination intensity using the combination of a calibrated photodiode and a Pixera CCD camera (150CL-CU). We demodulated the raw cantilever deflection data using a Hilbert Transform to obtain the instantaneous frequency ($\Delta\omega(t)$). This code is freely available online via the FFTA Python package (https://github.com/GingerLabUW/FFTA).

3.3.3 Multi-output Neural Network Approach

We provide the code and example data online on GitHub (xxLINKxx). For the network itself, we used the PyTorch framework (v. 2.3.1 with Cuda 11.8). Our simulated training dataset varies the cantilever parameters k, Q, and ω according to the distributions in Appendix B Fig. 1. We vary τ_1 between 1 and 10 μs, τ_2 between 50 and 500 μs, and A (the coefficient) between 0 and 1 according to the distributions shown in Appendix B Fig. 2. During training, each label is normalized between 0 and 1 to prevent overcorrection during training and back propagation (generally, normalizing the labels makes the error gradients more uniform, leading to smoother and more efficient learning).[32–34] For initial training on simulated data, we use 10,000 traces total: 7,000 for training, 1,500 for validation, and 1,500 for testing. Results of random seed testing are shown in Appendix B Fig. 15; mean average error of trained network and R^2 scores comparing CNN-extracted and true parameters are consistent across multiple random seeds, supporting the generalizability of the approach.

3.3.4 Voltage Pulse Experiment to Obtain Labeled trEFM Data

To obtain labeled experimental data for fine tuning, we use a function generator (Agilent 33500B) to apply voltage pulses that follow a bi-exponential decay to a conductive substrate and capture the cantilever response. The voltage pulse method is time-consuming, where each frequency traces takes approximately 1-2 minutes to obtain. We use 500 voltage pulse traces (350 for training, 50 for validation, and 100 for testing) for fine tuning.[35–37]

3.4 Results and Discussion

3.4.1 The Limitations of the Single-exponential Model

Equation 1 shows the bi-exponential function, which approximates realistic underlying kinetics in various systems with more than a single underlying physical process, such as surface potential equilibration in mixed ionic/electronic conductors[4] or semiconductors with two populations of traps.[20,38–41]

$$y = Ae^{-\frac{t}{\tau_1}} + (1 - A)e^{-\frac{t}{\tau_2}} \qquad \textbf{Equation 1}$$

Here A is the coefficient that describes the relative contribution of each time constant, τ_1 and τ_2; A is constrained to be between 0 and 1. When A = 0 or 1, the underlying function follows a single-exponential function. In practice, there will be an additional overall amplitude term to encode the strength of the perturbation; however, we ultimately normalize our signals between 0 and 1 to avoid convolving the amplitude with the time-dependent kinetics of interest.

We have discussed the working principles and analytical workflow of trEFM in previous publications (additional details are also provided in Methods 2.2).[4,17,31] Briefly, we drive an SPM cantilever at a known frequency; when we photoexcite a semiconducting sample, we generate electronic carriers and, depending on the material, induce ion motion.[4,11] The evolution of these charged carrier profiles results in a transient equilibration of the surface potential of the material.[4] The change in the surface potential perturbs the electrostatic force gradient between the oscillating tip and sample, resulting in a perturbation to the oscillation frequency of the cantilever ($\Delta\omega(t)$).[17,19,31] Because we are driving the cantilever at a fixed frequency, after the initial perturbation to the electrostatic force gradient the cantilever's instantaneous frequency relaxes back to the drive frequency, meaning the transient response we are interested in probing is both coupled to and obfuscated by the cantilever physics.

Fig. 1 shows the experimental response of a real cantilever to a bi-exponential perturbation generated with a programmed voltage pulse applied to a conductive substrate (see Methods 2.4). The $\Delta\omega(t)$ trace shows an initial fast shift to a point of maximum deviation from the drive frequency (normalized to 0), and then a slow relaxation back to equilibrium drive frequency (normalized to 1). The magnitude of the frequency shift encodes information about the relative strength of the perturbation, but not the time-dependent kinetics we are interested in probing.[31] Additionally, the magnitude may be dependent on the state of the cantilever's tip.[19,31] We are interested in probing the time-dependent kinetics of the frequency shift, so here we normalize the signal. Previous work supports our hypothesis that the initial shift in $\Delta\omega(t)$ corresponds to transient charge carrier dynamics of interest.[4,18] The subsequent relaxation back to the drive frequency is primarily governed by the cantilever Q.[17–19,31] For bi-exponential perturbations, we calculate the $<\tau>$ as a weighted average of the time constants using Equation 2.

$$<\tau> = A \times \tau_1 + (1 - A) \times \tau_2 \qquad \textbf{Equation 2}$$

The dotted line in Fig. 1 shows a simulated signal governed by a single-exponential perturbation with a time constant of 170.12 μs, which we extracted using our previous feedforward neural network;[18] this τ markedly underestimates the true $<\tau>$ value of 277.85 μs. The simulated signal only approximately reconstructs our experimental data, with an R^2 score of 0.67, where a score of 1.0 would indicate perfect signal reconstruction. This degraded performance stands in contrast to the performance of the feedforward neural network on truly single-exponential data, extracting a τ value of 53.66 μs, compared to a true τ value of 58.81 μs, leading to a reconstruction R^2 score of 0.93.

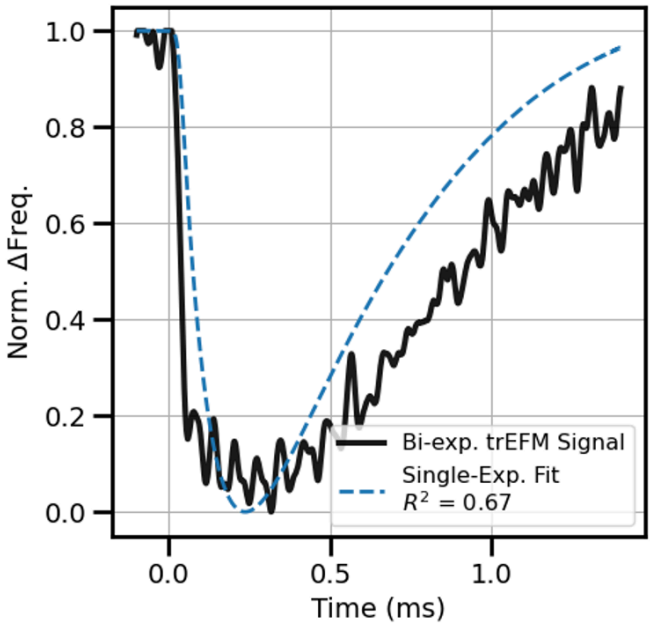

Figure 1: Example trEFM frequency trace governed by an underlying bi-exponential perturbation to the electrostatic force gradient with a <τ> of 277.85 μs, collected via the voltage pulse method described in Methods 2.4. The trigger for the bi-exponential voltage pulse is at t=0 ms. The Δω(t) trace is normalized such that a value of 1 represents the equilibrium drive frequency and a value of 0 represents the maximum shift in Δω(t). The blue dashed line is a simulated signal governed by a single-exponential perturbation with a τ value of 170.12 μs, extracted via a feedforward neural network from previous work.[18]

3.4.2 The Multi-Output Convolutional Neural Network Model

To regress to parameters that describe a more complex underlying function that follow Equation 1, we design a more complex neural network and train it on a broader set of simulated training data. We then test the trained network's performance on experimental data. Fig. 2 shows a schematic of our CNN architecture; the input includes the Δω(t) trace and the relevant physical cantilever parameters, which are easily obtained during the trEFM experiment. We use a PyTorch framework with a custom error function (see Appendix B Note 1 and Methods 2.3) and implement early stopping to prevent overfitting to our simulated data. We initially split the cantilever parameters from the input array containing the Δω(t) trace and we feed the Δω(t) signal into three convolutional branches. The convolution operation applies a filter (a kernel) to the signal, which helps the network detect and learn patterns in the data such as edges or noise.[28,42,43] We direct the network to pay attention to patterns of different timescales by changing the size of the kernel, where relatively smaller convolutional kernels learn faster patterns, like those in the initial shift in cantilever oscillation frequency, and relatively larger kernels learn patterns in the slower features, like the cantilever relaxation. In the fast and slow branches, we employ residual block layers to improve deep learning efficiency and gradient optimization for small variations in input data.[28,34,37] The weight branch is strictly a convolutional neural network, which we found best approximated the relative contributions from fast and slow processes.

When we train the network, each branch learns a latent representation of the Δω(t) trace. We concatenate the latent representations with the cantilever parameters and input those data into a shared features dense layer. In this step, we expect the network learns how the parameters contextualize the latent fast, slow, and weight patterns in the data. We direct the output of this dense layer into three branches that comprise two dense layers each. These simple feedforward branches regress on the contextualized latent representation of the signal and output each parameter: τ_1, τ_2, and A.

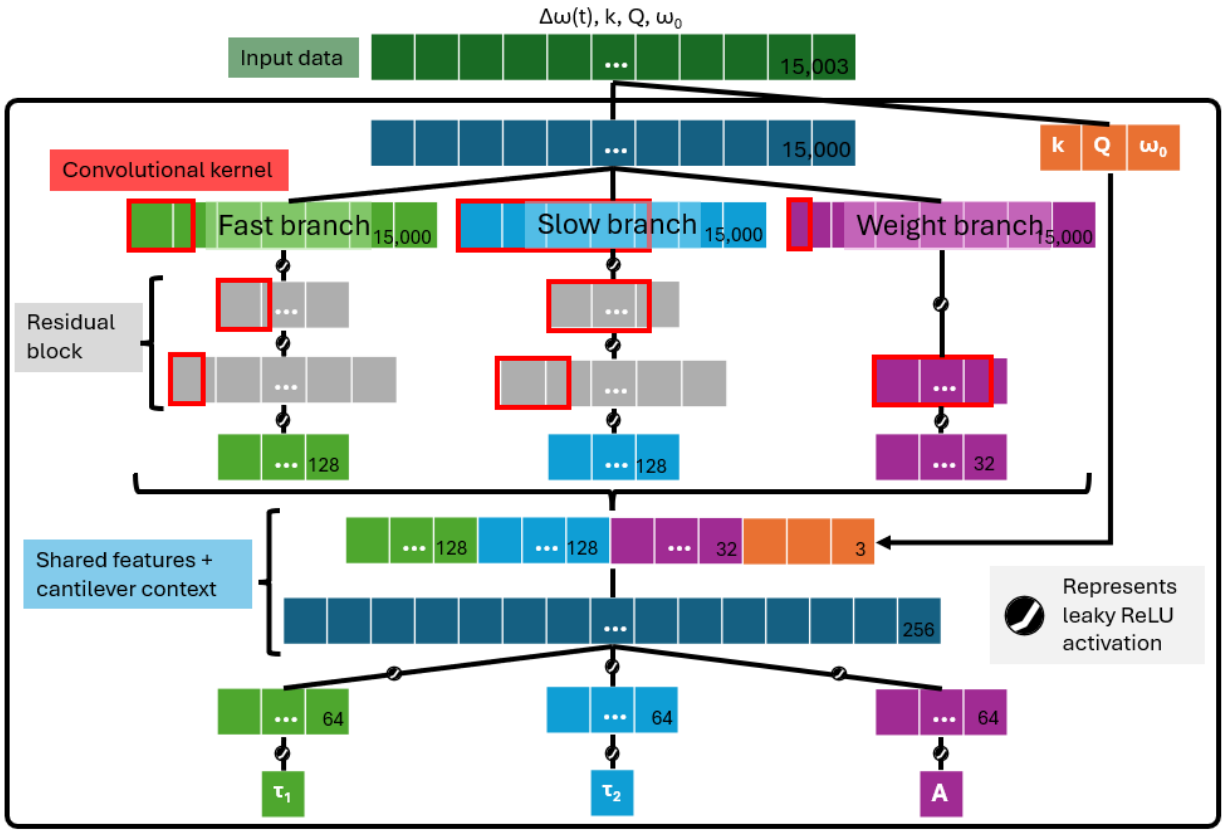

Figure 2: Schematic describing the multi-output convolutional neural network architecture, where the change in frequency (Δω(t)) is fed into three branches that learn the time-dependent features of the signal; the cantilever parameters (k, Q, and ω) are then concatenated with these latent representations of the Δω(t) signal. From the contextualized latent representations, three fully connected branches extract the relevant parameters given in Equation 1. Note that additional dropout regularization and batch normalization layers are not shown here; refer to [xxLINKtoGitHubxx] for the full network architecture.

Our initial training dataset for our new network comprises simulated Δω(t) traces and corresponding cantilever parameters. Appendix B Fig. 1 shows the distributions of k, Q, and ω we use to simulate our training data. In our simulated training dataset, we vary τ_1 between 1 and 10 μs, τ_2 between 50 and 500 μs, and A between 0.0 and 1.0 (Appendix B Fig. 2 shows distributions of these parameters used in our simulation). By constraining τ_1 to relatively faster times and τ_2 to slower times, the coefficient, A, represents the relative contributions of a "fast" and a "slow" component in the signal. From our previous work, we expect that the initial shift in frequency to its maximum deviation from the drive frequency contains the most information regarding the time

constants, and that the following frequency relaxation is primarily governed by cantilever physics (specifically Q).[4,17–19,31] Appendix B Fig. 3 shows how the initial transient response of the cantilever oscillation frequency is impacted by τ_1, τ_2, and A. After training the network, we evaluate its performance on simulated data; Appendix B Fig. 4 shows the network's performance on simulated test data. We aim for the network to handle experimental noise sources, such as thermal noise, limitations from the photodiode, or jitter in the trigger.[44,45]

3.4.3 Testing the Performance of the Trained CNN on Experimental Data

To ensure the network learns to interpret realistically noisy data, we apply voltage pulses that follow single- or bi-exponential decays to a with known time constant parameters to a conductive substrate, providing us with a dataset of labeled experimentally obtained signals that captures real experimental noise sources. We obtain the cantilever parameters k (N/m), Q (unitless) and ω (kHz) during the experiment to include in our new dataset. We do not use solely the voltage pulse data to train our network, as collecting sufficient labeled data on multiple cantilevers would take too long; rather, we fine tune our CNN model that was already trained on simulated data with a smaller dataset of voltage pulse traces.[36] We discuss the voltage pulse method experimental details in Methods 2.4. Appendix B Fig. 5 shows the parity plots of the test voltage pulse data, confirming that fine tuning enabled accurate parameter extraction on experimental data. The mean average error for τ_1 was 1.01 μs, for τ_2 was 35.87 μs, and for A was 0.04 (a mean percent error of 17.6%, 11.7%, and 8.3% respectively); and the R^2 score for each parameter's parity plot was 0.74, 0.79, and 0.97 respectively. Appendix B Note 2 discusses the variations in error metrics for the three parameters in detail.

We believe this level of accuracy should be sufficient for many if not most imaging applications; the trained model separates the two time constants and their relative contribution to the underlying kinetics of interest. Because we cannot assign precise physical processes to each parameter, we use $\langle\tau\rangle$ to summarize our network's overall performance. Fig. 3a shows a parity plot of $\langle\tau\rangle$ extracted from voltage pulse data. The mean average error is 17.1 μs (~11.5% error), with an R^2 value (comparing CNN-extracted $\langle\tau\rangle$ values to true $\langle\tau\rangle$ values) of 0.97. Because trEFM is an imaging technique, we construct an artificial image using the labeled experimental test voltage pulse signals, where each pixel contains the $\Delta\omega(t)$ trace from our voltage pulse dataset governed by a single- or bi-exponential underlying function. Appendix B Fig. 6 shows the map of τ_1, τ_2, and A for this artificial image and the CNN-extracted parameter maps. Fig. 3b shows the $\langle\tau\rangle$ map according to Equation 2. Fig. 3c shows the CNN-extracted $\langle\tau\rangle$ for our artificial image.

We demonstrate that the trained multi-output CNN accurately extracts the parameters that describe a single- or bi-exponential underlying function; we expect that these parameters also enable us to more accurately reconstruct the $\Delta\omega(t)$ signal. Given the CNN-extracted parameters, we simulate $\Delta\omega(t)$ traces and calculate the R^2 value to compare the reconstructed signal with the experimental input. Appendix B Fig. 7 shows the map of R^2 values for our artificial image, with an average R^2 of 0.97, confirming excellent signal reconstruction with the multi-output CNN. This performance is a significant improvement over the single-exponential feedforward network[18] which produces an average reconstruction R^2 score of only 0.79 (see Appendix B Fig. 7).

Convolutional neural networks are a well-established method for extracting information (or fitting parameters) from noisy data.[24,28,33,46] We hypothesize that by using a multi-output CNN (that assumes bi-exponential underlying kinetics) we can not only extract parameters closer to the ground truth but also extract accurate parameters from noisy data. Appendix B Fig. 8 shows the single-exponential feedforward network time constant and multi-output CNN $<\tau>$ values plotted against the signal-to-noise ratio (SNR) and the signal reconstruction R^2 score for each approach. From this analysis, we see that the multi-output CNN reconstructs the data with an R^2 score of 0.83 at an SNR as low as 5.85, whereas the single-exponential neural network results in a reconstruction R^2 score of 0.43. The multi-output CNN reconstruction R^2 score surpasses 0.9 when the SNR surpasses ~7, while the single-exponential neural network reconstruction R^2 score approaches 0.8 at an SNR of 15 (and never surpasses 0.81 even at higher SNR values). These results confirm that the multi-output CNN is more robust to noise than our previous feedforward network approach down to SNRs of ~7, indicating that the parameters extracted via the multi-output CNN more accurately represent the real dynamics of interest in the signal. Appendix B Note 3 discusses the resilience of the CNN to Gaussian noise further.

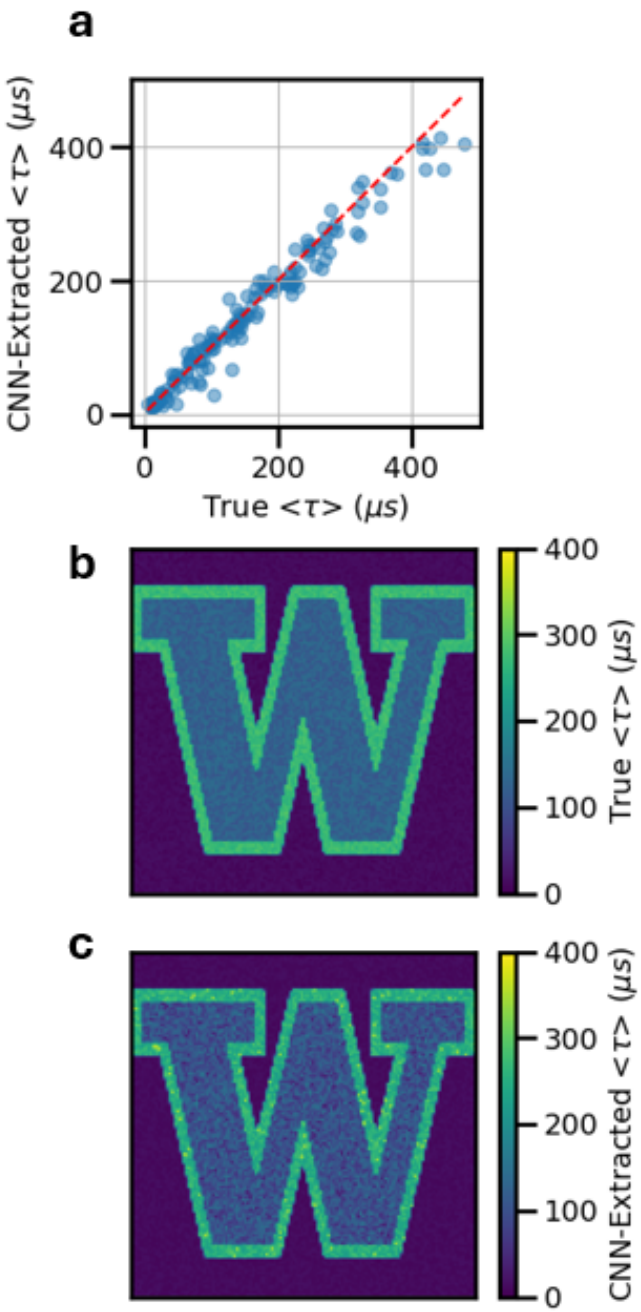

Figure 3: (a) Parity plot showing fine-tuned network performance on labeled experimental data; CNN-extracted <tau> values plotted against ground truth <tau> values calculated from Equation 2. (b) Artificially constructed ground truth image of <τ> values comprising labeled experimental data at each pixel. (c) CNN-extracted <τ> values recovered from the underlying experimental data at each pixel in the artificial image. Appendix B Fig. 6 show individual parameter maps for ground truth and CNN-extracted τ_1, τ_2, and A; overall signal reconstruction R^2 value is 0.97 (where 1.0 would indicate perfect signal reconstruction).

3.4.4 Model Explainability

Given the success of our network in reconstructing the <τ> from labeled training data, we now turn to examining the patterns the model learned. Model explainability is critical to trust and

transparency, bias detection, and user understanding of ML methods.[33,42,43,47] We previously used Shapley Additive exPlanations (SHAP)[47] to explore the impact of different features on our feedforward network's output, enabling us to confirm that the single-exponential network accurately interpreted the relevant cantilever parameters *and* learned intuitive patterns in the frequency signals.[18] Here, we apply SHAP to explore our more complex model and the impact of cantilever parameters and different parts of the frequency signal on each parameter output.

SHAP analysis reveals how every input into the network (e.g. Q for a particular cantilever or the $\Delta\omega(t)$ value at a given index) indicates the model output should be greater than or less than (or equal to) the mean model output.[18,47] An input that the model learned corresponds to an output that is greater than the mean model output has a positive SHAP value,[47] and a negative SHAP value corresponds to an output less than the mean model output. If an input at a given index has no effect on the resulting model prediction relative to its mean output, the SHAP value will be 0.

We explore the distributions of SHAP values across the varied cantilever parameters in our simulated test dataset to confirm that the trained CNN has learned the appropriate cantilever physics. Appendix B Fig. 9 shows the distributions of SHAP values across k, Q, and ω from this representative dataset. Importantly, Appendix B Fig. 9e shows that the model learned that signals collected with cantilevers that have high Q values typically represent faster underlying dynamics, which not only physically intuitive[17,19] but also reproduces the results from our previous work.[18]

Fig. 4 shows three example $\Delta\omega(t)$ traces colored by the SHAP value for the model output corresponding to the coefficient A. We see that the largest impact on the predicted coefficient, A, (the highest density of positive and negative SHAP values) lies along the initial frequency shift. The trace where A=0.1 has the slowest $\langle\tau\rangle$ (per Equation 2) and exhibits the highest density of negative SHAP values along its transient frequency shift, indicating the model learned that a slow frequency shift results in a lower contribution of fast τ_1. In contrast, the trace where A=0.9 has the fastest $\langle\tau\rangle$ (the largest contribution of fast τ_1) and exhibits a high density of positive SHAP values along its initial frequency shift, indicating the model learned that a fast frequency shift results in a higher contribution of fast τ_1. Appendix B Figs. 10-11 show example traces for the SHAP analysis on τ_1 and τ_2. These results confirm that the initial transient response has the most impact on the model output, and that the slow cantilever relaxation has little to no effect on the model's output compared to the mean.

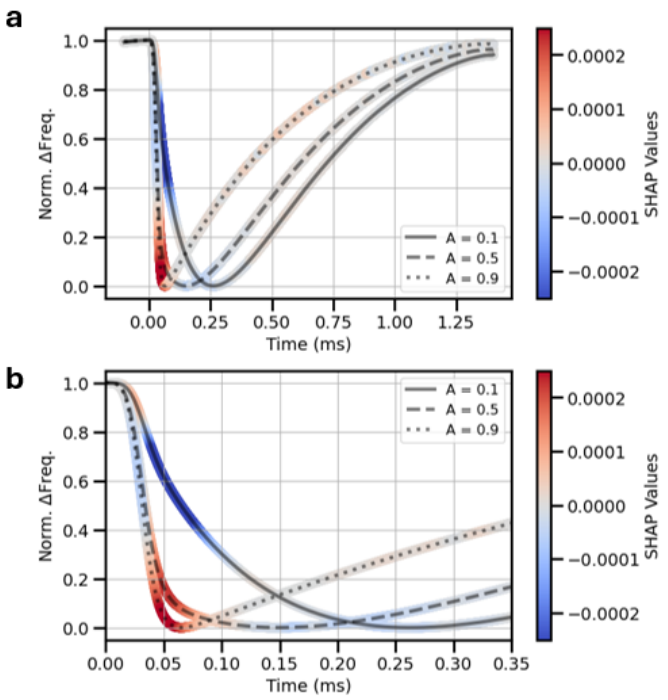

Figure 4: (a) Example Δω(t) traces with varied coefficient A values according to Equation 1, colored by SHAP values at each index, indicating the directional impact on the trained CNN each index has on the extracted coefficient A. Here, at t=0 ms the photoexcitation event is triggered. (b) Zoomed in on region immediately following trigger, showing varied densities of positive and negative SHAP values along initial transient frequency shift.

3.4.5 Signal Reconstruction on Unlabeled Experimental Data

Having demonstrated our multi-output CNN's ability to accurately reconstruct our data and withstand significant noise in the data and having explored feature importance with SHAP, we now apply the model to real, unlabeled experimental data. We performed trEFM on a mixed-cation, mixed-halide perovskite thin film device of the architecture and composition: ITO/Me-4PACz/$Cs_{0.17}FA_{0.83}Pb(I_{0.85}Br_{0.15})_3$. This composition is a useful, modern photovoltaic material for testing our approach on a real system of interest.[48] See Methods section for a detailed description of sample preparation and trEFM protocol.

After normalizing the Δω(t) trace at each pixel, we give the datacube to the trained CNN. Fig. 5a shows the 2×1 μm region of interest topography map. The sample exhibits 100-200 nm scale morphological features, commonly (if simplistically) referred to as "grains."[7,9,12] Given that these features cannot be resolved with optical microscopy, the fact that trEFM is a high-spatial resolution SPM technique makes it the ideal measurement tool for probing photoinduced dynamics.[4] Fig. 5b shows the $\langle\tau\rangle$ map (according to Equation 2) we extracted with the multi-output CNN. We see that the grain boundaries exhibit slower surface potential equilibration dynamics than grain interiors, a phenomenon we have previously observed in these materials.[4,11] Appendix B Fig. 12 shows the maps of τ_1, τ_2, and A, as extracted by the trained CNN. Given these parameters, we simulated Δω(t) traces for each pixel to evaluate how well the bi-exponential parameters reconstructed the experimental data. Appendix B Fig. 13 shows the map of R^2 values comparing the experimental and simulated data, showing an average R^2 score of 0.89. For comparison, we

feed the same data into our single-exponential feedforward neural network; Appendix B Fig. 14 shows the resulting τ map and the signal reconstruction R^2 map, with an average R^2 value of 0.71. These results indicate that the multi-output CNN extracts parameters that better reconstruct real experimental data, meaning the <τ> values we obtain with the CNN more accurately represent the charge carrier dynamics of interest.

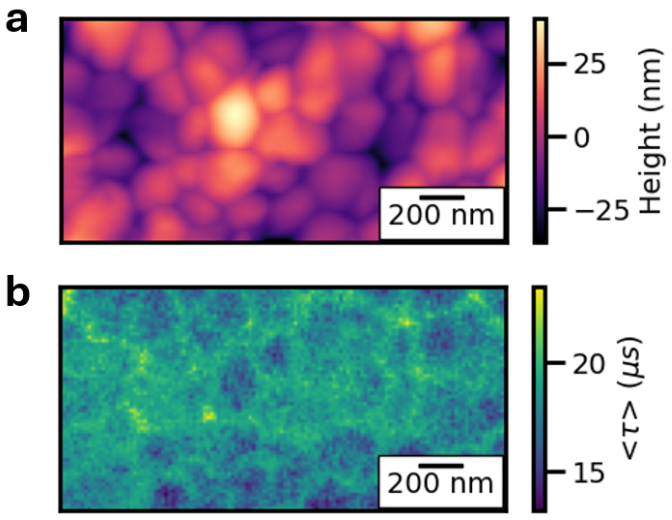

Figure 5: (a) Topography of 2×1 μm region of perovskite partial device (ITO/Me-4PACz/$FA_{0.83}Cs_{0.17}Pb(I_{0.85}Br_{0.15})_3$), which exhibits 100-200 nm scale morphological features. (b) CNN-extracted <τ> values at each pixel. trEFM data were collected with a 705 nm laser at 150 mW/cm^2 incident intensity. Appendix B Fig. 13 shows map of R^2 values comparing experimental data with simulated reconstructed signals, with an average R^2 value of 0.89.

3.5 Conclusion

We present a multi-branched, multi-output CNN trained on simulated data and fine tuned on labeled experimental data that efficiently and accurately extracts parameters that describe the underlying physical dynamics measured by trEFM. We demonstrate that the trained model extracts parameters which accurately reconstruct labeled and unlabeled experimental data. SHAP analysis reveals the importance of the initial shift in frequency on the extracted dynamics and confirms that the model correctly interpreted the role of cantilever physics on the resulting Δω(t) response. This work represents an application of physics-informed ML that offers a more robust and accurate analysis of dynamics in SPM signals, specifically of trEFM data, enabling more accurate signal reconstruction for interpreting the underlying kinetics of surface potential equilibration. The approach is highly generalizable to other underlying functions and techniques.

3.6 Acknowledgments

The atomic force microscopy imaging work (M.D.B.) was supported by the U.S. Department of Energy, Office of Basic Energy Sciences, Division of Materials Sciences and Engineering under Award DE-SC0013957. M.D.B. acknowledges support from the NSF Graduate Student Fellowship program under Grant no. DGE-2140004. D.S.G acknowledges salary and infrastructure support from the Washington Research Foundation, the Alvin L. and Verla R. Kwiram endowment, and the B. Seymour Rabinovitch Endowment.

3.7 References

(1) Giridharagopal, R.; Precht, J. T.; Jariwala, S.; Collins, L.; Jesse, S.; Kalinin, S. V.; Ginger, D. S. Time-Resolved Electrical Scanning Probe Microscopy of Layered Perovskites Reveals Spatial Variations in Photoinduced Ionic and Electronic Carrier Motion. *ACS Nano* **2019**, *13*, 2812–2821. https://doi.org/10.1021/acsnano.8b08390.

(2) Birkhold, S. T.; Precht, J. T.; Liu, H.; Giridharagopal, R.; Eperon, G. E.; Schmidt-Mende, L.; Li, X.; Ginger, D. S. Interplay of Mobile Ions and Injected Carriers Creates Recombination Centers in Metal Halide Perovskites under Bias. *ACS Energy Lett* **2018**, *3*, 52. https://doi.org/10.1021/acsenergylett.8b00505.

(3) Harrison, J. S.; Waldow, D. A.; Cox, P. A.; Giridharagopal, R.; Adams, M.; Richmond, V.; Modahl, S.; Longstaff, M.; Zhuravlev, R.; Ginger, D. S. Noncontact Imaging of Ion Dynamics in Polymer Electrolytes with Time-Resolved Electrostatic Force Microscopy. *ACS Nano* **2019**, *13*, 536–543. https://doi.org/10.1021/acsnano.8b07254.

(4) Harrison, J. S.; Waldow, D. A.; Cox, P. A.; Giridharagopal, R.; Adams, M.; Richmond, V.; Modahl, S.; Longstaff, M.; Zhuravlev, R.; Ginger, D. S.; Nikiforov, M. P.; Gam, S.; Jesse, S.; Composto, R. J.; Kalinin, S. V. Morphology Mapping of Phase-Separated Polymer Films Using Nanothermal Analysis. *Macromolecules* **2019**, *43*, 536–543. https://doi.org/10.1021/acsnano.8b07254.

(5) Pothoof, J.; Westbrook, R. J. E.; Giridharagopal, R.; Breshears, M. D.; Ginger, D. S. Surface Passivation Suppresses Local Ion Motion in Halide Perovskites. *J. Phys. Chem. Lett* **2023**, *14*, 6092–6098. https://doi.org/10.1021/acs.jpclett.3c01089.

(6) Breshears, M. D.; Pothoof, J.; Giridharagopal, R.; Ginger, D. S. Sub-Diffraction Imaging of Carrier Dynamics in Halide Perovskite Semiconductors: Effects of Passivation, Morphology, and Ion Motion. *ArXiv* **2024**.

(7) Jiang, F.; Pothoof, J.; Muckel, F.; Giridharagopal, R.; Wang, J.; Ginger, D. S. Scanning Kelvin Probe Microscopy Reveals That Ion Motion Varies with Dimensionality in 2D Halide Perovskites. *ACS Energy Lett.* **2021**, *6*, 100–108. https://doi.org/10.1021/acsenergylett.0c02032.

(8) Giridharagopal, R.; Cox, P. A.; Ginger, D. S. Functional Scanning Probe Imaging of Nanostructured Solar Energy Materials. *Acc. Chem. Res.* **2016**, *49*, 1769–1776. https://doi.org/10.1021/acs.accounts.6b00255.

(9) Tennyson, E. M.; Gong, C.; Leite, M. S. Imaging Energy Harvesting and Storage Systems at the Nanoscale. *ACS Energy Lett.* **2017**, *2*, 2761–2777. https://doi.org/10.1021/acsenergylett.7b00944.

(10) Garrett, J. L.; Tennyson, E. M.; Hu, M.; Huang, J.; Munday, J. N.; Leite, M. S. Real-Time Nanoscale Open-Circuit Voltage Dynamics of Perovskite Solar Cells. *Nano Lett.* **2017**, *17*, 2554–2560. https://doi.org/10.1021/acs.nanolett.7b00289.

(11) Jariwala, S.; Sun, H.; Adhyaksa, G. W. P.; Lof, A.; Muscarella, L. A.; Ehrler, B.; Garnett, E. C.; Ginger, D. S. Local Crystal Misorientation Influences Non-Radiative Recombination in Halide Perovskites. *Joule* **2019**, *3*, 3048–3060. https://doi.org/10.1016/j.joule.2019.09.001.

(12) DeQuilettes, D. W.; Vorpahl, S. M.; Stranks, S. D.; Nagaoka, H.; Eperon, G. E.; Ziffer, M. E.; Snaith, H. J.; Ginger, D. S. Impact of Microstructure on Local Carrier Lifetime in Perovskite Solar Cells. *Science (1979)* **2015**, *348* (6235), 683–686. https://doi.org/10.1126/SCIENCE.AAA5333.

(13) Tennyson, E. M.; S Doherty, T. A.; Stranks, S. D. Heterogeneity at Multiple Length Scales in Halide Perovskite Semiconductors. *Nat. Rev.* **2019**, *4*, 573–587. https://doi.org/10.1038/s41578-019-0125-0.

(14) Frohna, K.; Chosy, C.; Al-Ashouri, A.; Scheler, F.; Chiang, Y. H.; Dubajic, M.; Parker, J. E.; Walker, J. M.; Zimmermann, L.; Selby, T. A.; Lu, Y.; Roose, B.; Albrecht, S.; Anaya, M.; Stranks, S. D. The Impact of Interfacial Quality and Nanoscale Performance Disorder on the Stability of Alloyed Perovskite Solar Cells. *Nat Energy* **2024**. https://doi.org/10.1038/s41560-024-01660-1.

(15) Shi, Y.; Rojas-Gatjens, E.; Wang, J.; Pothoof, J.; Giridharagopal, R.; Ho, K.; Jiang, F.; Taddei, M.; Yang, Z.; Sanehira, E. M.; Irwin, M. D.; Silva-Acuñ, C.; Ginger, D. S. (3-Aminopropyl)Trimethoxysilane Surface Passivation Improves Perovskite Solar Cell Performance by Reducing Surface Recombination Velocity. *ACS Energy Lett.* **2024**, *7*, 4081–4088. https://doi.org/10.1021/acsenergylett.2c01766.

(16) Kong, J.; Giridharagopal, R.; Harrison, J. S.; Ginger, D. S. Identifying Nanoscale Structure-Function Relationships Using Multimodal Atomic Force Microscopy, Dimensionality Reduction, and Regression Techniques. *J. Phys. Chem. Lett.* **2018**, *9*, 3307–3314. https://doi.org/10.1021/acs.jpclett.8b01003.

(17) Akrami, F.; Jiang, F.; Giridharagopal, R.; Ginger, D. S. Kinetic Suppression of Photoinduced Halide Migration in Wide Bandgap Perovskites via Surface Passivation. *J. Phys. Chem. Lett* **2023**, *14*, 9310–9315. https://doi.org/10.1021/acs.jpclett.3c02570.

(18) Giridharagopal, R.; Rayermann, G. E.; Shao, G.; Moore, D. T.; Reid, O. G.; Tillack, A. F.; Masiello, D. J.; Ginger, D. S. Submicrosecond Time Resolution Atomic Force Microscopy for Probing Nanoscale Dynamics. *Nano Lett.* **2012**, *12*, 893–898. https://doi.org/10.1021/nl203956q.

(19) Breshears, M. D.; Giridharagopal, R.; Pothoof, J.; Ginger, D. S. A Robust Neural Network for Extracting Dynamics from Electrostatic Force Microscopy Data. *J. Chem. Inf. Model.* **2022**, *62* (18), 4342–4350.

(20) Tirmzi, A. M.; Dwyer, R. P.; Jiang, F.; Marohn, J. A. Light-Dependent Impedance Spectra and Transient Photoconductivity in a Ruddlesden-Popper 2D Lead-Halide Perovskite Revealed by Electrical Scanned Probe Microscopy and Accompanying Theory. *J. Phys. Chem. C* **2020**, *124*, 13639–13648. https://doi.org/10.1021/acs.jpcc.0c04467.

(21) Taddei, M.; Jariwala, S.; Westbrook, R. J. E.; Gallagher, S.; Weaver, A. C.; Pothoof, J.; Ziffer, M. E.; Snaith, H. J.; Ginger, D. S. Interpreting Halide Perovskite Semiconductor Photoluminescence Kinetics. *ACS Energy Lett.* **2024**, *9*, 2508–2516. https://doi.org/10.1021/acsenergylett.4c00614.

(22) Shea, D. E.; Giridharagopal, R.; Ginger, D. S.; Brunton, S. L.; Kutz, J. N. Extraction of Instantaneous Frequencies and Amplitudes in Nonstationary Time-Series Data. *IEEE Access* **2021**, *9*, 83453–83466. https://doi.org/10.1109/ACCESS.2021.3087595.

(23) Cuomo, S.; Di Cola, V. S.; Giampaolo, F.; Rozza, G.; Raissi, M.; Piccialli, F. Scientific Machine Learning Through Physics–Informed Neural Networks: Where We Are and What's Next. *J. Sci. Comput.* **2022**, *92* (88), 1–62.

(24) Yaman, M. Y.; Guye, K. N.; Ziatdinov, M.; Shen, H.; Baker, D.; Kalinin, S. V.; Ginger, D. S. Alignment of Au Nanorods along de Novo Designed Protein Nanofibers Studied with Automated Image Analysis. *Soft Matter* **2021**, *17*, 6109.

(25) Garcon, A.; Vexler, J.; Budker, D.; Kramer, S. Deep Neural Networks to Recover Unknown Physical Parameters from Oscillating Time Series. *PLoS One* **2022**, *17* (5 May). https://doi.org/10.1371/JOURNAL.PONE.0268439.

(26) Borodinov, N.; Bilkey, N.; Foston, M.; Ievlev, A. V; Belianinov, A.; Jesse, S.; Vasudevan, R. K.; Kalinin, S. V; Ovchinnikova, O. S. Application of Pan-Sharpening Algorithm for Correlative Multimodal Imaging Using AFM-IR. *Npj Comput. Mater.* **2019**, *5*. https://doi.org/10.1038/s41524-019-0186-z.

(27) Yaman, M. Y.; Kalinin, S. V.; Guye, K. N.; Ginger, D. S.; Ziatdinov, M. Learning and Predicting Photonic Responses of Plasmonic Nanoparticle Assemblies via Dual Variational Autoencoders. *Small* **2023**, *19*, 2205893.

(28) Jesse, S.; Kalinin, S. V. Principal Component and Spatial Correlation Analysis of Spectroscopic-Imaging Data in Scanning Probe Microscopy. *Nanotech.* **2009**, *20*, 085714. https://doi.org/10.1088/0957-4484/20/8/085714.

(29) Aloysius, N.; M, G. A Review on Deep Convolutional Neural Networks. In *International Conference on Communication and Signal Processing*; 2017; pp 0588–0592.

(30) Borodinov, N.; Neumayer, S.; Kalinin, S. V; Ovchinnikova, O. S.; Vasudevan, R. K.; Jesse, S. Deep Neural Networks for Understanding Noisy Data Applied to Physical Property Extraction in Scanning Probe Microscopy. *Npj Comput. Mater.* **2018**, *5*. https://doi.org/10.1038/s41524-019-0148-5.

(31) Fawaz, H. I.; Forestier, G.; Weber, J.; Idoumghar, L.; Muller, P.-A. Deep Learning for Time Series Classification: A Review. *Data Min Knowl Discov* **2019**, *33*, 917–963.

(32) Karatay, D. U.; Harrison, J. S.; Glaz, M. S.; Giridharagopal, R.; Ginger, D. S. Fast Time-Resolved Electrostatic Force Microscopy: Achieving Sub-Cycle Time Resolution. *Rev. Sci. Instrum.* **2016**, *87*, 053702. https://doi.org/10.1063/1.4948396.

(33) Siekmann, J.; Ravishankar, S.; Kirchartz, T. Apparent Defect Densities in Halide Perovskite Thin Films and Single Crystals. *ACS Energy Lett.* **2021**, *6*, 3244–3251. https://doi.org/10.1021/acsenergylett.1c01449.

(34) Krückemeier, L.; Liu, Z.; Krogmeier, B.; Rau, U.; Kirchartz, T.; Krückemeier, L.; Liu, Z.; Krogmeier, B.; Rau, U.; Kirchartz, T. Consistent Interpretation of Electrical and Optical Transients in Halide Perovskite Layers and Solar Cells. **2021**. https://doi.org/10.1002/aenm.202102290.

(35) Yuan, Y.; Yan, G.; Dreessen, C.; Rudolph, T.; Hülsbeck, M.; Klingebiel, B.; Ye, J.; Rau, U.; Kirchartz, T. Shallow Defects and Variable Photoluminescence Decay Times up to 280 Ms in Triple-Cation Perovskites. *Nature Materials* | **2024**, *23*, 391–397. https://doi.org/10.1038/s41563-023-01771-2.

(36) Krückemeier, L.; Liu, Z.; Kirchartz, T.; Rau, U. Quantifying Charge Extraction and Recombination Using the Rise and Decay of the Transient Photovoltage of Perovskite Solar Cells. **2023**. https://doi.org/10.1002/adma.202300872.

(37) Pandey, P.; Rai, A.; Mitra, M. Explainable 1-D Convolutional Neural Network for Damage Detection Using Lamb Wave. *Mech Syst Signal Process* **2022**, *164*, 108220.

(38) Borghesani, P.; Herwig, N.; Antoni, J.; Wang, W. A Fourier-Based Explanation of 1D-CNNs for Machine Condition Monitoring Applications. *Mech Syst Signal Process* **2023**, *205*, 110865.

(39) Freire, P. J.; Srivallapanondh, S.; Spinnler, B.; Napoli, A.; Costa, N.; Prilepsky, J. E.; Turitsyn, S. K. Computational Complexity Optimization of Neural Network-Based Equalizers in Digital Signal Processing: A Comprehensive Approach. *Journal of Lightwave Technology* **2023**, *42* (12), 4177–4200.

(40) Becherer, N.; Pecarina, J.; Nykl, S.; Hopkinson, K. Improving Optimization of Convolutional Neural Networks through Parameter Fine-Tuning. *Neural Comput Appl* **2019**, *31*, 3469–3479.

(41) Schumacher, Z.; Spielhofer, A.; Miyahara, Y.; Grutter, P. The Limit of Time Resolution in Frequency Modulation Atomic Force Microscopy by a Pump-Probe Approach. *Appl. Phys. Lett* **2017**, *110*, 53111. https://doi.org/10.1063/1.4975629.

(42) Albrecht, T. R.; Grütter, P.; Horne, D.; Rugar, D. Frequency Modulation Detection Using High-Q Cantilevers for Enhanced Force Microscope Sensitivity. *J. Appl. Phys.* **1991**, *69*, 668–673. https://doi.org/10.1063/1.347347.

(43) Zheng, H.; Shen, L.; Tang, A.; Luo, Y.; Hu, H.; Du, B.; Tao, D. Learn From Model Beyond Fine-Tuning: A Survey. *IEEE* **2023**, *14* (8), 1–20.

(44) Song, H.; Kim, M.; Park, D.; Shin, Y.; Lee, J.-G. Learning From Noisy Labels with Deep Neural Networks: A Survey. *IEEE Trans Neural Netw Learn Syst* **2023**, *34*, 8135–8153.

(45) Herwig, N.; Borghesani, P. Explaining Deep Neural Networks Processing Raw Diagnostic Signals. *Mech Syst Signal Process* **2023**, *200*, 110584.

(46) Lundberg, S.; Lee, S.-I. A Unified Approach to Interpreting Model Predictions. *ArXiv* **2017**. https://doi.org/http://arxiv.org/abs/1705.07874.

(47) Kosmatos, K. O.; Theofylaktos, L.; Giannakaki, E.; Deligiannis, D.; Konstantakou, M.; Stergiopoulos, T. Methylammonium Chloride: A Key Additive for Highly Efficient, Stable, and Up-Scalable Perovskite Solar Cells. *Energy Environ. Mater.* **2019**, *2*, 79–92. https://doi.org/10.1002/eem2.12040.

(48) Dai, Z.; Heckel, R. Channel Normalization in Convolutional Neural Networks Avoids Vanishing Gradients. **2019**.

(49) Kaur, R.; Kumar, R.; Gupta, M. Review on Transfer Learning for Convolutional Neural Network. In *3rd International Conference on Advances in Computing, Communication Control and Networking*; 2021; pp 922–926.

Chapter 4: Sub-Diffraction Imaging of Carrier Dynamics in Halide Perovskite Semiconductors: Effects of Passivation, Morphology, and Ion Motion

Adapted from: Breshears, M. D., Pothoof, J., Giridharagopal, R. & Ginger, D. S. Sub-diffraction Imaging of Carrier Dynamics in Halide Perovskite Semiconductors: Effects of Passivation, Morphology, and Ion Motion. *ArXiv* (2024).

4.1 Overview

We spatially resolve photocarrier dynamics in halide perovskites using time-resolved electrostatic force microscopy (trEFM) to map surface potential equilibration during photoexcitation. We compare several passivation agents including (3-aminopropyl)trimethoxysilane (APTMS), [3-(2-aminoethylamino)propyl]trimethoxysilane (AEAPTMS), and phenethylammonium iodide (PEAI). We obtain trEFM maps that reflect surface recombination velocity and carrier lifetimes and validate them with time-resolved photoluminescence imaging at large scales, while revealing high-resolution functional information that cannot be resolved with diffraction-limited imaging. We further validate the interpretation of sub-diffraction trEFM through wavelength- and intensity-dependent measurements, and with drift-diffusion simulations. The results reveal heterogeneity in surface potential equilibration times that correlates with perovskite film morphology and nanoscale variations in recombination dynamics following surface passivation. These data provide insight into the passivation of defects and grain boundaries and reveal there is still potential to further improve surface passivation through process control, while extending the utility of trEFM into the realm of high-efficiency semiconductors.

4.2 Introduction

Halide perovskite semiconductors have numerous applications including solar cells,[1,2] light-emitting diodes,[2,3] radiation detectors,[4] and even sources of quantum light.[5] Their advantages include scalable additive manufacturing, large absorption coefficients, bandgap tunability,[6] and high defect tolerance.[2] While perovskites are defect tolerant, they are not defect free.[2,7–11] Passivation strategies to reduce surface recombination velocity (SRV) by a factor of ~100 have improved perovskite device efficiencies over the last several years.[7,12–17] At the same time, ion motion, linked to phase segregation and electrochemical reactions, can be a limiting factor in perovskite semiconductor performance and stability.[18–26] Probing these effects at the device level is useful, but inherently reflects average values given the heterogenous nature of halide perovskite thin films,[8,9,27–29] and understanding how local film microstructure correlates with both electronic and ionic defects could advance materials processing.[8,9,28,30–33]

Indeed, microscopy tools that elucidate the relationship between local structure and nonradiative recombination have already proven useful for analyzing and improving semiconductor performance.[8,20,28,30,31,34–37] Time-resolved photoluminescence (trPL) probes electronic carrier recombination processes in perovskite materials;[38,39] and with confocal microscopy, we can obtain spatially resolved trPL maps at the optical diffraction limit. However, current best-in-class

perovskites comprise mixed-cation, mixed-halide compositions with grains that are often ~100 nm or smaller,[40–42] which is far below the optical diffraction limit with visible light. Other techniques, such as cathodoluminescence microscopy, can map carrier recombination dynamics on the nanoscale using an electron beam but often damage the sample in the process.[34,43] The ideal microscopy tool for advancing cutting edge perovskites would thus allow for measurement of carrier recombination dynamics at nanometer scale resolution without damaging the sample.

Time-resolved electrostatic force microscopy (trEFM), a scanning probe microscopy technique among the family of methods capable of providing fast electronic dynamics,[44–49] uses a mechanical cantilever to sense dynamic changes in the local electrostatic force gradient between the tip and the sample during photoexcitation.[31,32,50–52] To date, we have used trEFM to measure systems with large exciton binding energies such as organic photovoltaics and layered Ruddlesden-Popper perovskites.[31,32,45,51–56] In mixed-cation, mixed-halide perovskite systems where photoexcitation leads to free carriers, we expect the time-dependent changes measured should readily probe local recombination rates rather than be quantum efficiency-limited.

Here, we compare high-resolution trEFM images with spatially averaged trPL and drift-diffusion simulations. We show that trEFM measures the time it takes for surface potential to equilibrate as controlled by the evolution of electronic and ionic carrier concentrations during photoexcitation, and we probe the effects of chemical passivation on electronic carrier recombination and of local defect-mediated ion migration.

We demonstrate that treatments with different surface passivators, including (3-aminopropyl)trimethoxysilane (APTMS),[14–16] [3-(2-aminoethylamino)propyl]trimethoxysilane (AEAPTMS),[14] and phenethylammonium iodide (PEAI),[57,58] result in slower surface potential equilibration times due to reduced surface recombination velocities. We find that the local carrier dynamics vary with the perovskite morphology, where grain boundaries exhibit slower photoinduced dynamics than grain interiors. Through a combination of wavelength- and intensity-dependent experiments and drift-diffusion simulations, we show the competing influence of electronic carrier recombination and mobile ions on the surface potential equilibration time. We attribute the slower surface potential equilibration times following chemical passivation to the suppression of SRV; we ascribe the slower surface potential equilibration time observed at grain boundaries to locally higher defect densities that mediate slow ion migration and incur increased trap-mediated electronic carrier motion. Importantly, we show that surface potential equilibration times measured by trEFM correlate directly with minority carrier lifetimes and SRVs as measured by trPL. Our results connect the properties measured by trEFM with established optical characterization techniques and verify that trEFM can be a predictive tool for evaluating carrier recombination dynamics in modern halide perovskites with sub-diffraction-limited resolution, while also demonstrating that even common, effective surface passivation schemes can still exhibit local heterogeneity.

4.3 Results and Discussion

Fig. 1a shows a schematic of the trEFM experiment we use to probe carrier dynamics below the diffraction limit.[51,52] Here, we photoexcite the sample through the ITO substrate using a laser with

a rise time of ~2 ns and record the evolution of the mechanical cantilever dynamics to capture the transient electronic response of the sample. Fig. 1b shows the timing diagram of the excitation. Following photoexcitation, the carrier populations generated by the illumination will evolve to a new equilibrium. The time-dependence of these processes leads to a time-dependent change in the surface potential, surface capacitance, and dissipative properties of the sample,[44,45,51,52] and these shifts lead to transient deviations of the cantilever motion from the steady-state sinusoidal motion of a damped, driven harmonic oscillator.[59] These transient deviations encode information about short time dynamics of the local electronic environment's approach to a new equilibrium, which can be reconstructed via empirical calibration,[51] or even simulation and machine learning approaches.[56,60] Fig. 1c shows a representative cantilever frequency shift over time in response to photoexcitation. We obtain this frequency shift by demodulating the cantilever's oscillation (see Methods and Appendix C Note 1). The rapid shift in the cantilever's frequency following photoexcitation captures the transient dynamics of interest; following that, the cantilever relaxes to its resonance frequency on timescales governed by the cantilever quality factor, Q. We fit the frequency vs. time trace to a product of two exponentials (black dashed line in Fig. 1c), which enables us to find the time it takes for the cantilever to reach its maximum frequency deviation. We calibrate this time against the simulated response to excitation events with a defined time constant to extract a cantilever-independent time constant, τ (see Methods, Appendix C Note 1, and Appendix C Fig. 1).[51,52] Next, we show that this time constant reflects the surface potential equilibration time in halide perovskites.

The surface potential equilibration time is controlled by the sample's electronic carrier recombination dynamics and illumination conditions. First, we show there is a qualitative correlation between trEFM and confocal PL microscopy over large length scales on a partial perovskite device stack (or "half-stack)" with the architecture ITO/Me-4PACz/$Cs_{0.17}FA_{0.83}Pb(I_{0.75}Br_{0.25})_3$. This perovskite formulation is known to exhibit PL heterogeneity on the multi-micron-scale.[61] Fig. 1d shows a map of surface potential equilibration times in a 17.6×10 μm region-of-interest (ROI) as measured by trEFM, with empirical time constants on the microsecond-scale. Appendix C Fig. 2a shows the topography of this ROI. After imaging the sample with trEFM, we perform correlated confocal PL microscopy (see Methods). Fig. 1e shows the PL intensity map of the ROI. Fig. 1f shows correlated line traces (marked by the dashed lines in Fig. 1d,e), where slower surface potential equilibration times measured by trEFM correspond to brighter PL. Annotations on Fig. 1f show average minority carrier lifetime values collected at the corresponding positions shown in Fig. 1e, confirming that slower surface potential equilibration times measured by trEFM not only correlate to brighter PL, but also, qualitatively longer minority carrier lifetimes. Appendix C Fig. 2b shows a positive correlation between local surface potential equilibration times measured by trEFM and carrier dynamics measured by trPL in this image, with a Pearson correlation coefficient of 0.88 (with a p-value of 0.018).

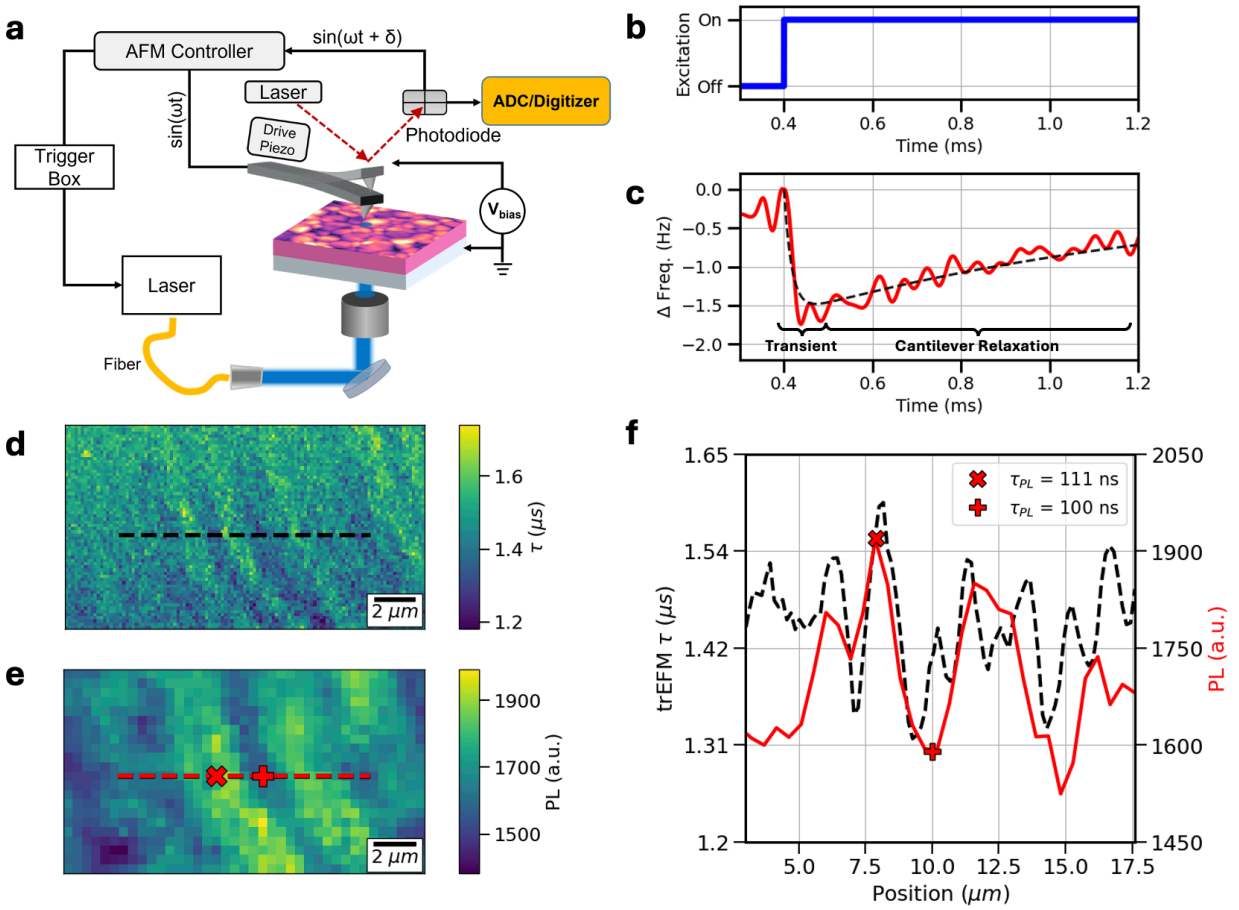

Fig. 1: trEFM measures photoinduced dynamics that correlate to PL metrics of interest. (a) trEFM schematic, where ADC refers to an analog-to-digital converter. (b) Excitation protocol for typical trEFM experiment. (c) Change in instantaneous frequency of cantilever after excitation, where the black dashed line shows an empirical fit of the product of two exponentials which describe the transient perturbation of interest and the cantilever relaxation (see Appendix C Note 1). (d) trEFM map of photoinduced dynamics across a 17.6×10 μm ROI on a sample with the formulation $Cs_{0.17}FA_{0.83}Pb(I_{0.75}Br_{0.25})_3$ collected using 705 nm excitation at an incident intensity of 100 mW/cm^2; Appendix C Fig. 2a shows the topography of this ROI. (e) Correlated PL map of the same ROI, taken using 60× objective, NA=0.7, using a 640 nm laser at a fluence of 105 nJ/cm^2. (f) Correlated line traces from the dotted lines shown in (d) and (e), where the trEFM line trace was smoothed to reduce pixel-to-pixel noise. Markers on (f) indicate positions shown in (e) where time-correlated single photon counting histograms were collected and fit with a stretched exponential (see Appendix C Note 2) to extract carrier lifetimes shown in legend (see Appendix C Fig. 2b for additional PL lifetimes collected in this ROI and corresponding correlated surface potential equilibration times).

To further examine this correlation between trEFM equilibration times and electronic carrier dynamics, we investigate the effects of three established surface passivation agents: APTMS,[14–16] AEAPTMS,[14] and PEAI.[57,58] We prepared half-stacks with the architecture glass/ITO/Me-4PACz/$Cs_{0.22}FA_{0.78}Pb(I_{0.85}Br_{0.15})_3$. Appendix C Figs. 3-4 show UV-vis absorbance, XRD, PL, and trPL characterization for the half-stacks. The samples each exhibit Gaussian-shaped PL spectra with a PL maximum at 755 nm, consistent with literature reports for this composition.[62] We fit the trPL decays using stretched exponential functions[38] and summarize the fit parameters in Appendix C Table 1. From the half-stack PL data, we extract an 18×, 2×, and 2× improvement in the carrier lifetime for APTMS, AEAPTMS, and PEAI treatments respectively. Appendix C Fig. 5 show the

average PL quantum yields for each half-stack, which show a 13×, 4×, and 2× improvement for APTMS, AEAPTMS, and PEAI respectively. We attribute these enhancements to a reduction in nonradiative recombination pathways.[7,14–17,63]

Fig. 2a shows the surface potential equilibration times we measured with trEFM on untreated and passivated samples plotted against the PL lifetime measured by trPL for those samples. Appendix C Fig. 6 show the trEFM maps for these samples and Appendix C Fig. 4 and Appendix C Table 1 summarize the trPL measurements. We see that the extracted surface potential equilibration time scales proportionally to the carrier lifetime as measured on perovskite half-stacks before and after passivation. These trends are consistent with our interpretation of trEFM probing the time it takes for the surface potential to equilibrate during photoexcitation, largely influenced by the time it takes for carriers to reach new equilibrium profiles. As we reduce nonradiative recombination pathways via passivation, we observe slower surface potential equilibration times that correspond to enhanced minority carrier lifetimes, consistent with general carrier generation and recombination kinetics.[64] However, consistently, the dynamics measured via trEFM are an order of magnitude larger than the average carrier lifetime measured via trPL, indicating that we are not measuring the trPL lifetime with trEFM. This difference is due to the nature of each experiment: trPL probes carrier population decay after pulsed excitation, while trEFM probes the evolution of the carrier population to a new equilibrium distribution in response to a step-function in photoexcitation.

In Fig. 2b, we compare the trEFM time constant with the SRV computed from the trPL data following Wang et al.[13] (see Appendix C Note 3 for additional information on this calculation). We find a strong inverse linear relationship between the dynamics measured by trEFM and the log of the SRV with a Pearson correlation coefficient of -0.91 (with a p-value of 0.013), where a value of -1.0 would indicate a perfect inverse correlation. These results show that the surface potential equilibration time measured by trEFM is predictive of the local SRV, meaning we can use trEFM to characterize treatments for the suppression of nonradiative recombination at perovskite surfaces.

The direct correlation we show between trEFM equilibration times and SRV underpins the opportunity to image carrier dynamics below the optical diffraction limit. Figs. 2c,d show the topography and surface potential equilibration times measured across a 2×1 μm region of an unpassivated perovskite half-stack. We measure surface potential equilibration times that range from 3.7 – 5.6 μs, with grain boundaries exhibiting slower dynamics than grain interiors. Figs. 2e,f show the topography and surface potential equilibration time images for an APTMS-treated sample; APTMS polymerizes on the surface of the sample, changing the observed topography.[15,18,19] As expected from the above analysis, the equilibration times measured by trEFM are indeed significantly (~6×) slower after passivation. Furthermore, we can no longer differentiate grain interiors from grain boundaries. However, we still observe heterogeneous equilibration times across the ROI, indicating that passivated samples still exhibit local heterogeneity in SRV. We show in Appendix C Fig. 7 and Appendix C Table 2 that these results are consistent across different regions and samples.

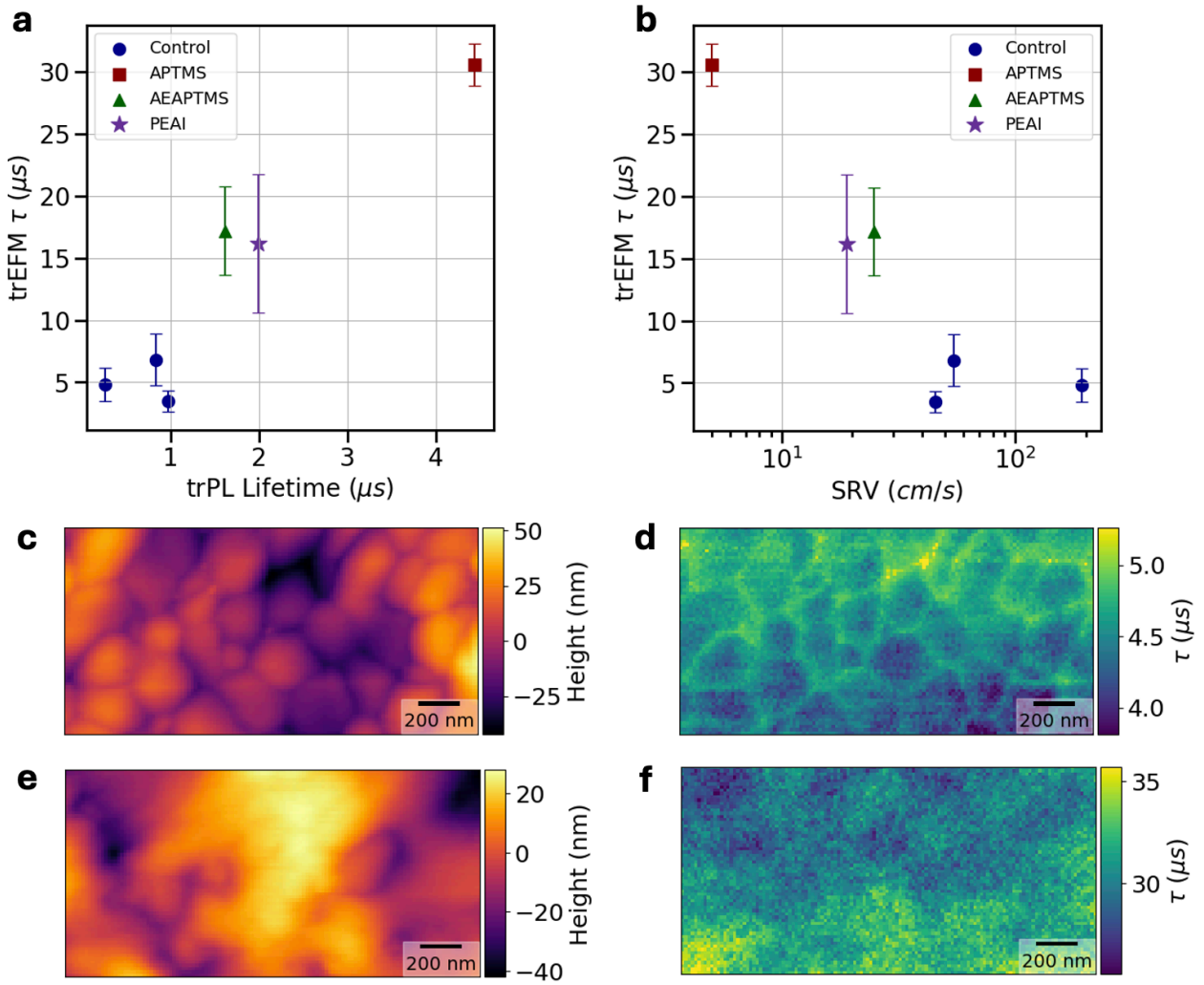

Fig. 2: Photoinduced dynamics measured by trEFM correlate to PL lifetime and (inversely) to SRV, revealing nanoscale heterogeneity on unpassivated and passivated samples. (a) Average trEFM τ values plotted against minority carrier lifetimes measured by trPL and (b) approximated SRV (see Appendix C Note 3 for SRV calculation). All trPL measurements were carried out using a pulsed 640 nm laser operated at ~30 nJ/cm^2 – enough to generate 2×10^{15} cm^{-3} carriers (1-2 Suns). (c) Topography of untreated half-stack and (d) corresponding trEFM τ map. (e) Topography of sample after APTMS-passivation with (f) trEFM τ map. All trEFM experiments here used a 405 nm laser with an incident intensity of ~150 mW/cm^2 (1.5 Suns) operated in a quasi-steady state regime.

The data so far support our hypothesis that trEFM dynamics probe carrier equilibration during photoexcitation, as dominated by SRV. To further examine this hypothesis, we use the open source 1D drift-diffusion simulator IonMonger, which enables us to explore the effects of various physical parameters, such as mobile ion concentration, excitation wavelength and intensity, and carrier recombination rates, on surface potential dynamics.[65–67] To reproduce our experimental setup, we model a device stack with an inverted, p-i-n architecture and we extract the potential evolution at the active layer surface. We find that the simulated surface potential equilibrates on the microsecond timescale, dependent on both the electronic carrier concentration and mobile ion concentration evolution, consistent with our experimental observations. Appendix C Note 4

describes the relationship between electronic and ionic carrier populations and the surface potential evolution further.

Fig. 3a shows the simulated surface potential evolution as a function of SRV ranging from 0.1 to 1000 cm/s, spanning the range of expected experimental values for untreated and treated films,[12,13,16,38] and Fig. 3b shows the simulated surface potential equilibration time plotted against SRV. As we decrease SRV, the simulated surface potential takes longer to reach the new steady-state, in agreement with the experimental trends from trEFM (Fig. 2b). This result is consistent with general behavior of rate equations and approach to equilibrium, where carrier generation rate is equal to recombination rate: if we decrease the recombination rate by suppressing SRV, then we will reach equilibrium more slowly (see Appendix C Note 4). While we are not attempting to simulate the full 3D system quantitatively, the excellent qualitative agreement between the experimental and simulated timescales further supports our physical interpretation that changes in surface potential equilibration times upon passivation (Fig. 2a,b) are primarily due to suppression of SRV. Appendix C Figs. 8-9 show the relationship between simulated surface potential equilibration time and bulk nonradiative and bimolecular recombination processes. Appendix C Table 3 contains complete simulation parameter details.

We next turn to interpreting the slower trEFM kinetics at the grain boundaries observed in our unpassivated samples. So far, we have established that known reductions in nonradiative recombination result in slower surface potential equilibration times, clearly showing that trEFM dynamics correlate with minority carrier lifetimes and SRVs. However, Fig. 2d shows that defect-rich grain boundaries in unpassivated samples also exhibit relatively slower equilibration times. In our previous work on 2D butylammonium lead iodide (BA_2PbI_4) perovskite materials, we also observed slower trEFM dynamics at grain boundaries, which we proposed are caused by increased contributions from slow ionic motion or trap-mediated electronic carrier transport.[32]

We now support this hypothesis with additional simulations of ion motion. Fig. 3c shows the simulated surface potential evolution as a function of the mobile ion concentration ranging from 1×10^{14} cm^{-3} to 1×10^{17} cm^{-3}, fixing the ion diffusion coefficient at 1×10^{-13} cm^2s^{-1} (parameter details are available in Appendix C Table 3).[68–74] Fig. 3d shows the simulated equilibration times as a function of mobile ion concentration, where higher mobile ion concentrations result in relatively slower surface potential equilibration times. This observation is supported by Poisson's Equation: as we increase the mobile ion concentration, the contribution of slow ion motion to the surface potential dynamics increases, thus lengthening the equilibration times (see Appendix C Note 4 for further discussion).[67] These results suggest that slower surface potential equilibration times measured at grain boundaries indeed result from higher local mobile ion concentrations.

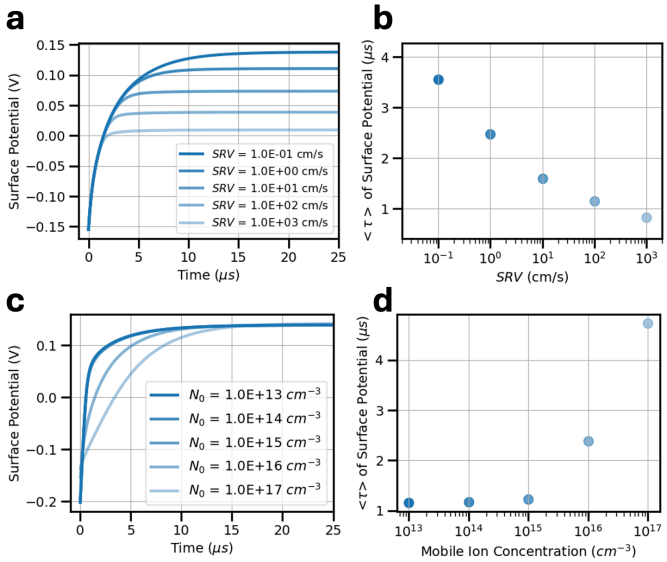

Fig. 3: Drift-diffusion simulations reveal influence of SRV and mobile ions on surface potential evolution. (a) Simulated surface potential evolutions plotted against time with varied SRV. (b) The average time constants describing the simulated surface potential equilibration times with respect to SRV, showing slower equilibration behavior at lower SRVs. (c) Simulated surface potential evolutions with varied mobile ion concentrations (N_0, cm^{-3}). (d) Average time constant that describes the equilibration of the simulated surface potential traces with respect to mobile ion concentration, showing slower equilibration behavior at higher mobile ion concentrations. For complete simulation parameter details see Appendix C Table 3.

To better understand the slower dynamics at grain boundaries, we explore the effect of different background illuminations intensities on the trEFM dynamics. Background illumination creates a population of mobile electronic carriers which can screen charged defects, such as halide vacancies or charge traps, masking their influence on observed dynamics. We thus expect background illumination bias should have two net effects: (1) the surface potential equilibration times should become faster due to overall higher electronic carrier concentrations reducing the marginal contribution from slower ionic processes, and (2) the observed contrast between grain boundaries and grain interiors should homogenize due to screening of both mobile ions and charge traps.

Figure 4 presents data consistent with both these expectations. We apply a continuous illumination bias to the ROI using an LED with a peak wavelength of 660 nm. While under this constant illumination bias, we use the 405 nm laser at 110 mW/cm^2 incident intensity to photoexcite the sample for trEFM imaging. We vary the illumination bias intensity from 0 mW/cm^2 to 100 mW/cm^2. Fig. 4a shows the representative topography of the ROI, with the characteristic nanoscale grains. Fig. 4b-e show the surface potential equilibration time maps measured by trEFM according to increasing illumination bias intensity (where Fig. 4f returns to 0 mW/cm^2). Consistent with our hypothesis, Fig. 4 shows that with increasing background illumination intensity, the average equilibration time becomes faster, consistent with our hypothesis above. Fig. 4g shows the surface potential equilibration times for grain boundaries and interiors plotted against illumination bias intensity. We see that with increasing illumination bias, the difference between grain boundaries and interiors decreases, again consistent with our hypothesis (see Appendix C Figs. 10-14 for detailed analysis and replicated results with 660 nm and 455 nm illumination biases). Overall,

these results are consistent with our earlier observations and drift-diffusion simulations in both overall equilibration times, and the intensities/photocarrier densities required to mask the grain boundary signals.

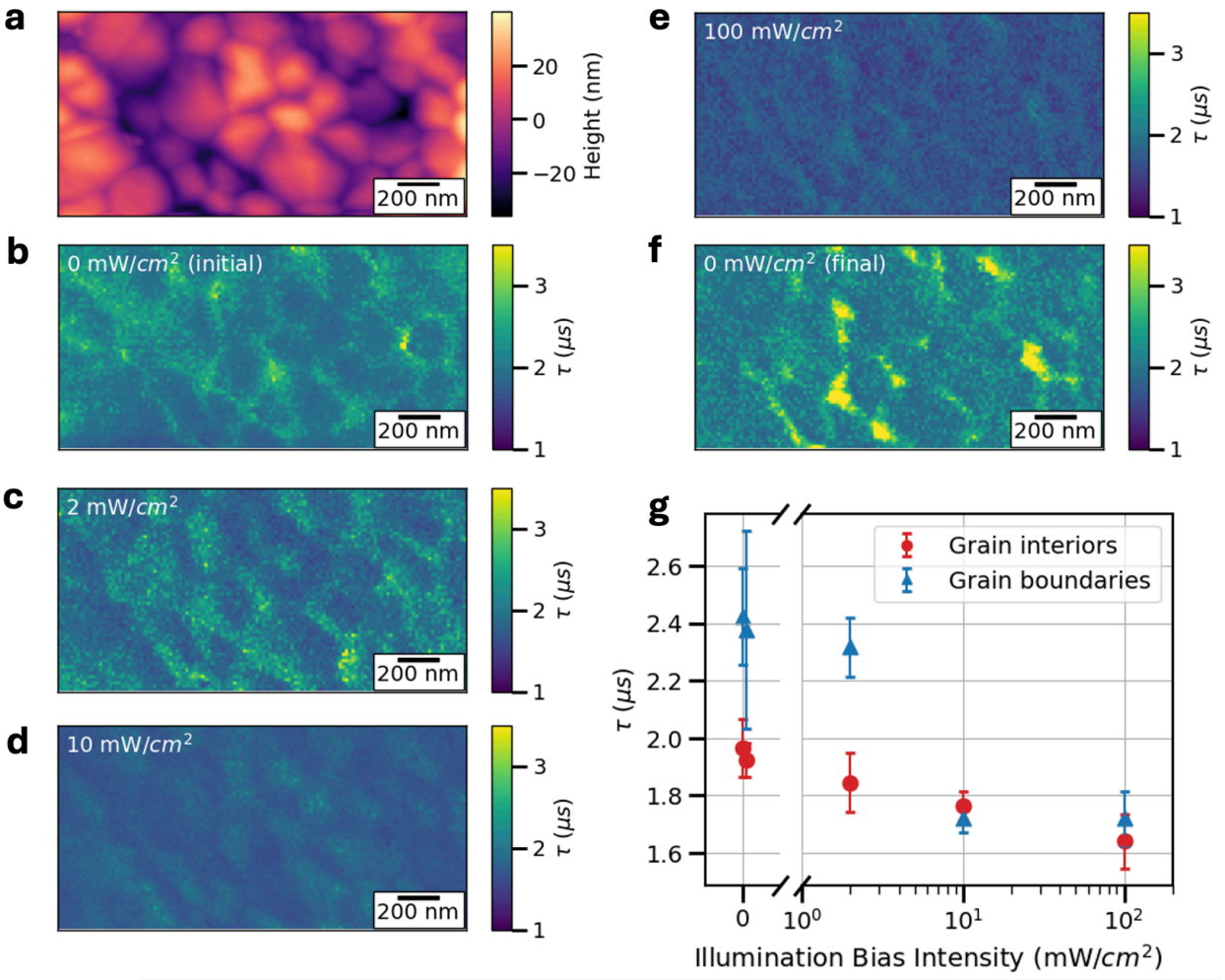

Fig. 4: Surface potential equilibration with varying background illumination bias intensity. (a) Topography of 2×1 μm ROI. (b)-(e) Images of surface potential equilibration time constants taken in the same ROI with increasing 660 nm bias illumination intensity ranging from 0 mW/cm^2 to 100 mW/cm^2, with a step-edge 405 nm laser at 110 mW/cm^2 used for trEFM excitation. (f) Reproduced trEFM time constant image at 0 mW/cm^2 showing return to unbiased time constants. (g) Average grain interior and boundary trEFM time constants with respect to background illumination bias intensity, error bars show standard deviation of masked pixel selection (Appendix C Fig. 10).

We stress test our model and interpretation with both intensity-dependent and wavelength-dependent trPL and trEFM measurements. Appendix C Figs. 15-19 and Table 4 show the detailed analysis of these experiments and simulations, which are broadly consistent with our interpretation. First, at higher excitation intensities we observe both faster trPL and faster trEFM signatures, consistent with higher order recombination processes and a correspondingly faster approach to equilibrium. Second, since we are exciting the half-stacks through the ITO with the cantilever at the perovskite surface, redder wavelength illumination photoexcites carriers closer to

the surface of the film, resulting in a greater contribution from SRV to the surface potential equilibration time.

Putting the experiment and simulation results together, Fig. 5a illustrates the key factors that influence the surface potential dynamics: the local mobile ion concentration and SRV. Fig. 5b shows simulated surface potential evolutions given parameters that approximate unpassivated and passivated grain boundaries and interiors. In the unpassivated regime, slightly higher mobile ion concentrations (grain boundaries) result in slightly slower equilibration times. In the passivated regime, upon the suppression of SRV and reduction in mobile ion concentration[18,19] the equilibration times become slower and indistinguishable. These results suggest that the heterogeneity we observe in surface potential equilibration times after passivation (Fig. 2f) is primarily due to local variations in SRV. This work highlights trEFM's ability to diagnose passivator uniformity and efficiency on the nanoscale.

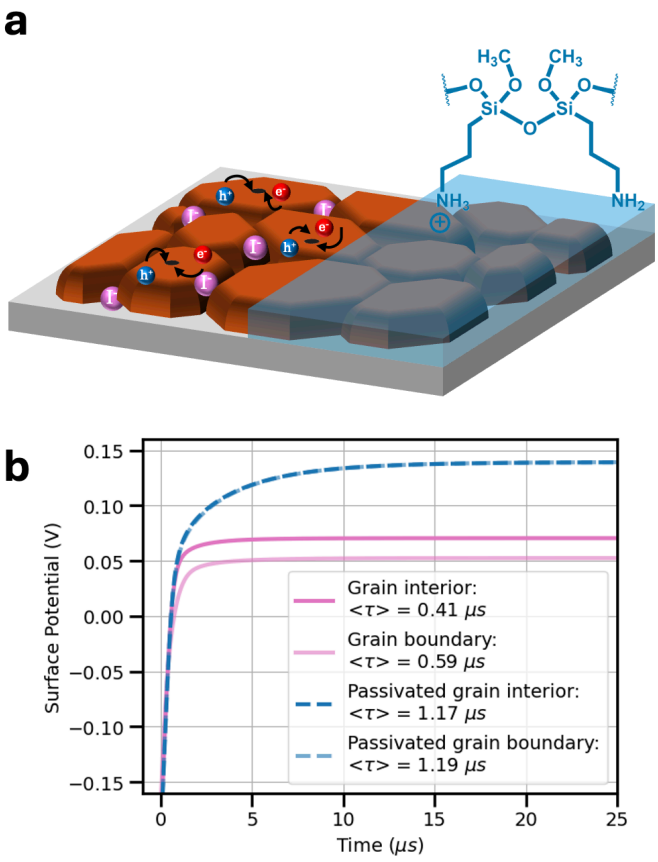

Fig. 5: Illustration of mobile ions and SRV, which influence surface potential evolution, supported by drift-diffusion simulations. (a) Illustration describing the effects of SRV and slow ion migration, which are both reduced by surface passivation with APTMS. (b) Drift-diffusion simulations of the surface potential where the primary difference between the grain interior and grain boundary is the concentration of mobile ions (1×10^{15} cm^{-3} and 5×10^{15} cm^{-3} respectively) with a SRV of 100 cm/s; simulated surface potential evolution of passivated grain interiors and boundaries have both reduced mobile ion concentrations and suppressed SRV values (5×10^{14} cm^{-3} and 1×10^{15} cm^{-3} for grain interiors and boundaries respectively, with a SRV of 0.1 cm/s). Note that there are two blue, dashed traces representing the passivated condition that are indistinguishable. For complete simulation parameters see Appendix C Table 3.

4.4 Conclusion and Outlook

We demonstrate that in halide perovskites, trEFM probes local surface potential equilibration time, which is influenced by both electronic carrier recombination and mobile ions. We show that passivation results in slower equilibration times due to strong suppression of SRV, and we directly correlate these equilibration dynamics to SRV obtained from trPL. Importantly, we reveal local variations in SRV after surface passivation using trEFM, demonstrating the need to optimize passivation treatments. Additionally, we conclude that slower equilibration times observed at grain boundaries in unpassivated samples are caused by higher defect concentrations that result in increased contributions of slow ion motion to the surface potential dynamics. These advances highlight the ability to characterize not only the impact of perovskite nanostructure on local carrier dynamics, but also to evaluate the effectiveness of passivation below the optical diffraction limit at length scales relevant to modern halide perovskites. We anticipate the use of sub-diffraction-limited imaging of carrier recombination dynamics to optimize perovskite semiconductor devices and passivation treatments down to the nanoscale.

4.5 Methods

Materials

Lead iodide (99.99%, for perovskite precursor) and Me-4PACz (>99.0%) were purchased from TCI. Lead bromide (99.999%, ultra dry) and cesium iodide (99.999%) were purchased from Alpha Aesar. Formamidinium iodide (>99.99%), phenethylammonium iodide, and methylammonium chloride (>99.99%) were purchased from Greatcell Solar Materials. Aluminum oxide nanoparticles dissolved at 20 wt% was purchased from Sigma Alrich. All other materials were purchased from Sigma Aldrich.

Sample preparation

All preparation of perovskite samples was performed in a N_2 glovebox.

A 1.2 M $Cs_{0.17}FA_{0.83}Pb(I_{0.75}Br_{0.25})_3$ solution was prepared according to previous literature reports[61] by mixing the correct molar ratio of PbI_2, $PbBr_2$, FAI, and CsI in a 4:1 solvent ratio of N,N-Dimethylformamide (DMF) and Dimethyl sulfoxide (DMSO). 1.5 cm^2 indium tin oxide (ITO) coated glass substrates were cleaned by sequential sonication in DI water containing ~2% Micro-90 detergent, DI water, acetone, and isopropanol for 10 minutes each. The substrates were ozone-cleaned for 23 minutes prior to spincoating. Me-4PACz was dissolved in DMF at a concentration of 50 mg/mL and subsequently diluted to 1 mg/mL in isopropanol. Approximately 60 µL of the 1 mg/mL Me-4PACz solution was deposited on the substrate and spincoated at 5000 rpm for 30 s with an acceleration of 800 rpm/s. The film was annealed at 100°C for 10 minutes. Next, 100 µL of a solution with the ratio 1:150 Al_2O_3 nanoparticle to isopropanol was spincoated at 6000 rpm for 30 s with an acceleration of 800 rpm/s to wash off excess Me-4PACz and improve wettability. The substrates were annealed at 100°C for 30 s. Finally, 70 µL of the perovskite precursor solution were deposited on the substrate and spincoated at 1000 rpm for 10 s with an acceleration of 200 rpm/s followed by spinning at 5000 rpm for 35 s with an acceleration of 800 rpm/s; 10 s before

the completion of the final spincoating step, 300 µL of anisole was dynamically deposited on the sample. The sample was annealed at 100°C for 45 minutes.

A 1.2 M $Cs_{0.22}FA_{0.78}Pb(I_{0.85}Br_{0.15})_3$ solution was prepared by mixing the correct molar ratio of PbI_2, $PbBr_2$, FAI, CsI and a 15 mol% relative to the Pb content equivalent of MACl to improve crystallization in a 4:1 solvent ratio of N,N-Dimethylformamide (DMF) and Dimethyl sulfoxide (DMSO). Indium tin oxide (ITO) coated glass substrates 1.5 cm^2 in size were cleaned by sequential sonication in DI water containing ~2% Micro-90 detergent, DI water, acetone, and isopropanol for 10 minutes each. The substrates were ozone-cleaned for 23 minutes prior to spincoating. Me-4PACz was first dissolved in DMF at a concentration of 50 mg/mL and was subsequently diluted to 1 mg/mL in 2-propanol (IPA). Approximately 60 µL of the 1 mg/mL Me-4PACz solution was spincoated on the substrates at 5000 rpms for 30 s with an acceleration of 800 rpm/s and annealed at 100 °C for 10 min. Next, 100 µL of IPA was dynamically spincoated on the substrate to wash away excess Me-4PACz at 6000 rpm for 30 s with an acceleration of 800 rpm/s and annealed at 100 °C for 5 min. Following that, Al_2O_3 nanoparticles suspended in IPA was diluted further with IPA by 1:150. Approximately 50 µL of the Al_2O_3 solution was spincoated at 6000 rpm for 30 s and annealed at 100 °C for 50 s to improve the wettability of perovskite on the Me-4PACz layer. The perovskite solution was filtered through a 0.2 µm PTFE membrane filter. Approximately 60 µL of the perovskite solution was dynamically deposited on top of the substrate and spincoated at 1000 rpm for 10 s with an acceleration of 200 rpm/s followed by spinning at 5000 rpm for 35 s with an acceleration of 800 rpm/s. After 25-30 s of the second step, 330 µL of an anisole antisolvent was dynamically deposited on the spinning substrate. The half-stack was then annealed for 30 min at 100 °C on a hot plate.

Passivation

APTMS and AEAPTMS passivation of the perovskite half-stacks was performed at room temperature and ambient conditions in a vacuum oven for 4 mins. A volume of 500 µL of the silane was placed in a 4 mL vial with the perovskite sample placed face up near the vial. The vial and sample were covered with a 500 mL glass jar inside of the vacuum chamber, and the pressure was pumped down to -26 inHg relative to the atmospheric pressure, as described in previous work.[16]

PEAI passivation was performed in a nitrogen glovebox by first preparing a 0.030 M solution of PEAI in IPA. Next, 100 µL of the PEAI solution was dynamically spincoated on the perovskite surface at 3000 rpm for 30 s with an acceleration of 800 rpm/s. Following treatment with PEAI, the sample was left to rest in the nitrogen glovebox in the dark for ~24 hours prior to making measurements.[58]

UV-Vis characterization

UV-Vis absorption spectra of the perovskite control and passivated half-stacks were collected using an Agilent 8453 UV-Vis Spectrometer in a wavelength range of 200-1100 nm and an integration time of 0.5 s.

XRD characterization

X-ray diffraction measurements of the perovskite control and passivated half-stacks were measured using a Bruker D8 Discover with a Pilatus 100 K large-area 2D detector with Cu Kα radiation at 50,000 mW.

Photoluminescence characterization

trPL was measured using a PicoQuant Fluotime 100 spectrometer and Picoharp 300 TCSPC system equipped with a 640 nm pulsed diode laser with a high average power of 30 mW and 90 ps pulse width. The repetition rate of the pulsed laser was controlled with an external function generator. The laser was pulsed with an excitation intensity of ~ 30 nJ/cm^2, in order to capture the decay at a carrier density near that of one Sun power. The PL emission was passed through a 700 nm long-pass filter before reaching the detector. The PL data was fitted using a stretched exponential function, additional information of this fitting can be found in the Supporting Information. For this measurement, the samples were measured in ambient conditions immediately after removal from a nitrogen glovebox.

Steady-state PL spectra and PLQY values were collected using an integrating sphere spectrometer (Hamamatsu Photonics K.K.) and a 532 nm continuous wave laser (CrystalLaser Lc). The integration time of the spectrometer was set to 250 ms and 5 measurements were averaged for each spectrum. The laser fluences was measured with a Thorlabs beam profiler (BP209-VIS). A continuous neutral density filter wheel (Thorlabs) was used to control the laser fluence. The neutral density filter wheel was adjusted for all measurements to be made at 100 mW/cm^2.

Confocal photoluminescence characterization

Confocal PL imaging was performed using a custom scanning confocal microscope built with a Nikon TE-2000 inverted microscope fitted with 60x dry objective (Nikon Plan Fluor, NA=0.7). A 640 nm pulsed diode laser (PDL 800-D P-C-640B, FWHM = 90 ps) was used at a repetition rate of 250 kHz, with a resulting fluence of 105 nJ/cm^2. The laser was coupled to the microscope via a FC/APC single-mode fiber and directed into the objective via a 640 dichroic cube. Sample was encapsulated under nitrogen and excited face-on (not through the substrate). The emission was filtered through a 700-850 nm bandpass filter (700 LP and 850 SP) and focused on a Single Photon Avalanche Diode from Micro Photon Devices. The PL decay was collected using a PicoHarp 300 time-correlated single photon counting (TCSPC) module. The scanning is done using a piezo nano position stage (PI). The data collection and analysis are performed through custom Python-based software.

trEFM characterization

trEFM and the required experimental setup have been discussed in detail.[51,52] Measurements were performed on an Asylum Research MFP3D-BIO mounted on a Nikon inverted optical microscope. All measurements used Pt-coated cantilevers (mikroMasch HQ/NSC15/Pt) driven at resonance frequency (~300 kHz). The sample was mounted in an inert glovebox environment in a sealed cell, then imaged under active flowing nitrogen in this sealed cell. The cantilever oscillation was recorded using a 16-bit A/D digitizer (Dynamic Signals/GaGe Razor Express CSE1622), typically at 5 MS/s, and synced to the cantilever oscillation phase (180°) using custom trigger electronics

(detailed circuit information can be found in our previous reports; additional information available upon request).[51,52] In an experimental window of 16 ms, we apply a bias of +10 V to the cantilever at t = 1 ms, the sample is then allowed to equilibrate for 4 ms; the cantilever oscillation is digitized starting at t = 4.6 ms through t = 8.6 ms, and laser excitation is triggered at t = 5 ms and turned off at t = 7 ms. We used either a 405 nm (Omicron PhoxXplus 405-120) or a 705 nm (Omicron PhoxXplus 705-40) continuous wavelength laser at an incident intensity of ~110-150 mW/cm^2 to excite our samples; we adjust the intensity using neutral density filters and the electrical power via software control. The laser was focused via a bottom objective on an inverted optical microscope and co-aligned with the cantilever tip. The illumination intensity was measured using the combination of a calibrated photodiode and a Pixera CCD camera (150CL-CU). Raw cantilever deflection data were used to extract the instantaneous frequency by demodulating the time-dependent cantilever amplitude using a short-time Fourier transform (STFT) and then using a parabolic estimation of the peak frequency (ridge finding) per time segment. This code is freely available online via the FFTA Python package (https://github.com/GingerLabUW/FFTA). See Appendix C Information Note 1 for a complete description of the required cantilever calibration step. Alternatively, we can use a convolutional neural network (CNN) to fit the cantilever instantaneous frequency signal (obtained via the Hilbert Transform) to obtain cantilever-independent time constants to describe the surface potential equilibration.[60] Appendix C Information Figs. 20-22 show recreations of Figs. 1, 2, and 4 in the main text using the CNN, which show the same trends we present using the calibration method.

4.6 Acknowledgements

Author Contributions

M.D.B. and J.P. contributed equally to this work. M.D.B. and J.P. wrote the paper and prepared the figures. M.D.B., J.P., R.G., and D.S.G. conceptualized the work. M.D.B. and J.P. drafted and edited the manuscript, with input and revisions from R.G. and D.S.G. Finally, M.D.B. and J.P. performed all the experiments.

Acknowledgements

The atomic force microscopy imaging work (M.D.B., J.P., R.G.) was supported by the U.S. Department of Energy, Office of Basic Energy Sciences, Division of Materials Sciences and Engineering under Award DE-SC0013957. Part of this work was carried out at the Molecular Analysis Facility, a National Nanotechnology Coordinated Infrastructure site at the University of Washington, which is supported by the National Science Foundation (NNCI-1542101), the Molecular Engineering and Sciences Institute, and the Clean Energy Institute. M.D.B. acknowledges support from the NSF Graduate Student Fellowship program under Grant no. DGE-2140004. M.D.B. thanks Nir Tessler for advice on drift-diffusion simulations. J.P. thanks Zixu Huang for help with XRD measurements. D.S.G acknowledges salary and infrastructure support from the Washington Research Foundation, the Alvin L. and Verla R. Kwiram endowment, and the B. Seymour Rabinovitch Endowment.

4.7 References

1. Zhang, H., Pfeifer, L., Zakeeruddin, S. M., Chu, J. & Grätzel, M. Tailoring passivators for highly efficient and stable perovskite solar cells. *Nat. Rev. Chem.* **7**, 632–652 (2023).

2. Stranks, S. D. & Snaith, H. J. Metal-halide perovskites for photovoltaic and light-emitting devices. *Nat. Nanotech.* **10**, 391–402 (2015).

3. Li, M. *et al.* Acceleration of radiative recombination for efficient perovskite LEDs. *Nature* **630**, 631–635 (2024).

4. Wei, H. & Huang, J. Halide lead perovskites for ionizing radiation detection. *Nat. Commun.* **10**, 1066 (2019).

5. Nguyen, H. A. *et al.* Design Rules for Obtaining Narrow Luminescence from Semiconductors Made in Solution. *Chem. Rev.* **123**, 7890–7952 (2023).

6. Eperon, G. E., Horantner, M. T. & Snaith, H. J. Metal halide perovskite tandem and multiple-junction photovoltaics. *Nat. Rev.* **1**, 0095 (2017).

7. Dequilettes, D. W. *et al.* Photoluminescence Lifetimes Exceeding 8 μs and Quantum Yields Exceeding 30% in Hybrid Perovskite Thin Films by Ligand Passivation. *ACS Energy Lett.* **1**, 438–444 (2016).

8. DeQuilettes, D. W. *et al.* Impact of microstructure on local carrier lifetime in perovskite solar cells. *Science (1979)* **348**, 683–686 (2015).

9. Jariwala, S. *et al.* Local Crystal Misorientation Influences Non-radiative Recombination in Halide Perovskites. *Joule* **3**, 3048–3060 (2019).

10. Kim, G.-W. & Petrozza, A. Defect Tolerance and Intolerance in Metal-Halide Perovskites 2. Defects in Perovskite Solar Cells: Efficiency versus Stability. *Adv. Energy Mater.* **10**, 2001959 (2020).

11. De Keersmaecker, M., Tirado, J., Armstrong, N. R. & Ratcliff, E. L. Defect Quantification in Metal Halide Perovskites Anticipates Photoluminescence and Photovoltaic Performance. *ACS Energy Lett* **9**, 243–252 (2024).

12. Dequilettes, D. W. *et al.* Reduced recombination via tunable surface fields in perovskite thin films. *Nat Energy* **9**, 457–466 (2024).

13. Wang, J. *et al.* Reducing Surface Recombination Velocities at the Electrical Contacts Will Improve Perovskite Photovoltaics. *ACS Energy Lett.* **14**, 222–227 (2019).

14. Lin, Y. H. *et al.* Bandgap-universal passivation enables stable perovskite solar cells with low photovoltage loss. *Science (1979)* **384**, 767–775 (2024).

15. Shi, Y. *et al.* (3-Aminopropyl)trimethoxysilane Surface Passivation Improves Perovskite Solar Cell Performance by Reducing Surface Recombination Velocity. *ACS Energy Lett.* **7**, 4081–4088 (2024).

16. Jariwala, S. *et al.* Reducing surface recombination velocity of methylammonium-free mixed-cation mixed-halide perovskites via surface passivation. *Chem. Mater.* **33**, 5035–5044 (2021).

17. Rigter, S. A. *et al.* Passivation Properties and Formation Mechanism of Amorphous Halide Perovskite Thin Films. *Adv. Func. Mater.* **31**, 2010330 (2021).

18. Akrami, F., Jiang, F., Giridharagopal, R. & Ginger, D. S. Kinetic Suppression of Photoinduced Halide Migration in Wide Bandgap Perovskites via Surface Passivation. *J. Phys. Chem. Lett* **14**, 9310–9315 (2023).

19. Pothoof, J., Westbrook, R. J. E., Giridharagopal, R., Breshears, M. D. & Ginger, D. S. Surface Passivation Suppresses Local Ion Motion in Halide Perovskites. *J. Phys. Chem. Lett* **14**, 6092–6098 (2023).

20. Jiang, F. *et al.* Scanning Kelvin Probe Microscopy Reveals That Ion Motion Varies with Dimensionality in 2D Halide Perovskites. *ACS Energy Lett.* **6**, 100–108 (2021).

21. McGovern, L. *et al.* Reduced Barrier for Ion Migration in Mixed-Halide Perovskites. *ACS Appl Energy Mater* **4**, 13431–13437 (2021).

22. Liu, Y. *et al.* Direct Observation of Photoinduced Ion Migration in Lead Halide Perovskites. *Adv. Funct. Mater.* **31**, 2008777 (2020).

23. Jiang, F. *et al.* Improved reverse bias stability in p-i-n perovskite solar cells with optimized hole transport materials and less reactive electrodes. *Nat. Energy* **9**, 1275–1284 (2024).

24. Weber, S. A. L. *et al.* How the formation of interfacial charge causes hysteresis in perovskite solar cells. *Energy Environ. Sci.* **11**, 2404–2413 (2018).

25. Liu, J. *et al.* Correlations between Electrochemical Ion Migration and Anomalous Device Behaviors in Perovskite Solar Cells. *ACS Energy Lett.* **6**, 1003–1014 (2021).

26. Tennyson, E. M. *et al.* The Effects of Incident Photon Energy on the Time-Dependent Voltage Response of Lead Halide Perovskites. *Chem. Mater.* **31**, 8969–8976 (2019).

27. Jones, T. W. *et al.* Lattice strain causes non-radiative losses in halide perovskites. *Energy Environ Sci* **12**, 596–606 (2019).

28. Tennyson, E. M., S Doherty, T. A. & Stranks, S. D. Heterogeneity at multiple length scales in halide perovskite semiconductors. *Nat. Rev.* **4**, 573–587 (2019).

29. Frohna, K. *et al.* The impact of interfacial quality and nanoscale performance disorder on the stability of alloyed perovskite solar cells. *Nat Energy* (2024) doi:10.1038/s41560-024-01660-1.

30. Delport, G., Macpherson, S. & Stranks, S. D. Imaging Carrier Transport Properties in Halide Perovskites using Time-Resolved Optical Microscopy. *Adv. Energy Mater.* **10**, 1903814 (2020).

31. Giridharagopal, R., Cox, P. A. & Ginger, D. S. Functional Scanning Probe Imaging of Nanostructured Solar Energy Materials. *Acc. Chem. Res.* **49**, 1769–1776 (2016).

32. Giridharagopal, R. *et al.* Time-Resolved Electrical Scanning Probe Microscopy of Layered Perovskites Reveals Spatial Variations in Photoinduced Ionic and Electronic Carrier Motion. *ACS Nano* **13**, 2812–2821 (2019).

33. Garrett, J. L. *et al.* Real-Time Nanoscale Open-Circuit Voltage Dynamics of Perovskite Solar Cells. *Nano Lett.* **17**, 2554–2560 (2017).

34. Guthrey, H. & Moseley, J. A Review and Perspective on Cathodoluminescence Analysis of Halide Perovskites. *Adv. Energy Mater.* **10**, 1903840 (2020).

35. Zhou, Y., Herz, L. M., Jen, A. K.-Y. & Saliba, M. Advances and challenges in understanding the microscopic structure–property–performance relationship in perovskite solar cells. *Nat. Energy* **7**, 794–807 (2022).

36. Tennyson, E. M. *et al.* Correlated Electrical and Chemical Nanoscale Properties in Potassium-Passivated, Triple-Cation Perovskite Solar Cells. *Adv. Mater. Interaces* **7**, 2000515 (2020).

37. Collins, S. D. *et al.* Observing Ion Motion in Conjugated Polyelectrolytes with Kelvin Probe Force Microscopy. *Adv Electron Mater* **3**, 1700005 (2017).

38. Taddei, M. *et al.* Interpreting Halide Perovskite Semiconductor Photoluminescence Kinetics. *ACS Energy Lett.* **9**, 2508–2516 (2024).

39. Yuan, Y. *et al.* Shallow defects and variable photoluminescence decay times up to 280 μs in triple-cation perovskites. *Nat Mater* **23**, 391–397 (2024).

40. Xiong, S. *et al.* Reducing nonradiative recombination for highly efficient inverted perovskite solar cells via a synergistic bimolecular interface. *Nat. Commun.* **15**, 5607 (2024).

41. Zhao, K. *et al.* peri-Fused polyaromatic molecular contacts for perovskite solar cells. *Nature* **632**, 301–306 (2024).

42. Rehman, W. *et al.* Photovoltaic mixed-cation lead mixed-halide perovskites: links between crystallinity, photo-stability and electronic properties. *Energy Environ. Sci* **10**, 361–369 (2017).

43. Bischak, C. G., Sanehira, E. M., Precht, J. T., Luther, J. M. & Ginsberg, N. S. Heterogeneous Charge Carrier Dynamics in Organic−Inorganic Hybrid Materials: Nanoscale Lateral and Depth-Dependent Variation of Recombination Rates in Methylammonium Lead Halide Perovskite Thin Films. *ACS Nano Lett.* **15**, 4799–4807 (2015).

44. Dwyer, R. P., Harrell, L. E. & Marohn, J. A. Lagrangian and Impedance-Spectroscopy Treatments of Electric Force Microscopy. *Phys. Rev. Appl.* **11**, 64020–64052 (2019).

45. Tirmzi, A. M., Dwyer, R. P., Jiang, F. & Marohn, J. A. Light-Dependent Impedance Spectra and Transient Photoconductivity in a Ruddlesden-Popper 2D Lead-Halide Perovskite Revealed by Electrical Scanned Probe Microscopy and Accompanying Theory. *J. Phys. Chem. C* **124**, 13639–13648 (2020).

46. Albrecht, T. R., Grütter, P., Horne, D. & Rugar, D. Frequency modulation detection using high-Q cantilevers for enhanced force microscope sensitivity. *J. Appl. Phys.* **69**, 668–673 (1991).

47. Miyahara, Y., Cockins, L. & Grütter, P. Electrostatic Force Microscopy Characterization of Low Dimensional Systems. in *Kelvin Probe Force Microscopy* (eds. Sadewasser, A. & Glatzel, T.) vol. 48 177–199 (Springer, Berlin, Heidelberg).

48. Collins, L. *et al.* Breaking the Time Barrier in Kelvin Probe Force Microscopy: Fast Free Force Reconstruction Using the G-Mode Platform. *ACS Nano* **11**, 8717–8729 (2017).

49. Checa, M. *et al.* High-speed mapping of surface charge dynamics using sparse scanning Kelvin probe force microscopy. *Nat. Commun.* **14**, 7196 (2023).

50. Coffey, D. C. & Ginger, D. S. Time-resolved electrostatic force microscopy of polymer solar cells. *Nat. Mater.* **5**, 735–740 (2006).

51. Karatay, D. U., Harrison, J. S., Glaz, M. S., Giridharagopal, R. & Ginger, D. S. Fast time-resolved electrostatic force microscopy: Achieving sub-cycle time resolution. *Rev. Sci. Instrum.* **87**, 053702 (2016).

52. Giridharagopal, R. *et al.* Submicrosecond time resolution atomic force microscopy for probing nanoscale dynamics. *Nano Lett.* **12**, 893–898 (2012).

53. Cox, P. A. *et al.* Imaging Charge Transfer State Excitations in Polymer/Fullerene Solar Cells with Time-Resolved Electrostatic Force Microscopy. *J. Phys. Chem. Lett.* **6**, 2852–2858 (2015).

54. Reid, O. G., Rayermann, G. E., Coffey, D. C. & Ginger, D. S. Imaging Local Trap Formation in Conjugated Polymer Solar Cells: A Comparison of Time-Resolved Electrostatic Force Microscopy and Scanning Kelvin Probe Imagin. *J. Phys. Chem. C.* **114**, 20672–20677 (2010).

55. Shao, G., Rayermann, G. E., Smith, E. M. & Ginger, D. S. Morphology-Dependent Trap Formation in Bulk Heterojunction Photodiodes. *J. Phys. Chem. B* **117**, 4654–4660 (2013).

56. Breshears, M. D., Giridharagopal, R., Pothoof, J. & Ginger, D. S. A Robust Neural Network for Extracting Dynamics from Electrostatic Force Microscopy Data. *J. Chem. Inf. Model.* **62**, 4342–4350 (2022).

57. Teale, S., Degani, M., Chen, B., Sargent, E. H. & Grancini, G. Molecular cation and low-dimensional perovskite surface passivation in perovskite solar cells. *Nat. Energy* **9**, 779–792 (2024).

58. Jiang, Q. *et al.* Surface passivation of perovskite film for efficient solar cells. *Nat. Photonics* **13**, 460–466 (2019).

59. Thornton, S. T. & Marion, J. B. Classical Dynamics of Particles and Systems. in *Classical Dynamics of Particles and Systems* 100–117 (Thomsom Brooks/Cole, 2004).

60. Breshears, M. D., Giridharagopal, R. & Ginger, D. S. Multi-Output Convolutional Neural Network for Improved Parameter Extraction in Time-Resolved Electrostatic Force Microscopy Data. *Preprint* (2025), arXiv:2502.03572.

61. Taddei, M. *et al.* Ethylenediamine Addition Improves Performance and Suppresses Phase Instabilities in Mixed-Halide Perovskites. *ACS Energy Lett.* **7**, 4265–4273 (2022).

62. Xu, J. *et al.* Triple-halide wide–band gap perovskites with suppressed phase segregation for efficient tandems. *Science (1979)* **367**, 1097–1104 (2020).

63. Wang, R. *et al.* Constructive molecular configurations for surface-defect passivation of perovskite photovoltaics. *Science (1979)* **366**, 1509–1513 (2019).

64. Johnston, M. B. & Herz, L. M. Hybrid Perovskites for Photovoltaics: Charge-Carrier Recombination, Diffusion, and Radiative Efficiencies. *Acc. Chem. Res.* **49**, 146–154 (2016).

65. Courtier, N. E., Richardson, G. & Foster, J. M. A fast and robust numerical scheme for solving models of charge carrier transport and ion vacancy motion in perovskite solar cells. *Appl. Math. Model.* **63**, 329–348 (2018).

66. Courtier, N. E., Cave, J. M., Foster, J. M., Walker, A. B. & Richardson, G. How transport layer properties affect perovskite solar cell performance: insights from a coupled charge transport/ion migration model. *Energy Environ. Sci* **12**, 396–409 (2019).

67. Courtier, N. E., Cave, · J M, Walker, · A B, Richardson, · G & Foster, · J M. IonMonger: a free and fast planar perovskite solar cell simulator with coupled ion vacancy and charge carrier dynamics. *J Comput Electron* **18**, 1435–1449 (2019).

68. Peng, W. *et al.* Quantification of Ionic Diffusion in Lead Halide Perovskite Single Crystals. *ACS Energy Lett.* **3**, 1477–1481 (2018).

69. Futscher, M. H. *et al.* Quantification of ion migration in CH3NH3PbI 3 perovskite solar cells by transient capacitance measurements. *Mater. Horiz.* **6**, 1497–1503 (2019).

70. Yun, J. S. *et al.* Critical Role of Grain Boundaries for Ion Migration in Formamidinium and Methylammonium Lead Halide Perovskite Solar Cells. *Adv. Energy Mater.* **6**, 1600330 (2016).

71. Siekmann, J., Ravishankar, S. & Kirchartz, T. Apparent Defect Densities in Halide Perovskite Thin Films and Single Crystals. *ACS Energy Lett.* **6**, 3244–3251 (2021).

72. Eames, C. *et al.* Ionic transport in hybrid lead iodide perovskite solar cells. *Nat. Commun.* **6**, 7497 (2015).

73. Wu, N., Walter, D., Fell, A., Wu, Y. & Weber, K. The Impact of Mobile Ions on the Steady-State Performance of Perovskite Solar Cells. *J. Phys. Chem. C* **124**, 219–229 (2020).

74. Mcgovern, L. *et al.* Reduced Barrier for Ion Migration in Mixed-Halide Perovskites. *Appl. Energy Mater.* **4**, 13431–13437 (2021).

Chapter 5: Opportunities and Outlook

5.1 Proposal: Correlated trEFM and EBSD to Explore How Local Strain Gradients Affect Surface Potential Equilibration Time

Electron backscattering diffraction (EBSD) is a method that, at very high spatial resolutions, resolves crystallographic information that enables evaluation of strain gradients in polycrystalline films.[1–3] We have previously used EBSD to characterize large-grain methylammonium lead triiodide ($MAPbI_3$), finding that larger grains exhibited larger strain gradients, and in turn corresponded to decreased photoluminescence (PL) brightness.[1] Indeed, Adhyaksa et al. also used EBSD to understand structural heterogeneity and the impact on PL for $MAPbI_3$.[2] $MAPbI_2$ was advantageous for not only its large morphological features, but also its relatively stability under the e-beam required for EBSD[1,2] Recent mixed-cation, mixed-halide perovskite compositions have proven more robust to e-beam damage,[4] and understanding how strain gradients may be affected by additives, composition engineering, and post-treatment passivation strategies is of great importance for not only improving lab-scale device performances but also scaling up devices for manufacturing.

The benefit of large-grain perovskite thin films is the ability to characterize them with optical microscopy. Time-resolved photoluminescence (trPL) and confocal PL brightness maps are optoelectronic properties that tell us about the quality of the film and relate to the quality of the resulting photovoltaic device. While trEFM can resolve nanoscale variations in surface potential dynamics (affected by surface recombination velocity and ion motion, among other factors),[5] additional correlation with traditional optical microscopy methods would strengthen our understanding of the structure-function relationship.

Recent work from the David Fenning's group at University of California, San Diego used a combination of additive engineering and alternate processing conditions to synthesize large-grain formamidinium lead triiodide ($FAPbI_3$) which exhibited improved stability and performance for photovoltaic devices.[6,7] I propose, in collaboration with the Fenning group, an investigation of the impact of strain gradients on surface potential evolution dynamics and trPL. I expect that regions with increased strain gradients (regions with increased compressive strain, in particular[8]) will exhibit dimmer PL and faster PL lifetimes; this is broadly in line with what Jariwala et al. found[1] and what deQuilettes et al. found.[9] Additionally, I expect that regions with increased strain gradients (like morphological domain or "grain" boundaries) will have faster surface recombination velocity due to more defects in the crystal lattice at the surface; as such, we would expect that the surface potential equilibration dynamics measured by trEFM would be faster in

these regions. However, we have previously observed that even at grain boundaries, where we may expect faster surface recombination velocities and thus faster surface potential equilibration, we observe slower trEFM dynamics. We attribute this to an increased contribution from slow ion motion through defect sites. Obtaining additional structural information would provide insight into the threshold of strain-induced defects that enable ion motion. Further investigation with varied additives that the Fenning group have explored[6,7] may shed light on whether additive chemistry affects local strain gradients and the resulting performance metrics of interest.

Practically, I would propose performing trEFM first, as it is completely non-destructive. Importantly, I propose measuring at least two small regions of interest with two excitation wavelengths at low intensity (ideally ~100 mW/cm^2, depending on the wavelength, to mimic the same generated carrier concentration as 1 Sun illumination). General good practice with trEFM would also involve checking two additional excitation intensities to ensure that with increased intensity we observe faster surface potential equilibration dynamics.[5,10,11] After noting the critical features in the regions of interest, scratching a box with the SPM probe would then enable further characterization on other microscopes. Instead of encapsulating the film (which is typical for optical microscopy experiments) I would low the sample into a nitrogen flow cell and collect PL brightness and trPL images in the regions of interest. Finally, I would conclude the correlation study with EBSD, as EBSD is most likely to damage the film.

Given this rich dataset, there is ample opportunity to precisely correlate the images and use statistical analysis to understand correlations in the data. (For example, I would expect higher degrees of strain captured by EBSD would strongly, positively correlate to dimmer PL brightness and slower trEFM surface potential dynamics, per my previous hypothesis.) Ultimately, this study would inform the structure-function relationship in $FAPbI_3$.

5.2 Proposal: Exploring Surface Potential Equilibration in New Organic Photovoltaics through trEFM and Drift-Diffusion Modeling

Organic photovoltaics (OPVs) are of great interest for transparent solar cells[12–16] and sensors.[15,17] As they are only electronic conductors (as opposed to also conducting ions like lead halide perovskites), the underlying dynamics that govern the surface potential equilibration are slightly more straightforward. We have previously studied OPV materials with trEFM, finding that they exhibited heterogeneity on the nanoscale dependent on blend ratio.[12–14,16] To reconcile these results, which indicate trEFM captures external quantum efficiency (EQE), with the results from our work on highly efficient mixed-cation, mixed-halide perovskites, which indicate trEFM also captures "something" correlated to PL lifetimes, we used drift diffusion simulations. As shown in Chapter 4, we can use drift-diffusion simulations to understand how surface recombination velocity and mobile ions affect surface potential equilibration. These results unify our observations on mixed-cation, mixed-halide perovskite thin films. These perovskite compositions, however, have much higher EQEs compared to OPVs.[18–20] As such, to ensure our interpretation of our results on perovskite thin films was correct, we simulated an OPV using IonMonger.[21–23] To do so, we used the parameters shown in Table 5.1.

Table 5.1

Parameter	Value
Thickness (d)	100 nm
Bandgap (E_g)	1.9 eV
Shockley-Read Hall Recombination Lifetime (τ_{SRH})	1e20 s (effectively no SRH recombination)
Surface Recombination Velocity (SRV)	0 cm/s
Mobile Ion Density (N_0)	0 cm^{-3}
Absorption Coefficient (ϵ)	2 ϵ_0 F/m
Electronic Carrier Diffusion Coefficient (D_n)	1e-5 cm/s

By using this parameter combination, we can approximate an OPV with IonMonger. A primary observation from our previous work on OPVs was that trEFM dynamics (surface potential evolution upon excitation) slowed down linearly with increasing open-circuit voltage (related to the log of the excitation intensity). This relationship suggested that trEFM captured the external quantum efficiency or "charging" efficiency of the OPV.

To mimic these conditions, I varied the excitation intensity in my drift-diffusion simulations. I simulated surface potential illumination under photoexcitation with intensities ranging from 0.05 mW/cm^2 to 1 mW/cm^2. When approximating the experimental setup we used to test mixed-cation, mixed-halide perovskites, I used an excitation intensity of 100 mW/cm^2 (which generated electronic carriers at the equivalent of ~1 Sun illumination). Because OPVs exhibit a significantly decreased EQE compared to perovskite semiconductors, I used much lower excitation intensities when simulating my OPV. Figure 5.1 shows the results of these simulations; 5.1a plots the $<\tau>$ of the surface potential equilibration against the excitation intensity, and 5.1b shows the surface potential equilibration *rate* ($1/<\tau>$) plotted against the excitation intensity. Figure 5.1c shows the surface potential equilibration traces, which clearly show that with increasing excitation intensity we observe faster surface potential equilibration.

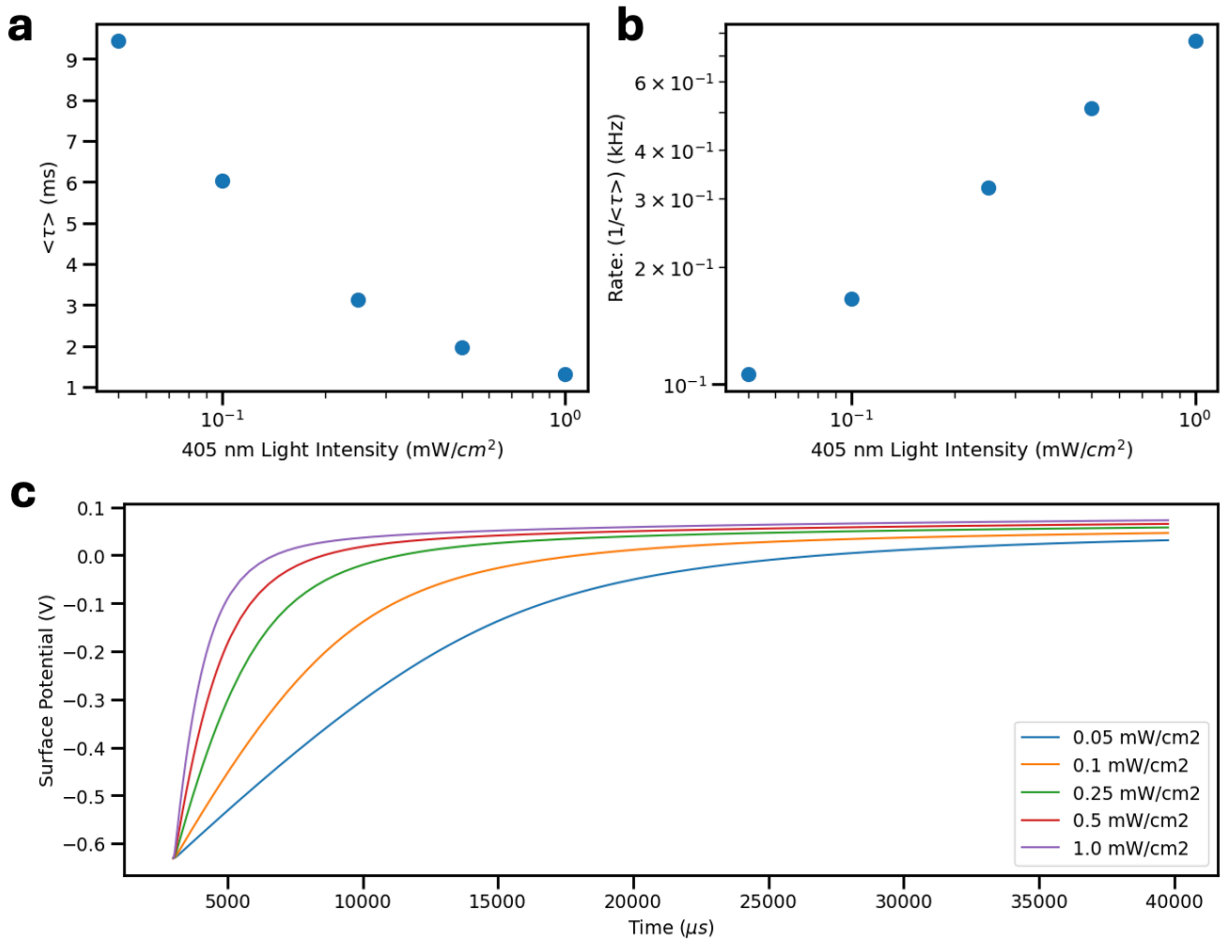

Figure 5.1: (a) Surface potential equilibration time constant plotted against excitation intensity with 405 nm excitation; (b) 1/<τ> or surface potential equilibration rate plotted against 405 nm excitation intensity, showing linear relationship between equilibration rate and log of excitation intensity. (c) Surface potential equilibration traces plotted over time with varied excitation intensities.

Indeed, these results confirmed that IonMonger accurately reproduced our results on OPVs, suggesting that in materials with low EQEs (like OPVs) the surface potential equilibration is efficiency-limited, capturing charging efficiency directly. In high quantum efficiency systems like lead halide perovskites, the surface potential equilibration also captures other dynamic processes, like electronic carrier recombination and ion motion.

Given an OPV material with an experimental EQE, I propose we calculate the carriers generated at a given excitation intensity and collect the other relevant parameters (e.g. thickness, bandgap, absorption coefficient for each excitation wavelength, etc.) to accurately simulate the system with IonMonger. From this, we can predict how the OPV would behave under different illumination conditions. Then, we can perform trEFM on a sample and compare the results to our simulations. Working with an expert on OPVs is critical so that we might understand potential effects of morphology, additives, or preparation methods that affect OPV performance. Overall, this project

would be a short, straightforward confirmation of our understanding of trEFM, revisiting a simpler semiconductor system and supporting our results with our newfound drift-diffusion approximation.

5.3 Conclusion and Outlook

Understanding the performance and quality of new semiconductor materials at all scales is paramount to developing long-lasting and efficient photovoltaic (and other optoelectronic) devices. Indeed, the heterogeneity we observe in properties such as PL, surface potential equilibration, surface photovoltage, and more at sub-diffraction-limited lengthscales can forecast the stability and efficiency of scaled up devices. Engineering better compositions, additives, and post-treatments for defect-tolerant (defect-containing) perovskite thin films will continue to require investigation at micrometer- and nanometer-scale spatial resolutions, meaning processing, analyzing, and interpreting multidimensional datasets from methods like trEFM, confocal trPL microscopy, EBSD, and more may necessitate the savvy and careful application of data science and machine learning. “Big Data” is an inviting nail for the hammer of machine learning.

This thesis focused on trEFM as a method of understanding sub-diffraction-limited surface potential equilibration dynamics on perovskite semiconductor materials. Such a multi-dimensional method easily leant itself to the application of ML to improve signal-to-noise and more accurately reconstruct our data. Overall, this work encompasses the application of trEFM as a method of nanoscale characterization on perovskites, but also the improvement on data processing, analysis, and reconstruction with machine learning.

5.4 References

1. Jariwala, S. *et al.* Local Crystal Misorientation Influences Non-radiative Recombination in Halide Perovskites. *Joule* 3, 3048–3060 (2019).
2. Adhyaksa, G. W. P. *et al.* Understanding Detrimental and Beneficial Grain Boundary Effects in Halide Perovskites. *Advanced Materials* 30, (2018).
3. Liu, Y. *et al.* Correlating Crystallographic Orientation and Ferroic Properties of Twin Domains in Metal Halide Perovskites. *ACS Nano* 15, 7139–7148 (2021).
4. Ran, J. *et al.* Electron-Beam-Related Studies of Halide Perovskites: Challenges and Opportunities. *Adv Energy Mater* 10, 1–19 (2020).
5. Breshears, M. D., Pothoof, J., Giridharagopal, R. & Ginger, D. S. Sub-diffraction Imaging of Carrier Dynamics in Halide Perovskite Semiconductors: Effects of Passivation, Morphology, and Ion Motion. *ArXiv* (2024).
6. Palmer, J. R. *et al.* Problems With Solutions: Manipulating Alkylammonium Additive Reactivity for Durable High-Quality Perovskite Films. *New J. Chem.* 1–10 (2025) doi:10.1039/D4NJ03915G.
7. Palmer, J. R. *et al.* Bismuth in Lead−Tin Alloy Perovskites: Effect on Material Properties and Photovoltaic Device Performance. *Appl. Energy Mater.* 7, 2726–2734 (2024).

8. Jones, T. W. *et al.* Lattice strain causes non-radiative losses in halide perovskites. *Energy Environ Sci* 12, 596–606 (2019).

9. DeQuilettes, D. W. *et al.* Impact of microstructure on local carrier lifetime in perovskite solar cells. *Science (1979)* 348, 683–686 (2015).

10. Breshears, M. D., Giridharagopal, R., Pothoof, J. & Ginger, D. S. A Robust Neural Network for Extracting Dynamics from Electrostatic Force Microscopy Data. *J. Chem. Inf. Model.* 62, 4342–4350 (2022).

11. Giridharagopal, R. *et al.* Time-Resolved Electrical Scanning Probe Microscopy of Layered Perovskites Reveals Spatial Variations in Photoinduced Ionic and Electronic Carrier Motion. *ACS Nano* 13, 2812–2821 (2019).

12. Cox, P. A. *et al.* Imaging Charge Transfer State Excitations in Polymer/Fullerene Solar Cells with Time-Resolved Electrostatic Force Microscopy. *J. Phys. Chem. Lett.* 6, 2852–2858 (2015).

13. Reid, O. G., Rayermann, G. E., Coffey, D. C. & Ginger, D. S. Imaging Local Trap Formation in Conjugated Polymer Solar Cells: A Comparison of Time-Resolved Electrostatic Force Microscopy and Scanning Kelvin Probe Imagin. *J. Phys. Chem. C.* 114, 20672–20677 (2010).

14. Coffey, D. C. & Ginger, D. S. Time-resolved electrostatic force microscopy of polymer solar cells. *Nat. Mater.* 5, 735–740 (2006).

15. Credgington, D. & Durrant, J. R. Insights from Transient Optoelectronic Analyses on the Open-Circuit Voltage of Organic Solar Cells. (2012) doi:10.1021/jz300293q.

16. Groves, C., Reid, O. G. & Ginger, D. S. Heterogeneity in Polymer Solar Cells: Local Morphology and Performance in Organic Photovoltaics Studied with Scanning Probe Microscopy. (2010) doi:10.1021/ar900231q.

17. Fukuda, K., Yu, K. & Someya, T. The Future of Flexible Organic Solar Cells. *Adv Energy Mater* 10, (2020).

18. Lin, K. *et al.* Perovskite light-emitting diodes with external quantum efficiency exceeding 20 per cent. *Nature* 562, (2018).

19. Ren, X., Wang, Z., Sha, W. E. I. & Choy, W. C. H. Exploring the Way To Approach the Efficiency Limit of Perovskite Solar Cells by Drift-Diffusion Model. (2017) doi:10.1021/acsphotonics.6b01043.

20. Best Research-Cell Efficiency Chart. *NREL* (2024).

21. Courtier, N. E., Richardson, G. & Foster, J. M. A fast and robust numerical scheme for solving models of charge carrier transport and ion vacancy motion in perovskite solar cells. *Appl. Math. Model.* 63, 329–348 (2018).

22. Courtier, N. E., Cave, J. M., Foster, J. M., Walker, A. B. & Richardson, G. How transport layer properties affect perovskite solar cell performance: insights from a coupled charge transport/ion migration model. *Energy Environ. Sci* 12, 396–409 (2019).

23. Courtier, N. E., Cave, · J M, Walker, · A B, Richardson, · G & Foster, · J M. IonMonger: a free and fast planar perovskite solar cell simulator with coupled ion vacancy and charge carrier dynamics. *J Comput Electron* 18, 1435–1449 (2019).

Appendix A: Supporting Information for Chapter 2

Note S1 on calibrating the cantilever for extraction of τ from instantaneous frequency data:

One key shortcoming of the current trEFM method is the discrepancy between the characteristic time constant, τ, defining the perturbation and the actual measured quantity, t_{FP} (Figure 1d in the text). For example, in the case where the excitation is a single exponential as is common in many physical phenomena, the expected change in the resonance frequency would also be a single exponential (Figure 1c in the text, green). The change in resonance frequency can be expressed as Equation S1:[1–3]

$$\omega_0(t \geq 0) \cong \omega_0(t = 0) + \Delta\omega_0\left(1 - e^{-t/\tau}\right) \qquad \text{Equation S1}$$

Where ω_0 is the resonance frequency, t is time (s), and τ is the characteristic time constant (s) that describes the frequency shift. However, the instantaneous frequency response (Figure 1c, blue) is clearly not a single exponential, due to the cantilever's relaxation to steady state frequency competing with the transient perturbation;[1] thus, t_{FP} is our metric for charging rate to compensate for the fact that the measured cantilever dynamics obfuscate the characteristic time constant, τ.

The current method to extract τ from the frequency signal is to calibrate each cantilever individually to correlate t_{FP} with τ. We do this one of two ways: (1) we apply voltage pulses of known τ values spanning the range of interest according to Equation S2 (Figure S1b) to a conductive substrate such as gold or ITO and measure the cantilever's response, demodulate the signal, and create a t_{FP}-τ calibration curve (Figure 1d in the text);[3] (2) alternatively, we can simulate a t_{FP}-τ calibration curve with the appropriate cantilever parameters.

$$V(t) = \Delta V(1 - e^{-t/\tau}) \qquad \text{Equation S2}$$

Where V is the voltage (V) between the tip and the sample, t is time (s), and τ is the time constant (s). The calibration process, though simple, is sensitive to t_{FP} extraction, which is dependent on noise among other factors. This problem easily lends itself to a machine learning solution, where we can use a neural network (NN) as seen in Figure 1e to map the entire instantaneous frequency signal to τ in a cantilever-agnostic way to ensure robust data interpretation for τ extraction.

Note S2 on the addition of noise to simulated data:

Random Gaussian noise was applied at varying levels to the simulated training dataset to ensure that the network learned on data that was as realistic as possible. The signal-to-noise ratio (SNR) was determined according to the following:

$$Noise\ Level(dB) = 10 \times \log_{10} V^2 - SNR \qquad \text{Equation S3}$$

Where V^2 is the signal power. Then, we can convert the desired noise level back to power and add Gaussian noise scaled to that noise level (centered at 0) back to the clean, simulated deflection signal.

Note S3 on Shapley Additive exPlanations (SHAP):

In the paper we used SHAP values to explore which portions of the instantaneous frequency signal were most instrumental in the network's regression and to probe the cantilever agnosticism of the network overall. SHAP values are calculated according to Equation S4:[4]

$$\phi_i(f, x) = \sum_{z' \subseteq x'} \frac{|z'|!(M-|z'|-1)}{M!}[f_x(z') - f_x(z'/i)] \qquad \text{Equation S4}$$

Where $\phi_i(f, x)$ is the SHAP value for feature i given the function f and input x, z' is a subset of features contained within the simplified input x' and specifically $|z'|$ is the number of non-zero entries in z', and M is the number of features. Critically, $f_x(z')$ is the result of the model or function given the subset z' including feature i and $f_x(z'/i)$ is the result of the model or function given the subset z' excluding the feature i. A SHAP value can be likened to the difference between the function output including feature i and the function output excluding the feature i, meaning SHAP is related to the feature's partial dependence plot in the context of regression.[4,5]

In terms of variables discussed in our case, let us consider an input array x' (containing k, Q, and $\omega(t)$). We want to understand the contribution to the network output of the specific instance of k (in terms of Equation S4, k is feature i). SHAP examines many subsets, z', of the input array x' that contain k. These subsets include or exclude other features in the input array (besides k, feature i) to disentangle the contribution of k, feature i, from the contributions of other features contained within x'. In our case, M is 100 because there are 100 input features. The first term of Equation S4 concerns how many ways we can choose the subset z' from x' (which contains M features). Essentially, it is weighting the marginal contributions calculated for z' by the inverse of the number of ways to pick z' from x'. The intuition is that smaller subsets, z', will tell us more about the feature we are inspecting. SHAP then calculates the difference of the model output given the input *with* the k instance (feature i) contained within the subset z' ($f_x(z')$) and *without* the k instance ($f_x(z'/i)$). SHAP sums these subset evaluations to account for the presence or absence of a random assortment of features. To create Figure 5, this process was repeated for all 3,000 test input arrays.

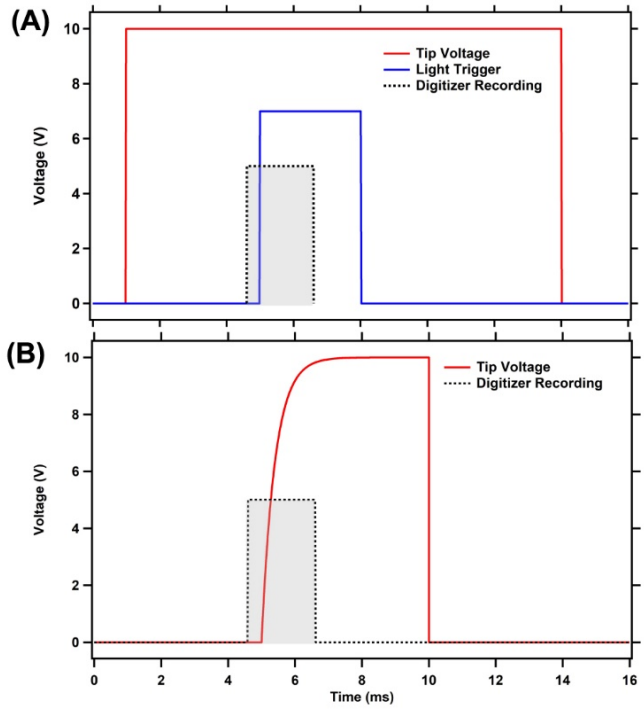

Figure S1: (a) Diagram depicting the waveforms that govern the tip voltage and light triggers for trEFM data collection. (b) Diagram depicting the voltage waveform applied to the tip when performing manual calibration as discussed in text.

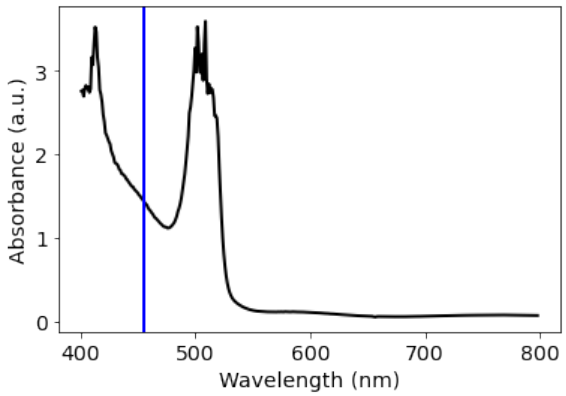

Figure S2: Absorbance of n-butylammonium lead iodide (BAPI) samples measured in study. Blue line indicates 455 nm LED used for optical excitation during trEFM experiments.

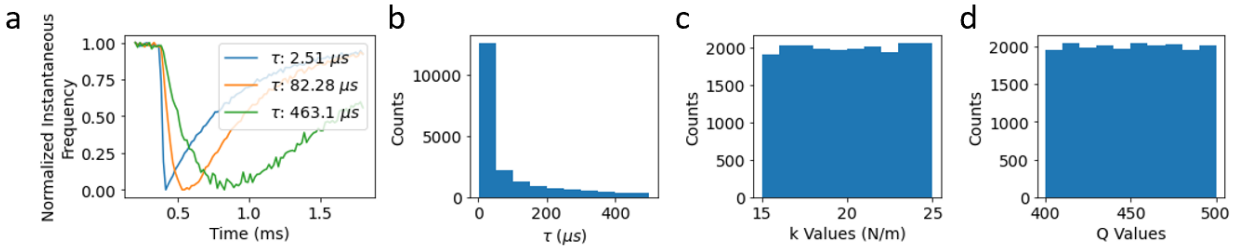

Figure S3: (a) Example of simulated normalized instantaneous frequency signals with τ values from 3 orders of magnitude where the shortest τ value also has the steepest frequency shift (therefore the shortest t_{FP}, related discussion in the text); (b) distribution of target τ values for simulated dataset; (c) uniform distribution of cantilever spring constants, k (N/m), used to simulate the training dataset; and (d) uniform distribution of cantilever Quality factors, Q (unitless), used to simulate the training dataset. Varying both k and Q in the simulated dataset ensured the network was cantilever-agnostic. Using a log-uniform distribution of τ values ensured the network learned the finer details of the data contained within each order of magnitude.

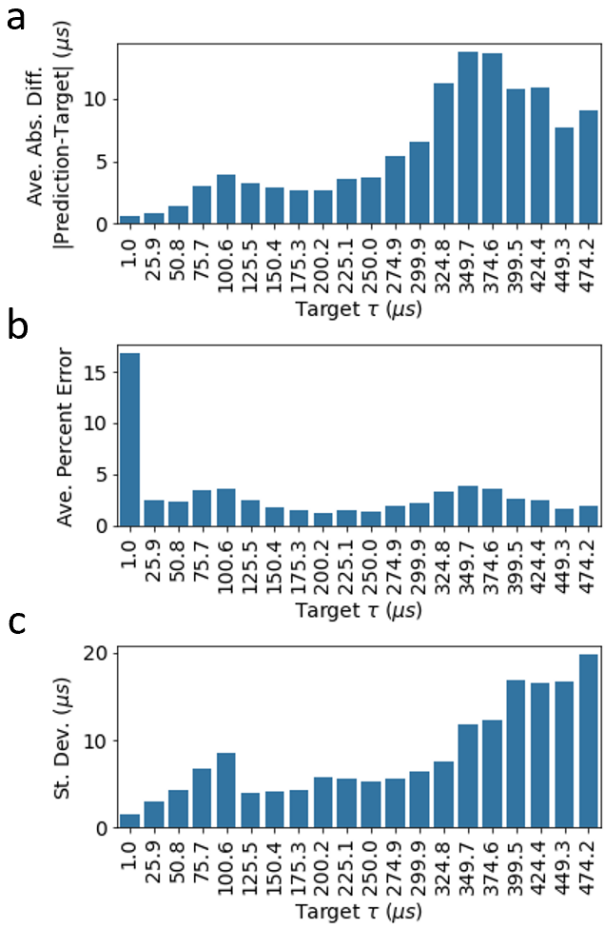

Figure S4: (a) Distribution of the average absolute difference between the network extracted τ value and the simulated ground truth τ value, where the absolute difference generally increases as the target τ value increases due to increased error in longer time regimes; (b) distribution of average

percent error of the network extracted τ value as compared to the simulated ground truth target τ value (note that the percent error is significantly higher in the 1 – 10 μs regime because small errors in the network τ value account for a larger percent of the target τ value); and (c) distribution of the average standard deviation across the target, simulated τ values showing increased standard deviations after 100 extractions. Standard deviation is calculated *via* the quasi-ensembling method discussed in the text. The standard deviation increases as the target τ value increases meaning there is less certainty in network extracted τ values in the slower time regimes.

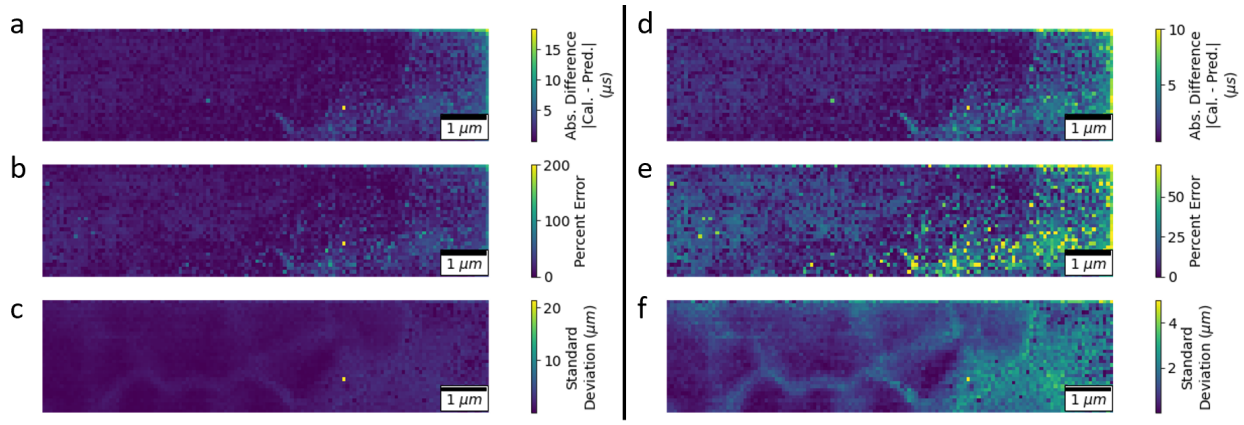

Figure S5: (a) Image of the absolute difference between the calibrated (ground truth) τ values and the network extracted τ values for trEFM data taken on BAPI where the absolute difference increases towards the right portion of the image, which is also reflected in (b) the image of the percent error of the calibrated (ground truth) τ values *vs*. the network extracted τ values for the same region of trEFM on BAPI; note that the single pixel achieving 200% error skews the color scale and that specific pixel also has the highest standard deviation as seen in (c) the image containing the standard deviation for each network extracted τ value for Figure 3(d) in the text. The standard deviation was calculated using the quasi-ensembling method described in the text. (d), (e), and (f) show the absolute difference, percent error, and standard deviation with the color scale adjusted for ease of viewing.

Comparing light-dependent photocharging data:

As mentioned in the discussion regarding main text Figure 3g, in photovoltaic samples, we expect the charging rate to increase with higher light intensity.[1, 2] To validate the results shown for the network, we adjust the light intensity from 42.1 W/m^2 to 203.6 W/m^2 and compare the predicted NN outputs. These data are shown for 3 different intensities in Figure. S6-8, and they are summarized in Table S1.

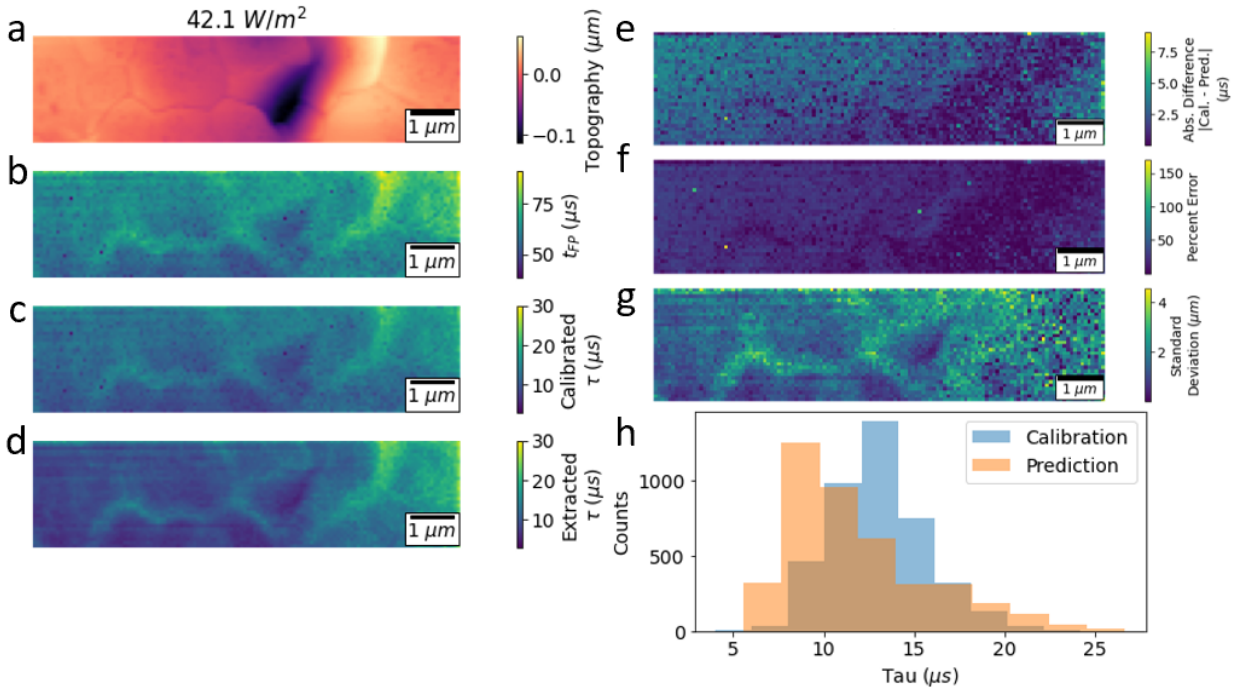

Figure S6: (a) Topography of the same BAPI region as shown in Figure 3 of the text; (b) associated image of the t_{FP} values from the trEFM data and (c) the calibrated τ values that we treat as ground truth; (d) the network extracted τ values averaged over 100 predictions as per the quasi-ensembling method; (e) the absolute difference, (f) percent error, and (g) standard deviation images for the same region generally demonstrating good agreement between the ground truth and network extracted τ values, which can also be seen in (h) where histograms of the calibrated (ground truth) and network extracted τ values are overlayed. Figure S4 is based on data collected with a 455 nm LED intensity of 42.1 W/m^2.

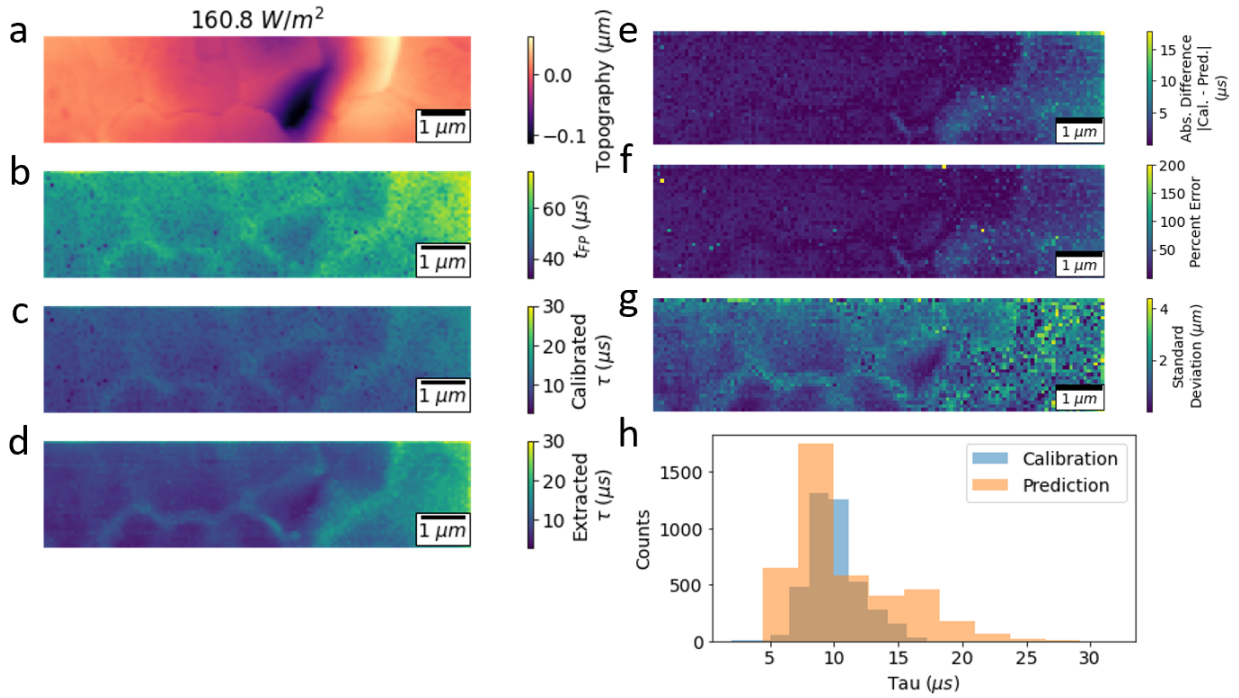

Figure S7: (a) Topography of the same BAPI region as shown in Figure 3 of the text; (b) associated image of the t_{FP} values from the trEFM data and (c) the calibrated τ values that we treat as ground truth; (d) the network extracted τ values averaged over 100 predictions as per the quasi-ensembling method; (e) the absolute difference, (f) percent error, and (g) standard deviation images for the same region generally demonstrating good agreement between the ground truth and network extracted τ values, which can also be seen in (h) where histograms of the calibrated (ground truth) and network extracted τ values are overlayed. Figure S4 is based on data collected with a 455 nm LED intensity of 160.8 W/m^2.

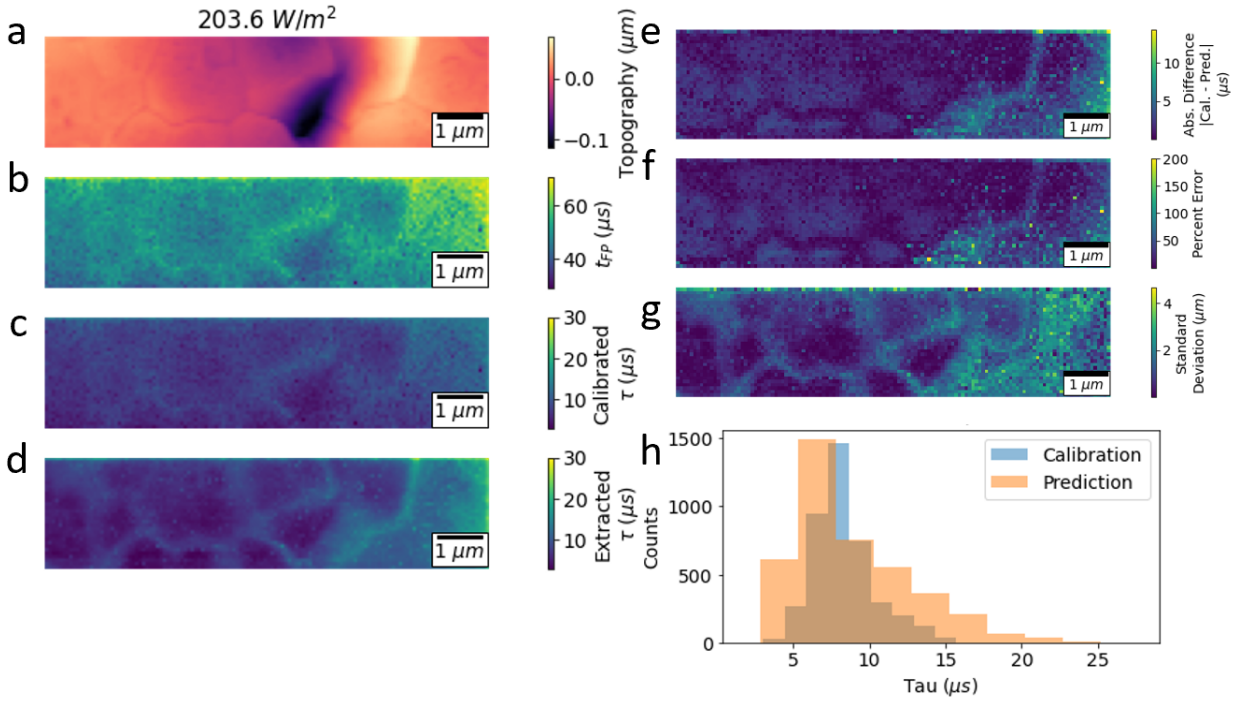

Figure S8: (a) Topography of the same BAPI region as shown in Figure 3 of the text; (b) associated image of the t_{FP} values from the trEFM data and (c) the calibrated τ values that we treat as ground truth; (d) the network extracted τ values averaged over 100 predictions as per the quasi-ensembling method; (e) the absolute difference, (f) percent error, and (g) standard deviation images for the same region generally demonstrating good agreement between the ground truth and network extracted τ values, which can also be seen in (h) where histograms of the calibrated (ground truth) and network extracted τ values are overlayed. Figure S4 is based on data collected with a 455 nm LED intensity of 203.6 W/m^2.

Power Intensity (W/m^2)	**Absolute Difference (μs)**		**Percent Error**		**Standard Deviation (μs)**	
	Mean	**Median**	**Mean**	**Median**	**Mean**	**Median**
42.1	2.23	2.25	17.56	18.07	1.79	1.72
109.9	1.54	1.12	17.80	14.28	1.17	0.99
160.8	2.11	1.54	20.19	16.19	1.41	1.33
203.6	2.07	1.60	25.56	20.06	1.12	0.99

Table S1: Summary mean and median absolute differences, percent errors, and standard deviations for data shown in Figures S4-S5.

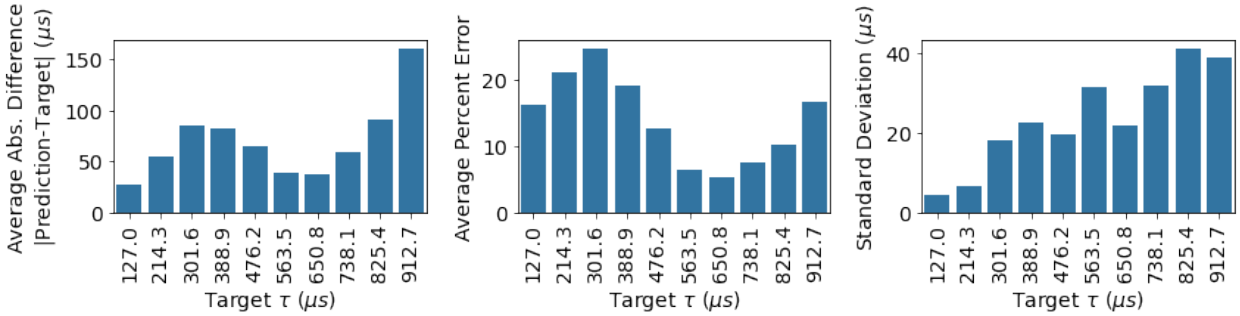

Figure S9: Distributions of error metrics for Figure 4 in the text where (a) is the distribution of average absolute difference between ground truth τ value fed to ITO substrate per Equation 1 in text and network extracted τ value; (b) is the distribution of average percent errors for the same data; and (c) is the distribution for the average standard deviations for these calibrated τ values.

References

(1) Giridharagopal, R.; Rayermann, G. E.; Shao, G.; Moore, D. T.; Reid, O. G.; Tillack, A. F.; Masiello, D. J.; Ginger, D. S. Submicrosecond Time Resolution Atomic Force Microscopy for Probing Nanoscale Dynamics. *Nano Letters* **2012**, *12* (2), 893–898. https://doi.org/10.1021/nl203956q.

(2) Giridharagopal, R.; Precht, J. T.; Jariwala, S.; Collins, L.; Jesse, S.; Kalinin, S. v.; Ginger, D. S. Time-Resolved Electrical Scanning Probe Microscopy of Layered Perovskites Reveals Spatial Variations in Photoinduced Ionic and Electronic Carrier Motion. *ACS Nano* **2019**, *13* (3), 2812–2821. https://doi.org/10.1021/acsnano.8b08390.

(3) Karatay, D. U.; Harrison, J. S.; Glaz, M. S.; Giridharagopal, R.; Ginger, D. S. Fast Time-Resolved Electrostatic Force Microscopy: Achieving Sub-Cycle Time Resolution. *Review of Scientific Instruments* **2016**, *87* (5), 053702. https://doi.org/10.1063/1.4948396.

(4) Lundberg, S.; Lee, S.-I. A Unified Approach to Interpreting Model Predictions. *arXiv* **2017**.

(5) Rozemberczki, B.; Watson, L.; Bayer, P.; Yang, H.-T.; Kiss, O.; Nilsson, S.; Sarkar, R. The Shapley Value in Machine Learning. *arXiv* **2022**.

Appendix B: Supporting Information for Chapter 3

Appendix B Fig. 1: Distributions of cantilever parameters for simulated training dataset.

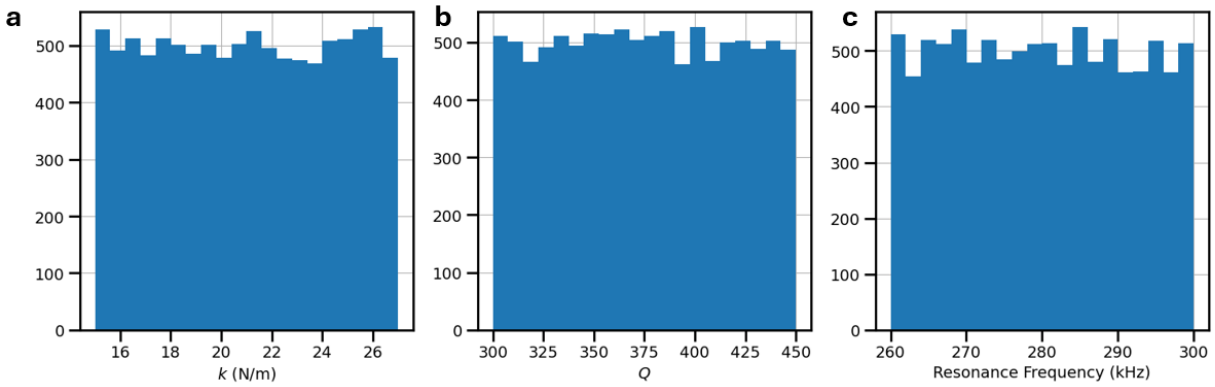

(a) Distribution of cantilever spring constant, k (N/m), values used for simulated training data. (b) Distribution of cantilever quality factor, Q (unitless), values used for simulated training data. (c) Distribution of resonance frequency, ω_0 (kHz), values used for simulated training data.

Appendix B Fig 2: Distributions of bi-exponential parameters used for simulated training datasets.

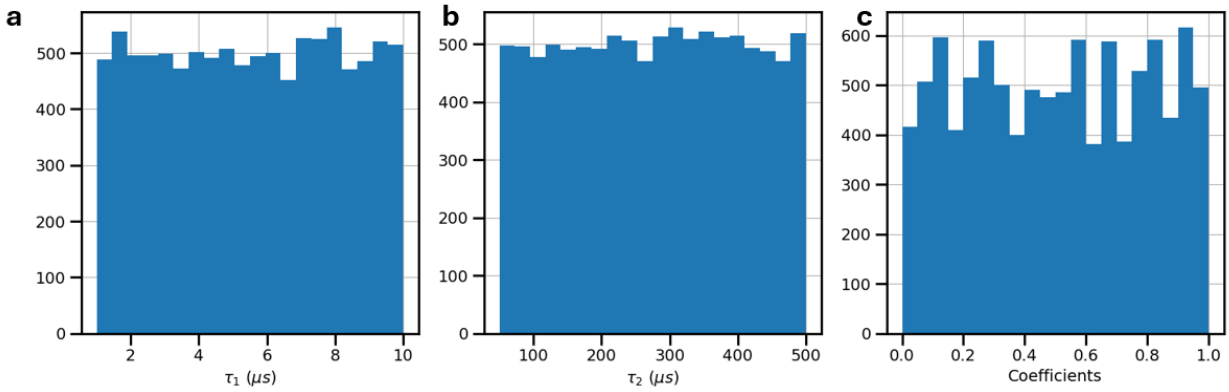

(a) Distribution of τ_1 (μs) values used in simulated training datasets. (b) Distribution of τ_2 (μs) values used in simulated training datasets. (c) Distribution of coefficient, A, values used in simulated training. Refer to Equation 1 in the main text.

Appendix B Fig 3: Effect of bi-exponential parameters on cantilever frequency signal.

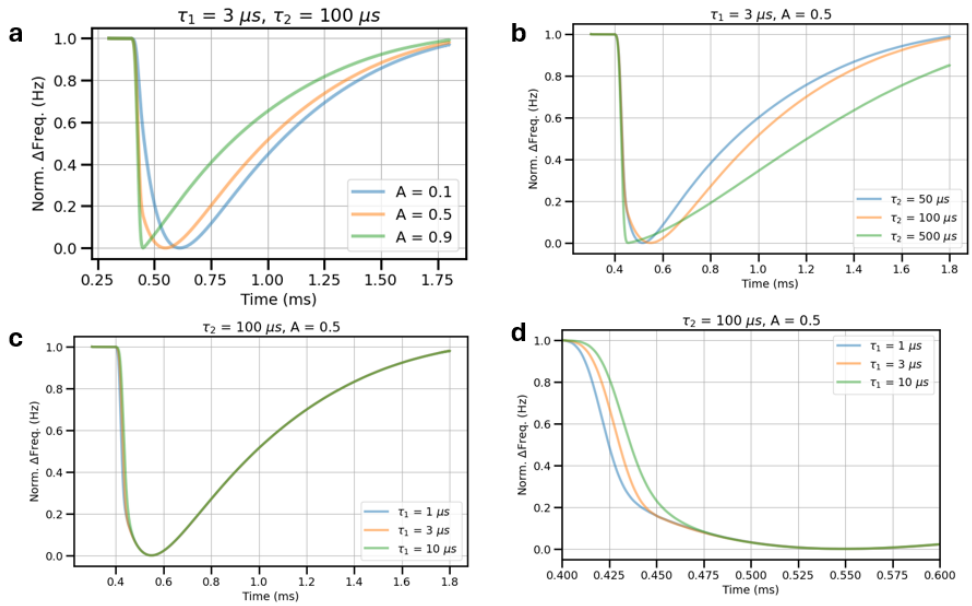

(a) Example simulated $\Delta\omega(t)$ traces following bi-exponential perturbations triggered at t=0.4 ms, where τ_1 and τ_2 are held constant at 3 µs and 100 µs respectively, and A (coefficient) is varied; refer to Equation 1 in the main text. (b) Simulated $\Delta\omega(t)$ traces where τ_1 and A are held constant at 3 µs and 0.5 respectively, and τ_2 is varied. (c) and (d) show simulated $\Delta\omega(t)$ traces where τ_2 and A are held constant and τ_1 is varied, showing slight variations in initial transient response after trigger at t=0.4 ms. All simulations performed with the FFTA code package (available at: https://github.com/rajgiriUW/ffta).

Appendix B Note 1: On the custom error function used in the multioutput CNN.

Given that each training label for τ_1, τ_2, and A (coefficient) is normalized between 0 and 1 to prevent exploding or vanishing gradients during training,[1,2] the error function used to penalize the network during training must reflect the difficulty of learning the patterns that correspond to each parameter. For instance, the subtleties of changing τ_1 (while holding τ_2 and A constant) as shown in Appendix B Fig. XX mean penalizing mistakes when predicting τ_1 is more important than penalizing mistakes when predicting τ_2 or A. After sweeping the coefficients for the mean squared error (MSE) of each parameter, we found the following combination enabled efficient and accurate learning of all three parameters:

$$criterion = 2.5 \times MSE\left(\tau_{1,true}, \tau_{1,pred}\right) + 1.75 \times MSE\left(\tau_{2,true}, \tau_{2,pred}\right) + 1 \times MSE\left(A_{true}, A_{pred}\right)$$

Where MSE is the mean squared error between the true and predicted parameter.

Appendix B Fig 4: Parity plots showing trained CNN performance on simulated test dataset.

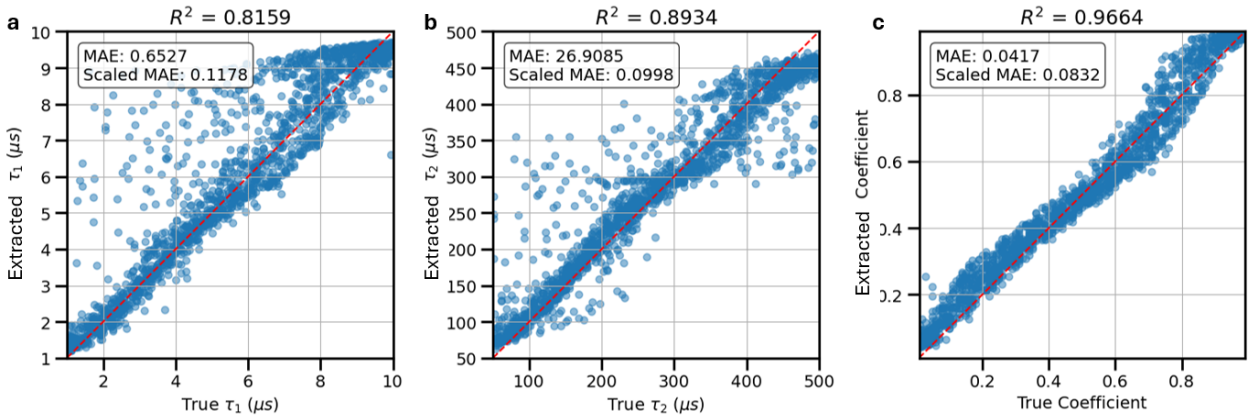

(a) Parity plot showing trained (not fine-tuned) CNN performance on test simulated data when predicting τ_1 (μs). (b) Parity plot showing trained (not fine-tuned) CNN performance on test simulated data when predicting τ_2 (μs). (c) Parity plot showing trained (not fine-tuned) CNN performance on test simulated data when predicting coefficient, A. R^2 scores comparing the extracted value versus the true value are on the title of each plot. "MAE" stands for the mean average error; for τ_1 and τ_2 the MAE is in μs, and for A it is unitless. The "Scaled MAE" is the MAE divided by the average true value for the given parameter.

Appendix B Fig 5: Parity plots showing CNN performance on labeled experimental dataset after fine-tuning.

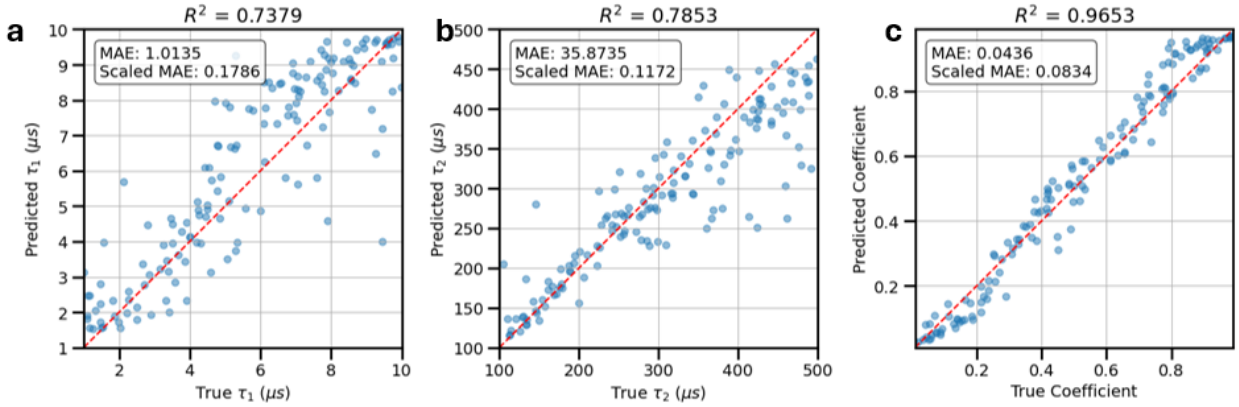

(a) Parity plot showing fine-tuned CNN performance on test labeled experimental data when predicting τ_1 (μs). (b) Parity plot showing fine-tuned CNN performance on test labeled experimental data when predicting τ_2 (μs). (c) Parity plot showing fine-tuned CNN performance on test labeled experimental data when predicting coefficient, A. R^2 scores comparing the extracted value versus the true value are on the title of each plot. "MAE" stands for the mean average error; for τ_1 and τ_2 the MAE is in μs, and for A it is unitless. The "Scaled MAE" is the MAE divided by the average true value for the given parameter.

Appendix B Note 2: On the variation in error metrics for each parameter after fine-tuning.

We hypothesize that the network will extract the coefficient, A, with the most accuracy, because the relative contribution between fast and slow components shows a significant effect on the signal (Appendix B Fig. 3). We also normalized all labels between 0 and 1 during training to prevent exploding gradients,[2] but A already ranged between 0 and 1, and as such we expect that the network will perform better when extracting this parameter. Not only are the effects of τ_1 and τ_2 on the $\Delta\omega(t)$ signal more subtle (Appendix B Fig. 3), but by normalizing the labels corresponding to both τ_1 and τ_2, we expect that the resulting un-normalized error will be slightly larger compared to the error for A. The mean average error for τ_1 was 1.01 μs, for τ_2 was 35.87 μs, and for A was 0.04 (a mean percent error of 17.6%, 11.7%, and 8.3% respectively); and the R^2 score for each parameter's parity plot was 0.74, 0.79, and 0.97 respectively, as expected.

Appendix B Fig 6: Artificial image parameter truths and extracted values.

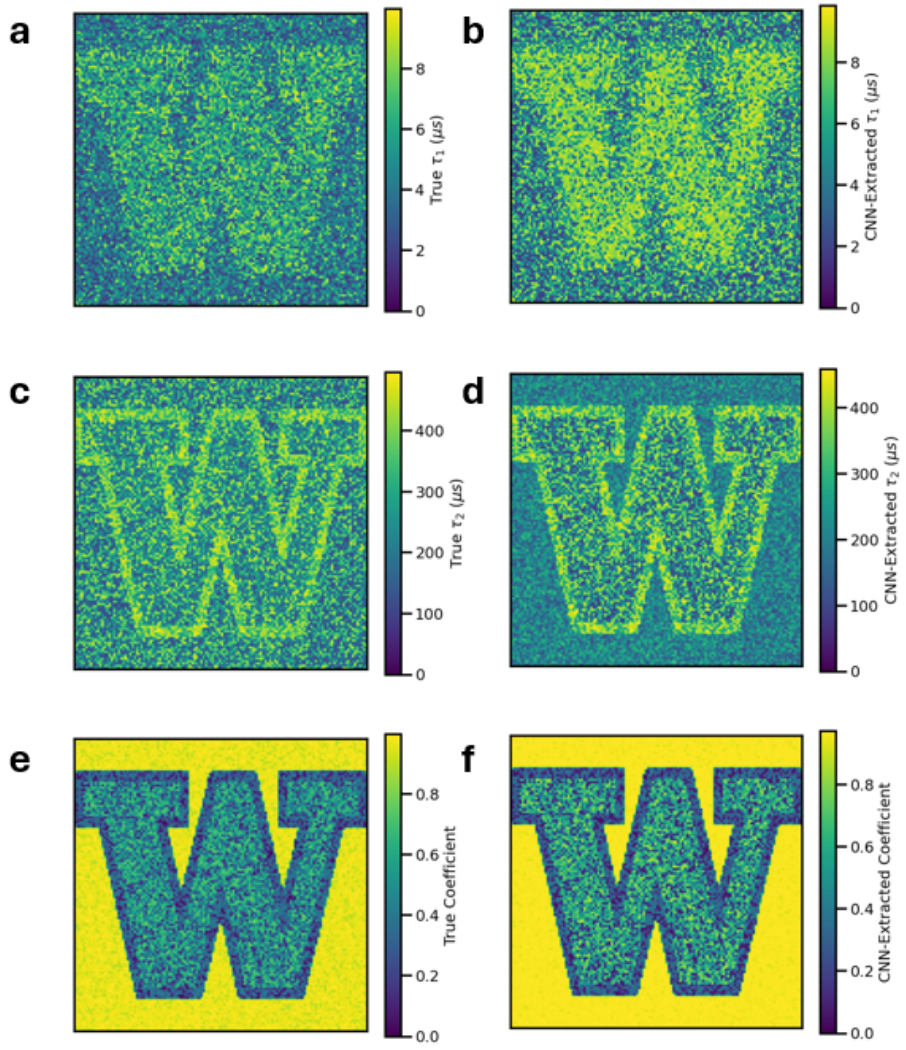

(a), (c), and (e) show the map of each parameter (τ_1, τ_2, and A) that constructs the artificial image shown in main text Figure XX. (b), (d), and (f) show the CNN-extracted parameter.

Appendix B Fig 7: Comparison of fine-tuned CNN and single-exponential neural network on artificial image.

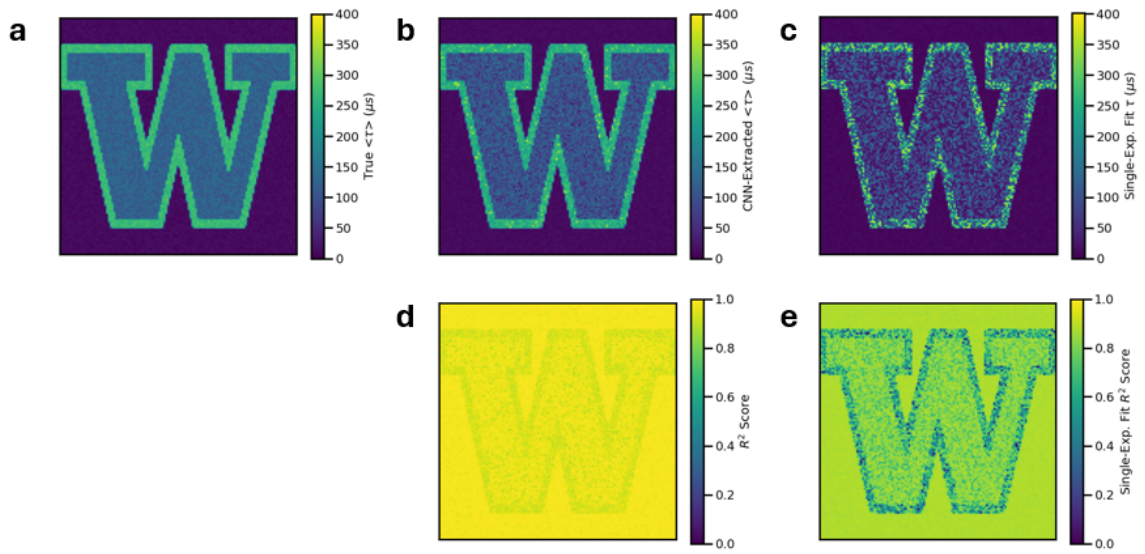

(a) Artificially constructed <τ> image (see Equation 2 in main text). (b) CNN-extracted <τ> image, showing relatively good agreement with (a) by eye. (c) Map of τ values obtained from feeding artificial image (with bi-exponential perturbations) into single-exponential feedforward neural network from previous work,[3] showing increased noise. (d) Map of R^2 values comparing the true data used to construct the artificial image compared to Δω(t) traces simulated from CNN-extracted parameters, where an R^2 value of 1 would indicate perfect signal reconstruction. (e) Map of R^2 values comparing the true data used to construct the artificial image compared to Δω(t) traces simulated from the single-exponential fit shown in (c).

Appendix B Note 3: On adding artificial Gaussian noise to simulated instantaneous frequency signals.

We collect the cantilever's raw oscillation and then demodulate it to its instantaneous frequency. To accurately mimic this process, we introduce Gaussian noise to a simulated cantilever oscillation before demodulating it to obtain the instantaneous frequency. We add the noise according to the following instructions:

1. $\overline{P_{signal}} = mean(Z^2)$, where P_{signal} is the average power of the signal Z.
2. We convert that to decibels via: $\overline{P_{signal,dB}} = 10 * \log(\overline{P_{signal}})$.
3. We calculate the power of the desired noise level (in decibels) with: $P_{noise,dB} = P_{signal,dB} - SNR_{desired}$.
4. $\overline{P_{noise}} = 10^{\frac{P_{noise,dB}}{10}}$, allows us to calculate the overall power of the noise.

We generate an array of Gaussian noise centered at 0 with a standard deviation of the square root of $\overline{P_{noise}}$ to add to our clean simulated signal (Z).

After we demodulate the signal (see main text Methods), we are left with the transform of that Gaussian noise, meaning our $SNR_{desired}$ value does not accurately represent the noise level of the signal. To obtain SNR_{final}, we do the following:

1. $noise = Z_{noisy} - Z$ gives us the noise by subtracting the clean signal (Z) from the noisy signal (Z_{noisy}).
2. $\overline{P_{signal}} = mean(Z^2)$ gives us the power of the signal, just like before.
3. $\overline{P_{noise}} = mean(noise^2)$ gives us the power of the noise.
4. To calculate the SNR_{final}, we need to compare the powers in decibels. We can obtain that ratio according to the following: $SNR_{final} = 10 * \log\left(\frac{\overline{P_{signal}}}{\overline{P_{noise}}}\right)$.

Appendix B Figs. 8a-c show example simulated Δω(t) traces with artificial Gaussian noise applied according to this method. Appendix B Figs. 8d-e show how well the multi-output CNN extracts accurate <τ> values from increasing noisy (decreasing SNR) simulated data. (Appendix B Figs. 8d-e also compare the single-exponential neural network's performance.) At SNRs of as low as ~7 the multi-output CNN parameters enable data reconstruction with an R^2 score of 0.9, meaning the dynamics we extract assuming a bi-exponential perturbation more accurately represent the dynamics we are interested in at higher noise levels.

Appendix B Fig 8: Evaluation of the limits of noise on single-exponential feedforward neural network and multi-output convolutional neural network.

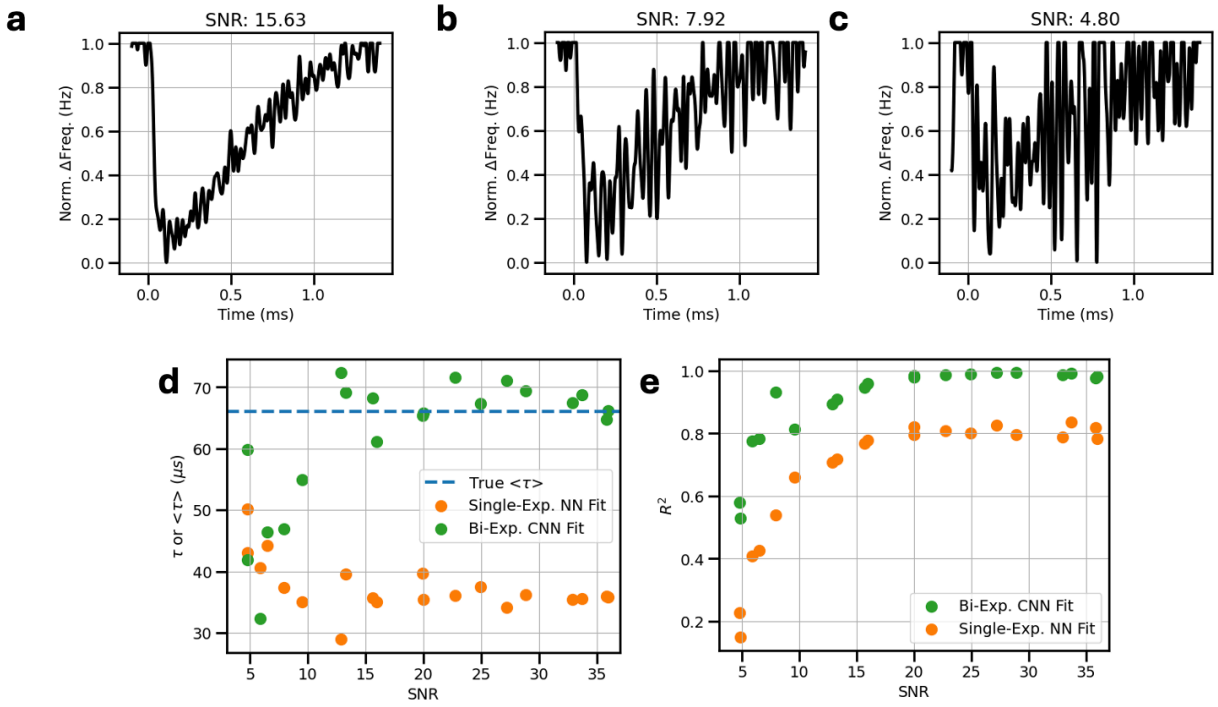

(a)-(c) Example simulated Δω(t) traces with varied levels of Gaussian noise added via the process described in Appendix B Note 3. (d) Scatter plot showing single-exponential neural network[3] and multioutput CNN performance on a simulated signal with increasing levels of Gaussian noise. Refer to Appendix B Note 3 for discussion on how noise was added to the simulated signal. (e) R^2 score comparing how well each network (single-exponential or multioutput CNN) reconstructed noisy data according to increasing signal-to-noise ratio, showing that multioutput CNN better reconstructs noisy data.

Appendix B Fig 9: SHAP analysis exploring the impact of each cantilever parameter.

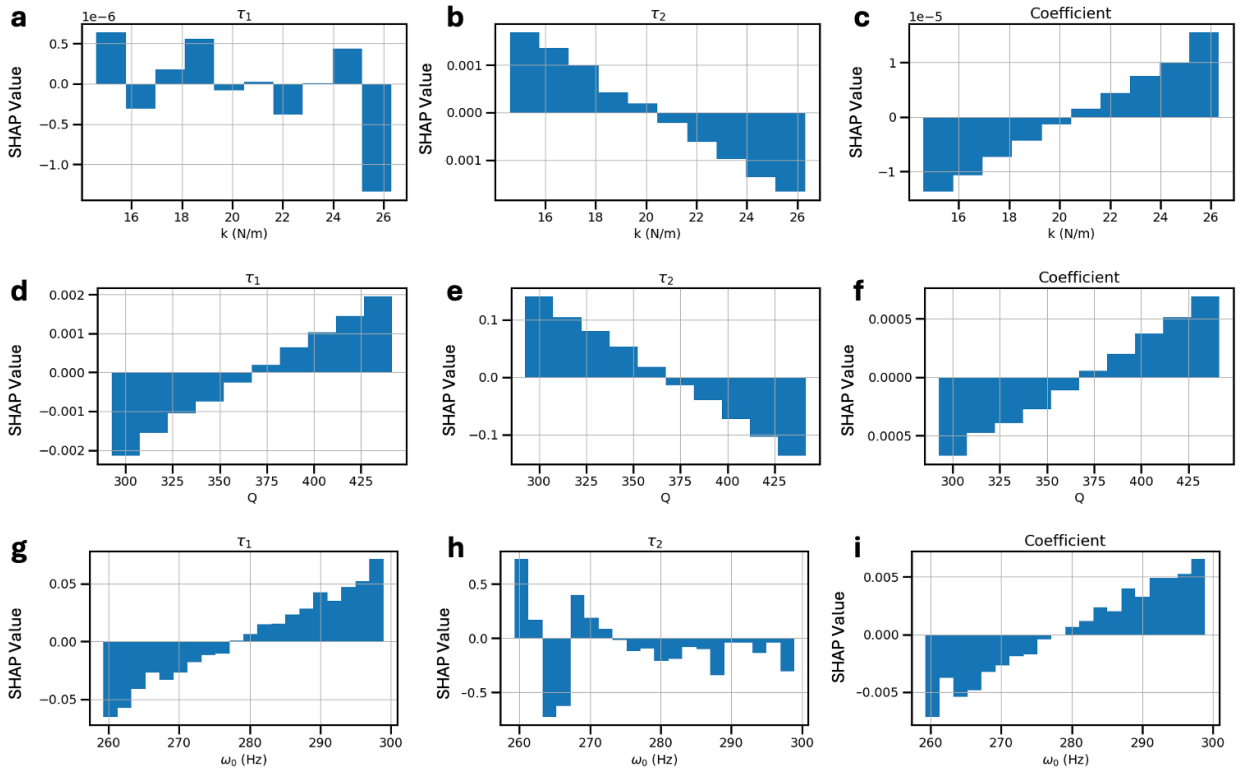

(a)-(c) SHAP value distributions plotted against cantilever spring constants (k, N/m) showing how varied spring constants affect the overall model output for each parameter (τ_1, τ_2, and A); note how small the SHAP values are, indicating that k has little to no effect on the model output. (d)-(f) SHAP value distributions plotted against cantilever quality factors (Q, unitless) showing how varied quality factors affect the overall model output for each parameter (τ_1, τ_2, and A); note that the SHAP values themselves are larger in magnitude compared to k, indicating Q does have an effect on the model output. This agrees with our previous work and understanding that Q primarily governs the cantilever frequency relaxation after the initial perturbation.[3–6] (g)-(i) SHAP value distributions plotted against cantilever resonance frequency (ω_0, kHz) showing how varied resonance frequencies affect the overall model output for each parameter (τ_1, τ_2, and A); from these distributions, we see that the magnitude of SHAP values is relatively small compared to the magnitude of the parameter outputs, suggesting that resonance frequency does not significantly impact the model's prediction.

Appendix B Fig 10: SHAP analysis revealing frequency signal impact on model output for τ_1.

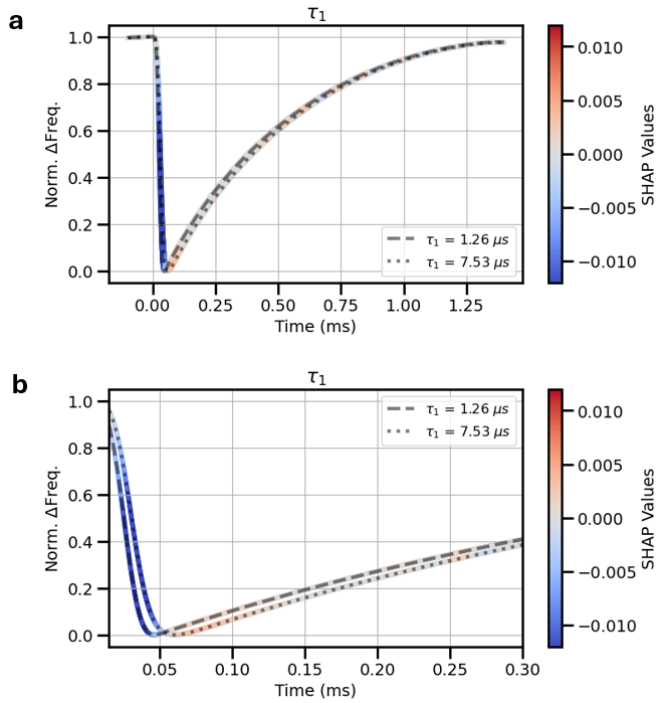

(a) SHAP analysis revealing initial frequency shift has biggest impact on (highest density of positive/negative SHAP values) on model output corresponding to τ_1. (b) Zoomed in on trigger region to show small density of positive SHAP values that correspond to larger value of τ_1. For these examples, τ_2 was held at 72.53 μs and A was held at 0.9 (a large contribution of τ_1). Examples were simulated using the FFTA code package, freely available at https://github.com/rajgiriUW/ffta.

Appendix B Fig 11 SHAP analysis revealing frequency signal impact on model output for τ_2.

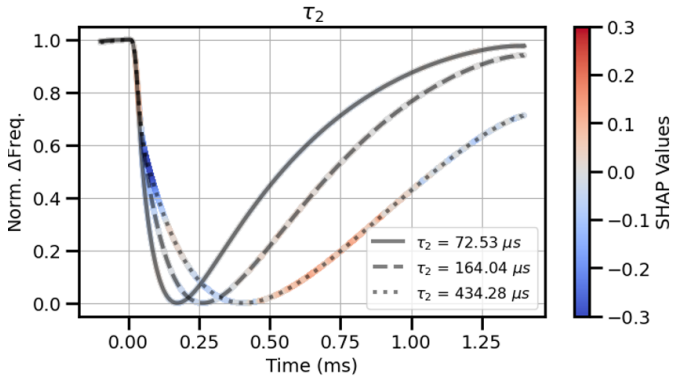

SHAP analysis revealing initial frequency shift has the biggest impact (highest density of positive/negative SHAP values) on model output corresponding to τ_2.

Appendix B Fig 12: Individual parameter maps for experimental data shown in main text Figure 5.

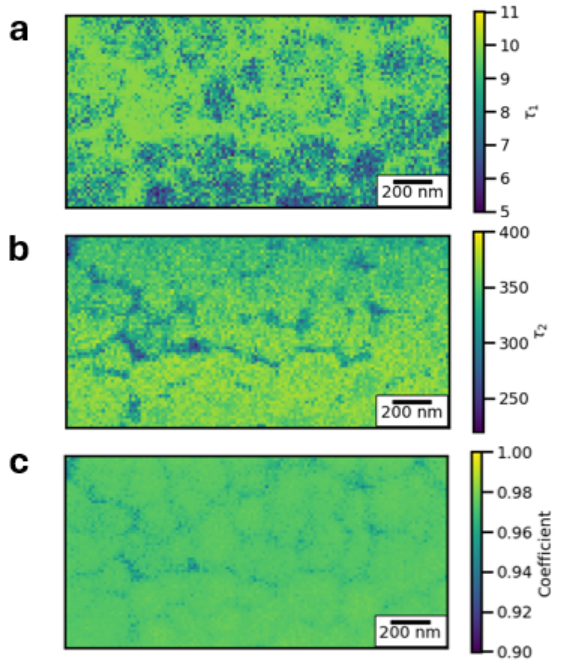

(a) Multioutput CNN map of extracted τ_1 values (μs) corresponding to trEFM image collected on **ITO/Me-4PACz/$Cs_{0.17}FA_{0.83}Pb(I_{0.85}Br_{0.15})_3$** *described in main text and shown in Figure 5. (b) Multioutput CNN map of extracted τ_2 values (μs) corresponding to trEFM image described in main text and shown in Figure 6. (c) map of extracted coefficient (A) values corresponding to trEFM image described in main text and shown in Figure 5.*

Appendix B Fig 13: Signal reconstruction R^2 map.

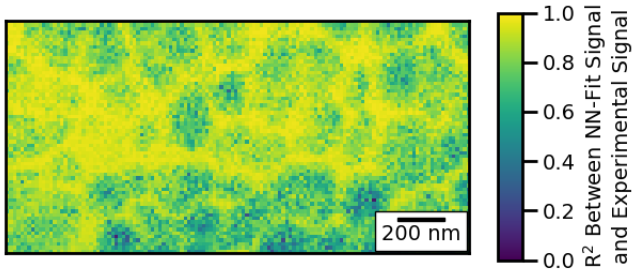

Map of R^2 values comparing experimental data with signals simulated with multioutput CNN parameters, evaluating how well the CNN parameters reconstruct the experimental data.

Appendix B Fig 14: Single-exponential neural network time constant map and signal reconstruction R^2 map for main text Figure 5.

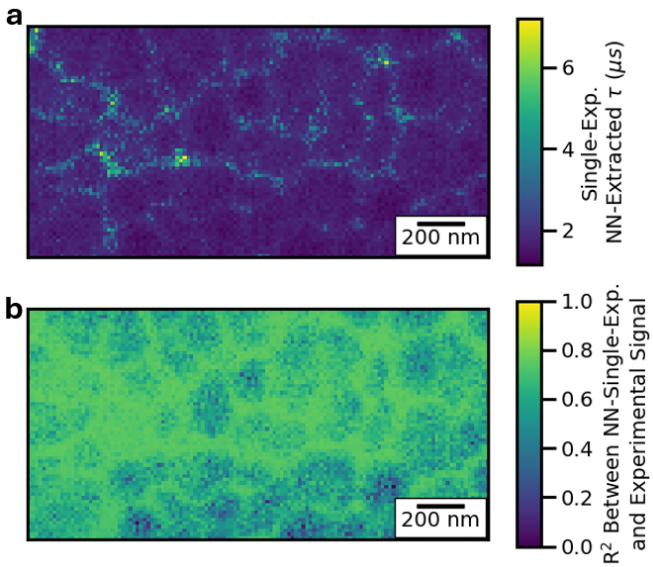

(a) Map of τ values (μs) generated from single-exponential feedforward neural network on experimental trEFM image on **ITO/Me-4PACz/$Cs_{0.17}FA_{0.83}Pb(I_{0.85}Br_{0.15})_3$** *described in main text and shown in main text Figure 5. (b) Map of R^2 values comparing experimental data with signals simulated with single-exponential feedforward neural network[3] parameters, evaluating how well the single-exponential network reconstruct the experimental data.*

Appendix B Fig 15: Random seed testing shows approach is generalizable and not reliant on chosen seed.

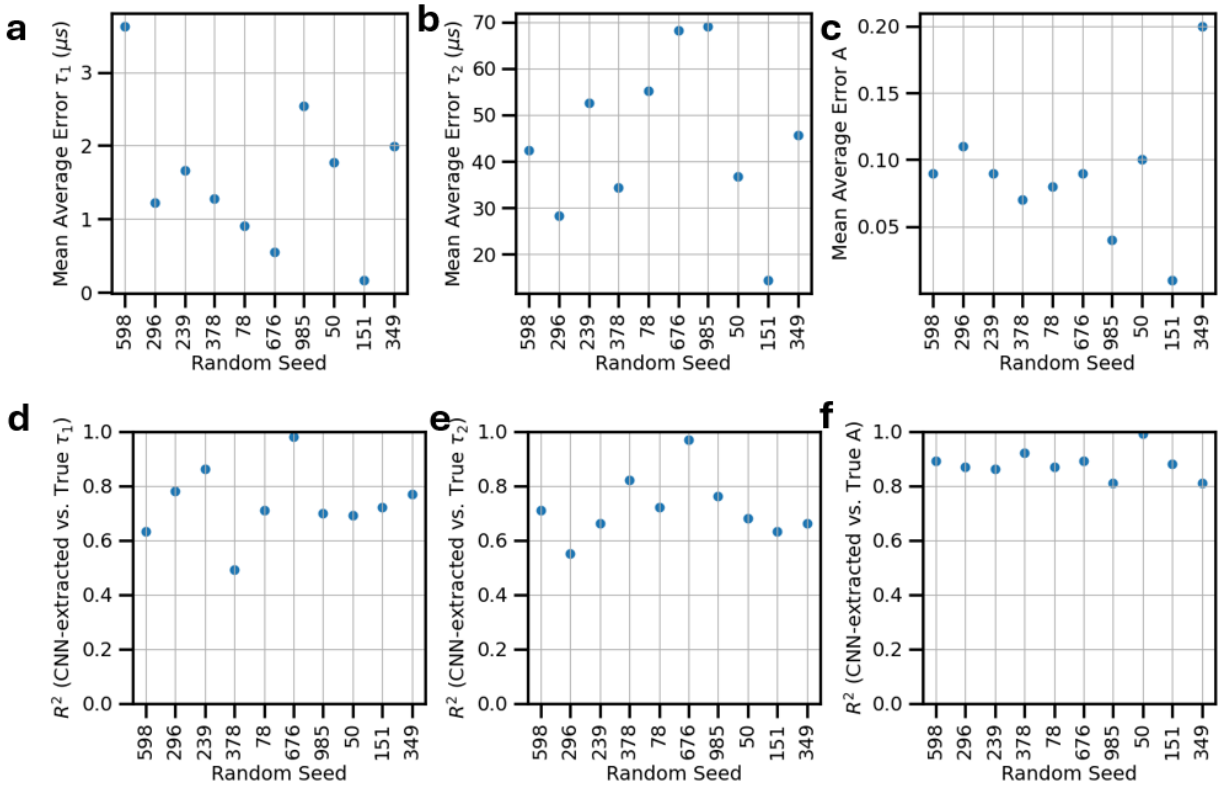

(a)-(c) Mean average error of trained network on τ_1, τ_2, and A respectively with varied random seed initializations, showing relatively consistent performance. (d)-(f) R^2 scores of CNN-extracted vs. true parameter values for τ_1, τ_2, and A. respectively, showing consistent, fair performance. Note that A is consistently predicted more accurately than each τ parameter, which we attribute to the normalization of the parameters during training leading to more accurate and consistent performance after un-normalizing.

References

(1) Dai, Z.; Heckel, R. Channel Normalization in Convolutional Neural Networks Avoids Vanishing Gradients. 2019.

(2) Song, H.; Kim, M.; Park, D.; Shin, Y.; Lee, J.-G. Learning From Noisy Labels with Deep Neural Networks: A Survey. *IEEE Trans Neural Netw Learn Syst* 2023, *34*, 8135–8153.

(3) Breshears, M. D.; Giridharagopal, R.; Pothoof, J.; Ginger, D. S. A Robust Neural Network for Extracting Dynamics from Electrostatic Force Microscopy Data. *J. Chem. Inf. Model.* 2022, *62* (18), 4342–4350.

(4) Tirmzi, A. M.; Dwyer, R. P.; Jiang, F.; Marohn, J. A. Light-Dependent Impedance Spectra and Transient Photoconductivity in a Ruddlesden-Popper 2D Lead-Halide Perovskite Revealed by Electrical Scanned Probe Microscopy and Accompanying Theory. *J. Phys. Chem. C* 2020, *124*, 13639–13648. https://doi.org/10.1021/acs.jpcc.0c04467.

(5) Giridharagopal, R.; Rayermann, G. E.; Shao, G.; Moore, D. T.; Reid, O. G.; Tillack, A. F.; Masiello, D. J.; Ginger, D. S. Submicrosecond Time Resolution Atomic Force Microscopy for Probing Nanoscale Dynamics. *Nano Lett.* 2012, *12*, 893–898. https://doi.org/10.1021/nl203956q.

(6) Harrison, J. S.; Waldow, D. A.; Cox, P. A.; Giridharagopal, R.; Adams, M.; Richmond, V.; Modahl, S.; Longstaff, M.; Zhuravlev, R.; Ginger, D. S. Noncontact Imaging of Ion Dynamics in Polymer Electrolytes with Time-Resolved Electrostatic Force Microscopy. *ACS Nano* 2019, *13*, 536–543. https://doi.org/10.1021/acsnano.8b07254.

Appendix C: Supporting Information for Chapter 4

Appendix C Note 1. Cantilever calibration for trEFM time constant extraction.

The experimental and theoretical background behind trEFM is described in significant detail in our previous works[1,2] and by Tirmzi, et al.[3] Here, we summarize the cantilever calibration procedure for the sake of reference.

During the trEFM experiment, we digitize the deflection or the raw oscillation of the cantilever, and then we demodulate it using a Short-Time Fourier Transform (STFT). Many demodulation methods work, such as non-stationary Fourier mode decomposition,[4] which demonstrates improved signal-to-noise extraction but is computationally expensive and slow. Hilbert Transforms[1,5] are computationally fast, but less robust to the experimental noise we observe. Thus, we use STFT to demodulate our data to balance the signal-to-noise we obtain and computation time. We then use a product of two exponentials (**Equation 1**) to empirically fit the change in frequency (Δf), including the transient response and cantilever relaxation (shown in main text Fig. 1c), and extract the time it takes for the cantilever's frequency to shift to its maximum deviation from the drive frequency after the illumination trigger.

Equation 1.

$$\Delta f = A \times \left[\exp\left(-\frac{t}{\tau_1}\right) - 1\right] \times \left[-\exp\left(-\frac{t}{\tau_2}\right)\right]$$

Where A is a coefficient that accounts for the magnitude of the frequency shift, t is time, τ_1 describes the transient decay, and τ_2 describes the cantilever relaxation.

We call the time it takes for the cantilever's frequency to shift to its maximum deviation from the drive frequency the "time-to-first-peak" or t_{fp}. The t_{fp} is cantilever-dependent, meaning physical qualities of the cantilever like its spring constant or quality factor affect the frequency response. Because the frequency response is cantilever-specific, we must extract the cantilever-independent dynamics via a calibration of the frequency response to a time constant that describes the transient response of interest (main text Fig. 1c). We collect the relevant cantilever parameters during the trEFM experiment, enabling us to use our model[6] to simulate a t_{fp} to τ calibration curve (Appendix C Fig. 1), which we use to obtain the cantilever-independent equilibration time maps shown in this work.

Appendix C Fig 1. Example simulated calibration curve for extraction of cantilever-independent τ values.

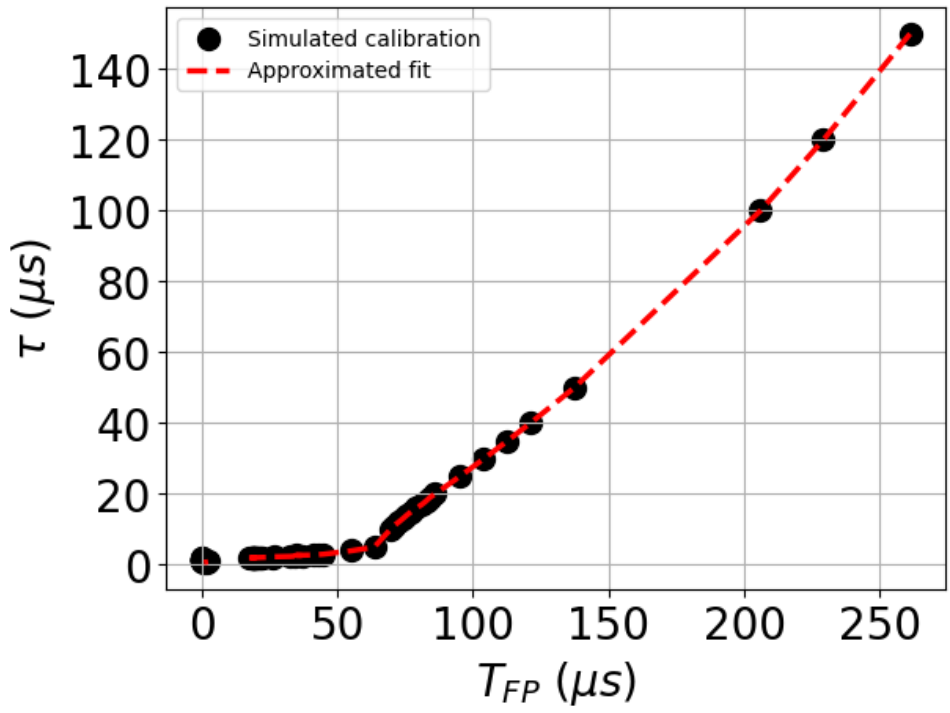

Figure shows characteristic time constant, τ, plotted against time-to-first peak, t_{fp}, obtained from simulation; this calibration curve is used to map experimentally obtained t_{fp} values to cantilever-independent τ values that describe the external force perturbation to the cantilever's oscillation (refer to Appendix C Note 1). We use our publicly available FFTA Python package to generate this calibration curve.[6]

Appendix C Fig 2. Topography of large-scale ROI to correlate trEFM with confocal PL microscopy.

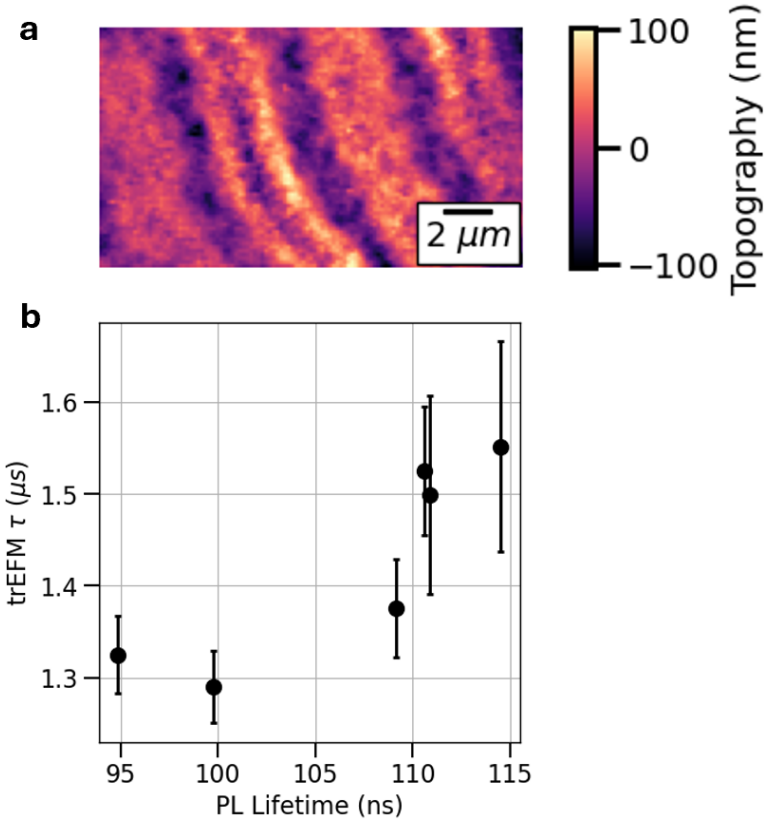

(a) Topography of large-scale ROI shown in main text Fig. 1d-e. **(b)** trEFM surface potential equilibration time constants plotted against trPL lifetimes in correlated regions. trPL lifetimes were collected with using 60× objective, NA=0.7, using a 640 nm laser at a fluence of 105 nJ/cm^2.

Appendix C Note 2. Fitting trPL decays with stretch exponential.

We fit the measured trPL decays using a stretched exponential function as described in **Equation 2** below. The stretched exponential function uses both a characteristic lifetime (τ_C) and a β-factor which describe the time to reach 1/e of the initial signal and the degree of heterogeneity in emitting states, respectively; a β-factor closer to 1 means emission is more homogenous, and the stretched exponential function collapses into a mono-exponential function.[7]

Equation 2.

$$y = \exp\left(-\frac{t}{\tau_C}\right)^{\beta}$$

From the τ_C and β-factor, we calculated the average trPL lifetimes as shown in **Equation 3**; this takes into account the amount of heterogeneity that exists in halide perovskite emission.[7]

Equation 3.

$$< \tau > = \frac{\tau_C}{\beta}\Gamma\left(\frac{1}{\beta}\right)$$

Appendix C Fig 3. UV-vis absorbance and XRD spectra to characterize perovskite half-stack samples and passivations.

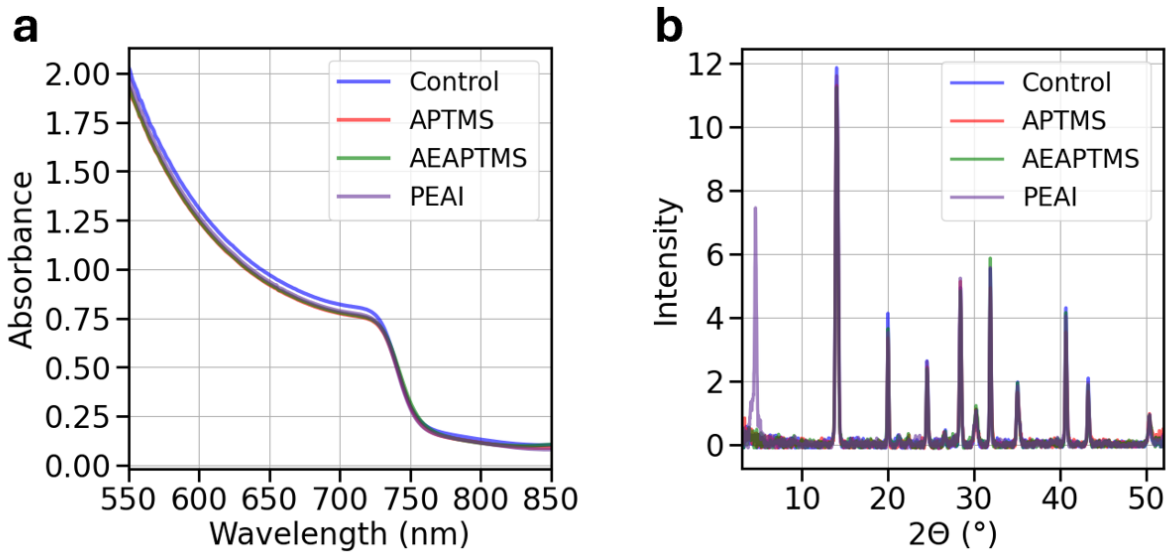

(a) UV-vis absorbance of half-stack samples including the unpassivated control and APTMS-, AEAPTMS-, and PEAI-passivated samples showing negligible change in overall absorbance after passivation. UV-vis characterization protocol described in main text Methods. **(b)** XRD spectra of half-stack samples including the unpassivated control and APTMS-, AEAPTMS-, and PEAI-passivated samples showing negligible change in perovskite diffraction peaks and presence of PEAI salt peak at 4.6°.[8]

Appendix C Fig 4. PL spectra and trPL decays of perovskite half-stacks before and after surface passivation treatments.

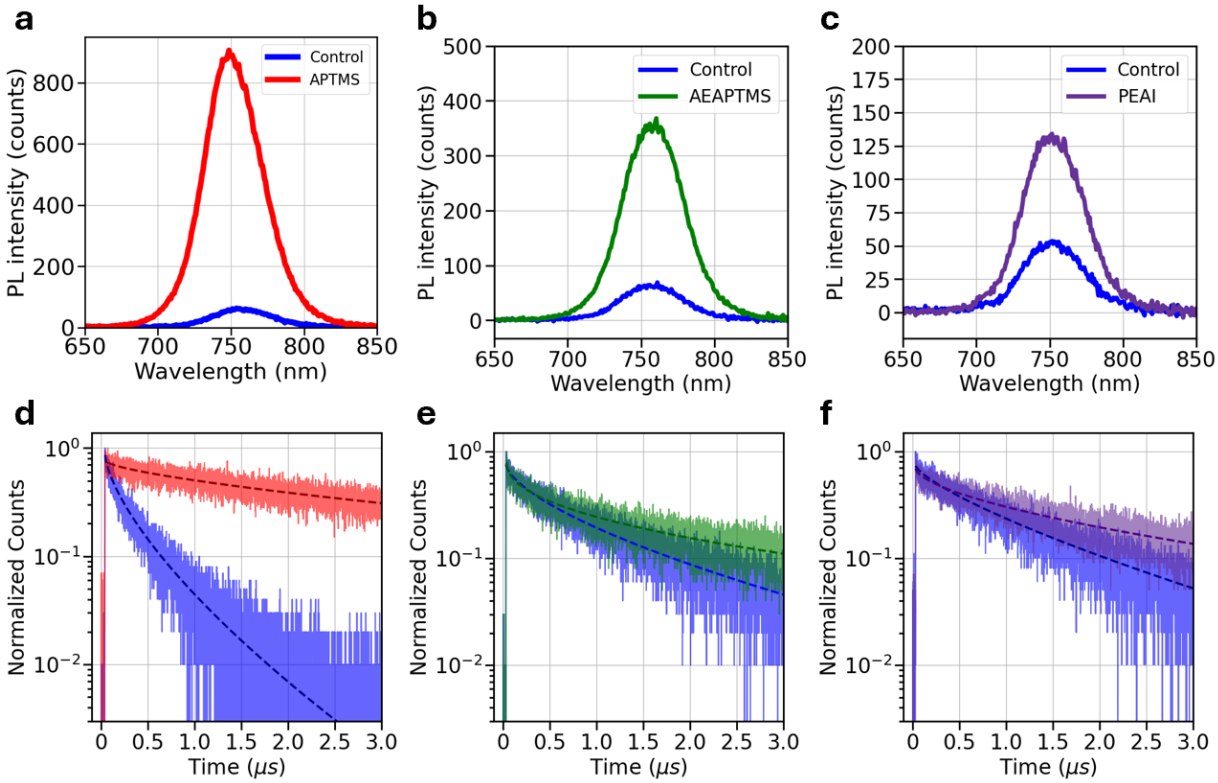

(a)-(c) PL spectra of control and passivated half-stack samples for APTMS, AEAPTMS, and PEAI passivation respectively. **(d)-(f)** trPL decays for control and passivated half-stack samples for APTMS, AEAPTMS, and PEAI passivation respectively.

Appendix C Table 1. Stretched exponential fitting parameters for Glass/ITO/Me-4PACz/$Cs_{0.22}FA_{0.78}Pb(I_{0.85}Br_{0.15})_3$ half-stack samples before and after passivation with AEAPTMS and PEAI.

Sample	τ_C (ns)	β-factor
Control	598	0.64
AEPTMS	684	0.46
Control	814	0.75
PEAI	1335	0.60

Appendix C Fig 5. Photoluminescence quantum yields (PLQY) for control and passivated samples.

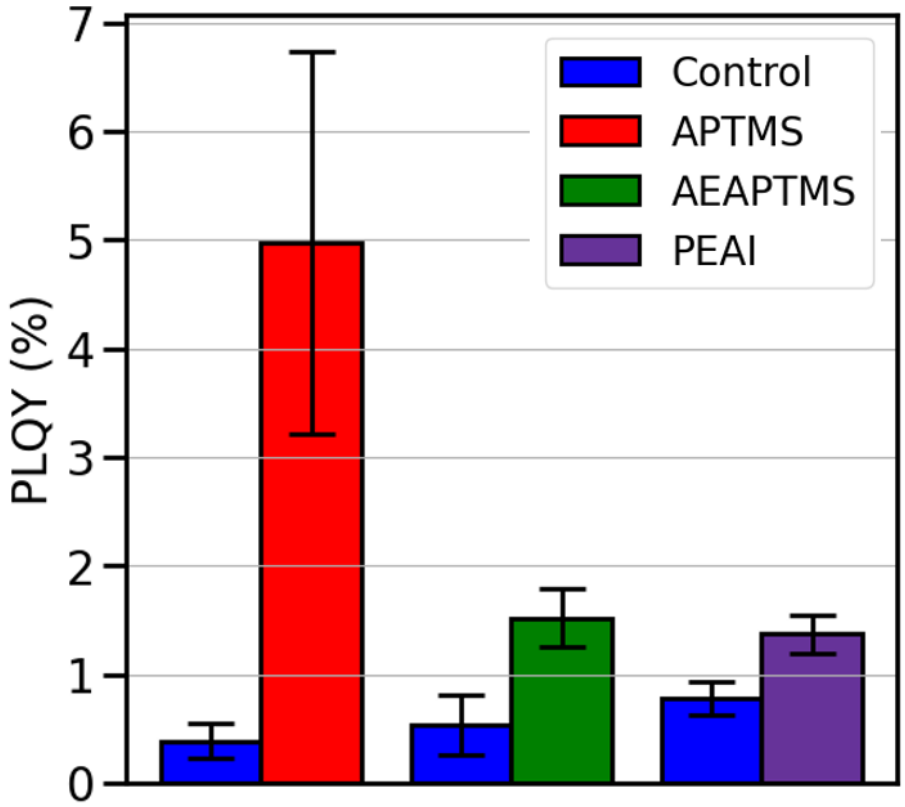

Figure shows PLQY enhancement after passivation with each passivator. The bar represents the average of 3 different samples and the error bars are the standard deviation.

Appendix C Fig 6. trEFM measurements of AEAPTMS and PEAI treatment.

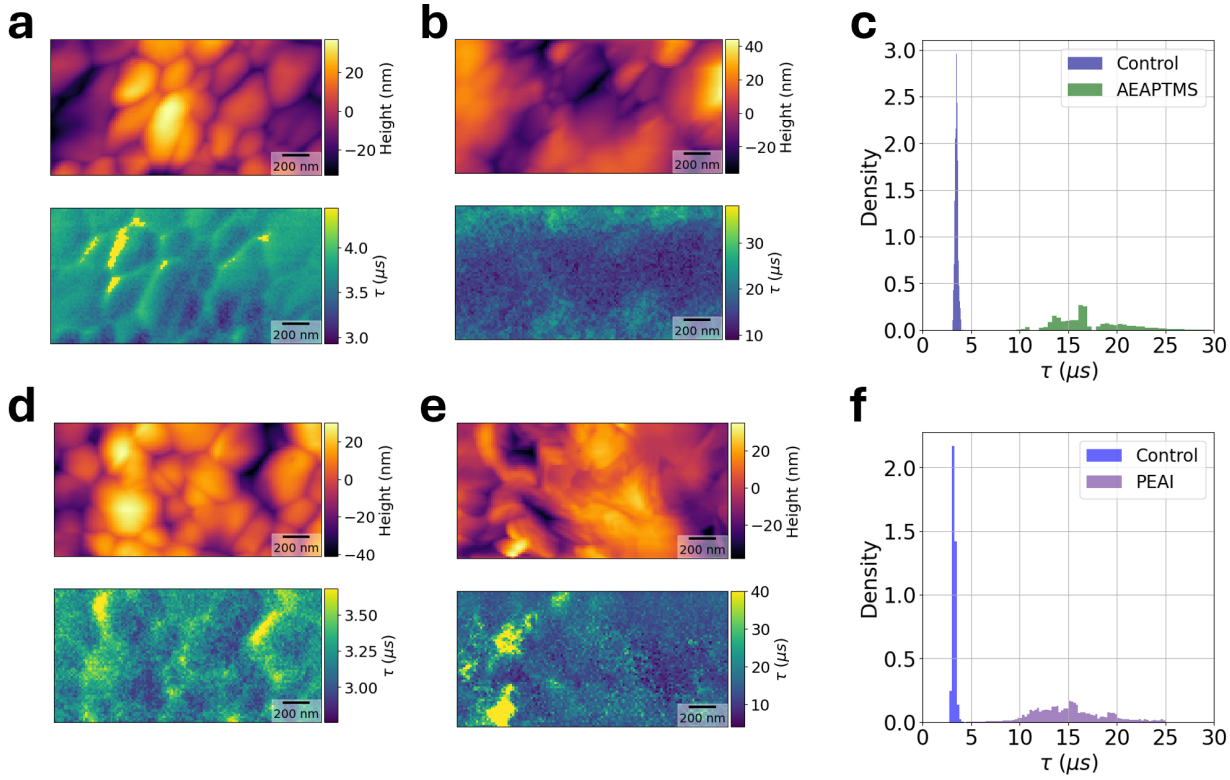

(a) Representative topography and trEFM time constant image of control and **(b)** AEAPTMS treated half-stack samples. **(c)** Associated histogram that shows slower surface potential equilibration times after treatment. **(d)** Representative topography and trEFM time constant image of control and **(e)** PEAI treated samples. **(f)** Associated histogram that also displays slower surface potential equilibration times after treatment.

Appendix C Note 3. Approximation of surface recombination velocity (SRV) from trPL effective lifetimes.

We approximate the SRV at the surface of the perovskite from the trPL measurements using **Equation 4**. Here, τ_{surf}, W, and D describe the carrier lifetime at the surface, the perovskite thickness (500 nm), and electronic carrier diffusion coefficient (assumed to be 0.75 cm^2/s). We can determine τ_{surf} from the effective carrier lifetime (τ_{eff}) and the bulk carrier lifetime (τ_{bulk}) as shown in **Equation 5**. We take the average trPL lifetimes as the τ_{eff} and assume the τ_{bulk} to be 8000 ns and the surface recombination velocity at the perovskite/substrate interface to be negligible, as previous reported.[9,10]

Equation 4.

$$SRV = \frac{W}{\tau_{surf} - \left(\frac{4}{D}\right)\left(\frac{W}{\pi}\right)^2}$$

Equation 5.

$$\tau_{surf} = \left(\frac{1}{\tau_{eff}} - \frac{1}{\tau_{bulk}}\right)^{-1}$$

Appendix C Fig 7. Histograms of the trEFM surface potential equilibration times measured in three ROIs of a control and APTMS-treated $Cs_{0.22}FA_{0.78}Pb(I_{0.85}Br_{0.15})_3$ half-stack sample.

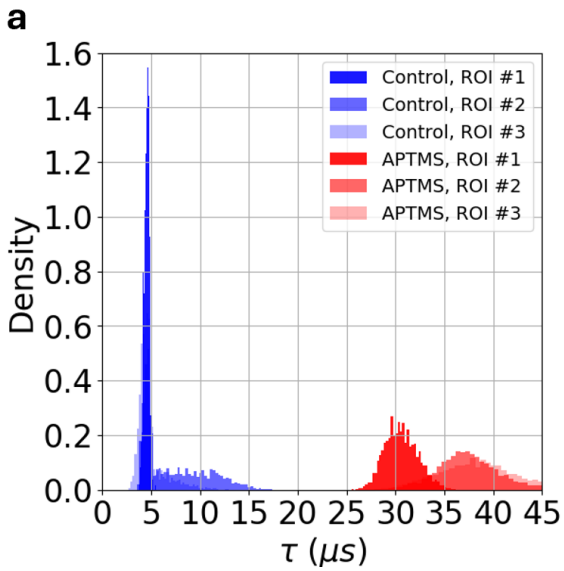

(a) Density normalized histograms showing the trEFM time constants measured across three unique ROIs in a Glass/ITO/Me-4PACz/$Cs_{0.22}FA_{0.78}Pb(I_{0.85}Br_{0.15})_3$ half-stack before and after APTMS treatment. The control and APTMS ROIs are also unique from one another.

Appendix C Table 2. Average values of the trEFM surface potential equilibration times measured in three separate $Cs_{0.22}FA_{0.78}Pb(I_{0.85}Br_{0.15})_3$ half-stack samples before and after APTMS passivation.

Sample	Control <τ> (μs)	APTMS <τ> (μs)
1	10.5	35.0
2	5.4	14.2
3	5.5	35.5

Appendix C Note 4: On surface potential equilibration in perovskite systems as modeled by drift diffusion simulations.

We assume that the surface potential in our simulations is dominated by electronic carrier dynamics because we observe equilibration of the surface potential on the scale of microseconds, while ion migration is typically on the minute timescale (see **Equation 6**).[11,12]

Equation 6.

$$\tau_{ion} = \frac{b}{D_I}\sqrt{\frac{V_T \varepsilon_A}{q\widehat{N}_0}}$$

Where τ_{ion} is the time constant that describes mobile ions migrating to the Debye layers in perovskite thin films, b is the sample thickness, D_I is the ion diffusion coefficient, V_T is the built in voltage, ε_A is the dielectric constant of the absorber, q is the elementary charge, and $\widehat{N}_0$ is the mean cation vacancy density (cation vacancies are assumed to be relatively stationary compared to anion vacancies, and cation vacancy density is assumed to be equal to mean anion vacancy density, so $\widehat{N}_0$ represents mobile ion concentration).[11–13] Given the parameters in **Appendix C Table 3**, ion motion occurs on the scale of several minutes. Because the electric potential in the sample is calculated according to Poisson's Equation ($\frac{d^2\phi}{dt^2} = \frac{q}{\varepsilon_A}\left(\widehat{N}_0 - P + n - p\right)$, where ϕ is potential, P is mobile anion vacancy, n is electron concentration, and p is hole concentration), we can use electronic carrier dynamics to explain the surface potential equilibration timescale. That said, if we increase the concentration of mobile ions (increase $\widehat{N}_0$, because $\widehat{N}_0$= P), we will observe slower surface potential equilibration dynamics due to the proportionally larger contribution from extremely slow ion motion.

We propose that the carrier equilibrium condition can be described by the following set of equations:

Equation 7.

$$G = R = -\frac{dn}{dt}$$

Where G is carrier generation rate, R is carrier recombination rate, n is electronic carrier concentration, and t is time. We describe recombination with the following equation:

Equation 8.

$$R = \frac{1}{\tau_{SRH}}[(n_0 + \Delta n)] + \beta[(n_0 + \Delta n)(p_0 + \Delta p)]$$

Where τ_{SRH} is the nonradiative recombination carrier lifetime, n_0 and p_0 are the electron and hole concentrations in the dark, Δn and Δp are the change in electron and hole concentrations, and β is the bimolecular recombination rate constant. Here, we assume that there is no Auger-Meitner

recombination.[7,11] At the surface, there is an additional recombination term to account for surface recombination velocity, which we describe with the following:

Equation 9.

$$R_{surface} = SRV \times \Delta n$$

Where SRV is the surface recombination velocity at the perovskite/surface interface. Given our electronic carrier equilibrium condition described in **Equation 7** (G = R), carrier concentrations in a sample with a higher SRV term will reach equilibrium at earlier times than a sample with lower SRV.

We fit the surface potential evolution with a tri-exponential function to extract an average time constant to describe the rise time, though we note that this time constant is a phenomenological representation of surface potential equilibration dynamics and the trends should be interpreted as qualitative rather than quantitative in capturing the trEFM experiment.

Appendix C Fig 8. Effects of the nonradiative recombination rate constant on the surface potential equilibration time.

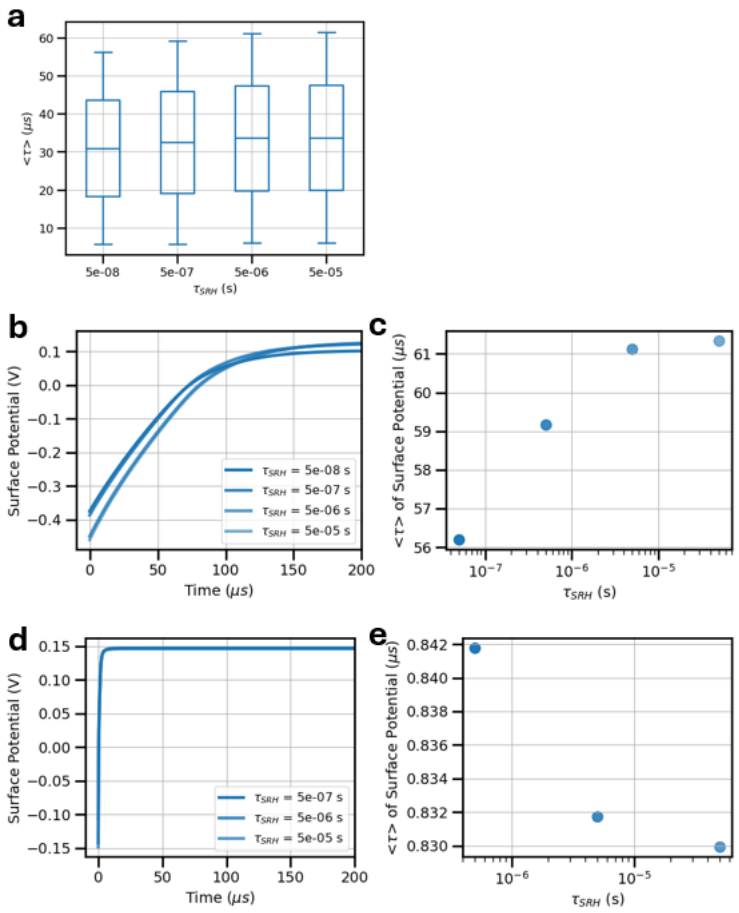

(a) Boxplot showing <τ> values calculated from tri-exponential fits of simulated surface potential traces with 405 nm, 1 mW/cm^2 excitation, showing slight increase in surface potential equilibration time with increasing Shockley Read Hall carrier lifetime (τ_{SRH}); at low fluences, increasing nonradiative recombination lifetime leads to slower equilibration times, which is also shown in **(b)** example surface potential evolutions and **(c)** <τ> fits for those examples; however, at higher excitation intensities like 100 mW/cm^2, τ_{SRH} shows little to no effect on the surface potential equilibration time, as seen in **(d)** and **(e)**. Because τ_{SRH} primarily affects bulk carrier dynamics, we expect that the surface recombination velocity dominates the carrier dynamics at the surface of the absorber. For full simulation details, see Appendix C Table 3, where the primary parameters swept for **(b)-(e)** are τ_{SRH} (s) and illumination intensity (scalar), and all other parameters are held constant. Boxplot mid-line is the median, box edges are the first and third quartiles of the data, and the whiskers show the range of the data.

Appendix C Fig 9. Effects of the bimolecular recombination rate constant on the surface potential equilibration time.

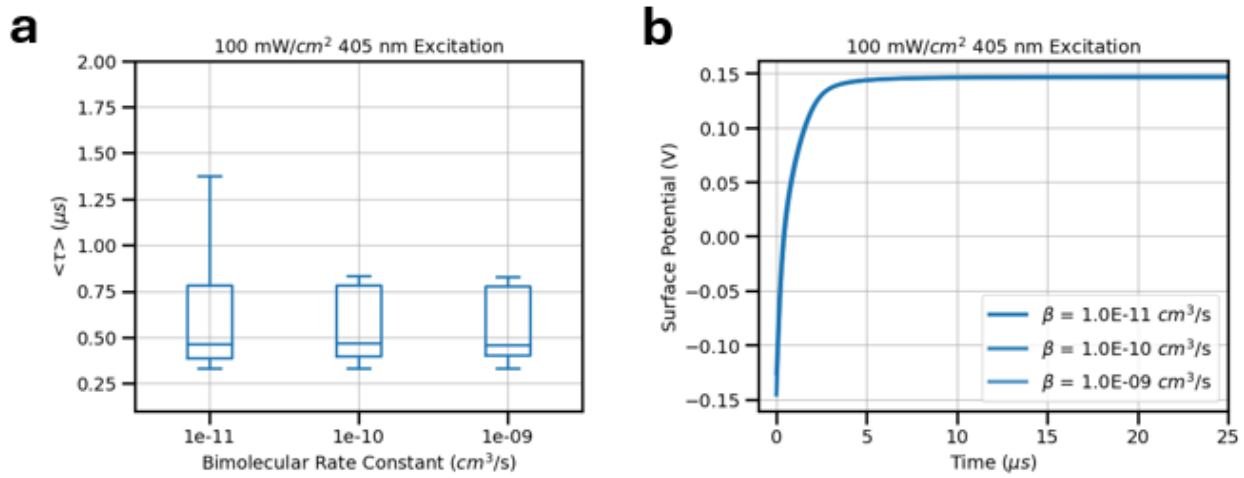

(a) Boxplot showing <τ> values calculated from a tri-exponential fit of simulated surface potential versus bimolecular rate constants, where simulated excitation was 405 nm at 100 mW/cm^2, similar to experimental conditions described in text; **(b)** example surface potential traces with varied bimolecular rate constants for 100 mW/cm^2 405 nm excitation with all other parameters held constant. For full simulation details, see Appendix C Table 3. We recognize that bimolecular recombination rate may be affected by surface passivation,[14] but these simulations show that the bimolecular rate constant has a relatively minor effect on the surface potential evolution. Boxplot mid-line is the median, box edges are the first and third quartiles of the data, and the whiskers show the range of the data.

Appendix C Table 3. IonMonger simulation parameters used to simulate perovskite surface potential evolution.

Parameter	Value(s)	Reference
Thickness	500 nm	N/A
Bandgap	1.7 eV	[11]
Absorption coefficient (α)	405 nm: 2.42085×10^{7} m^{-1} 705 nm: 2.5807×10^{6} m^{-1}	[7]
Photon flux (F_{ph})	405 nm: 2.05×10^{21} $m^{-2}s^{-1}$ 705 nm: 3.55×10^{21} $m^{-2}s^{-1}$	N/A
Illumination Intensity (scalar)	0.01 – 10 (scalar of 1 used for all 100 mW/cm^2 simulations)	N/A
Dielectric constant (ε_A)	$24.1\times\varepsilon_0$ Fm^{-1}	[11,15,16]
Mobile ion concentration (N_0)	1×10^{13} - 1×10^{17} cm^{-3}	[17–23]
Ion diffusion coefficient (D_I)	1×10^{-13} cm^2s^{-1}	[16–23]
Carrier diffusion coefficient (D)	7.5×10^{-3} – 7.5×10^{-1} cm^2s^{-1}	[7,16,24,25]
Nonradiative recombination lifetime (τ_{SRH})	5×10^{-8} - 5×10^{-5} s	[7,24]
Bimolecular recombination rate constant (β)	1×10^{-11} - 1×10^{-9} cm^3s^{-1}	[7,11,15]
Auger-Meitner recombination rate	1×10^{-28} cm^6s^{-1}	[7,15]
Surface recombination velocity (SRV)	1×10^{-1} - 1×10^{3} cm s^{-1}	[7,9–11,15,26]

Appendix C Fig 10. Binary mask used to separate grain interiors and boundaries.

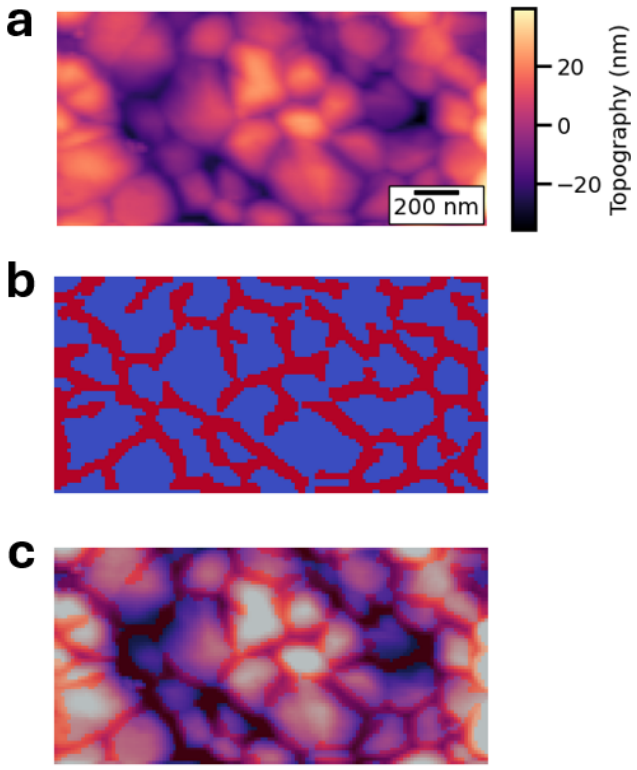

(a) Representative topography of illumination bias region of interest shown in Fig. 4 of the main text; **(b)** binary mask calculated from topography representing grain boundaries (red) and grain interiors (blue); and **(c)** binary mask overlaid on topography.

Appendix C Fig 11. Binary mask used to separate grain interiors and boundaries for second region of interest.

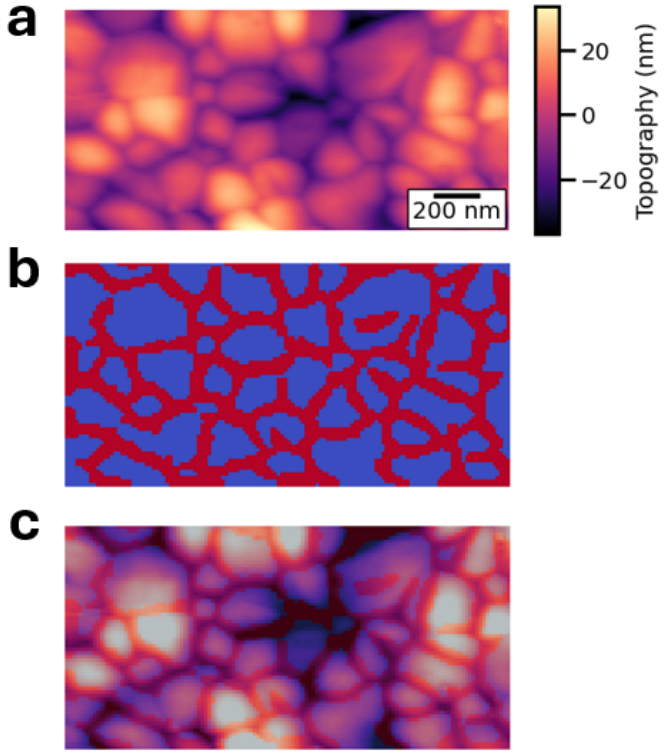

(a) Representative topography of illumination bias *second* region of interest (see Appendix C Fig. 12); **(b)** binary mask calculated from topography representing grain boundaries (red) and grain interiors (blue); and **(c)** binary mask overlaid on topography.

Appendix C Fig 12. Illumination bias data for second region of interest (same illumination conditions as main text Fig. 4).

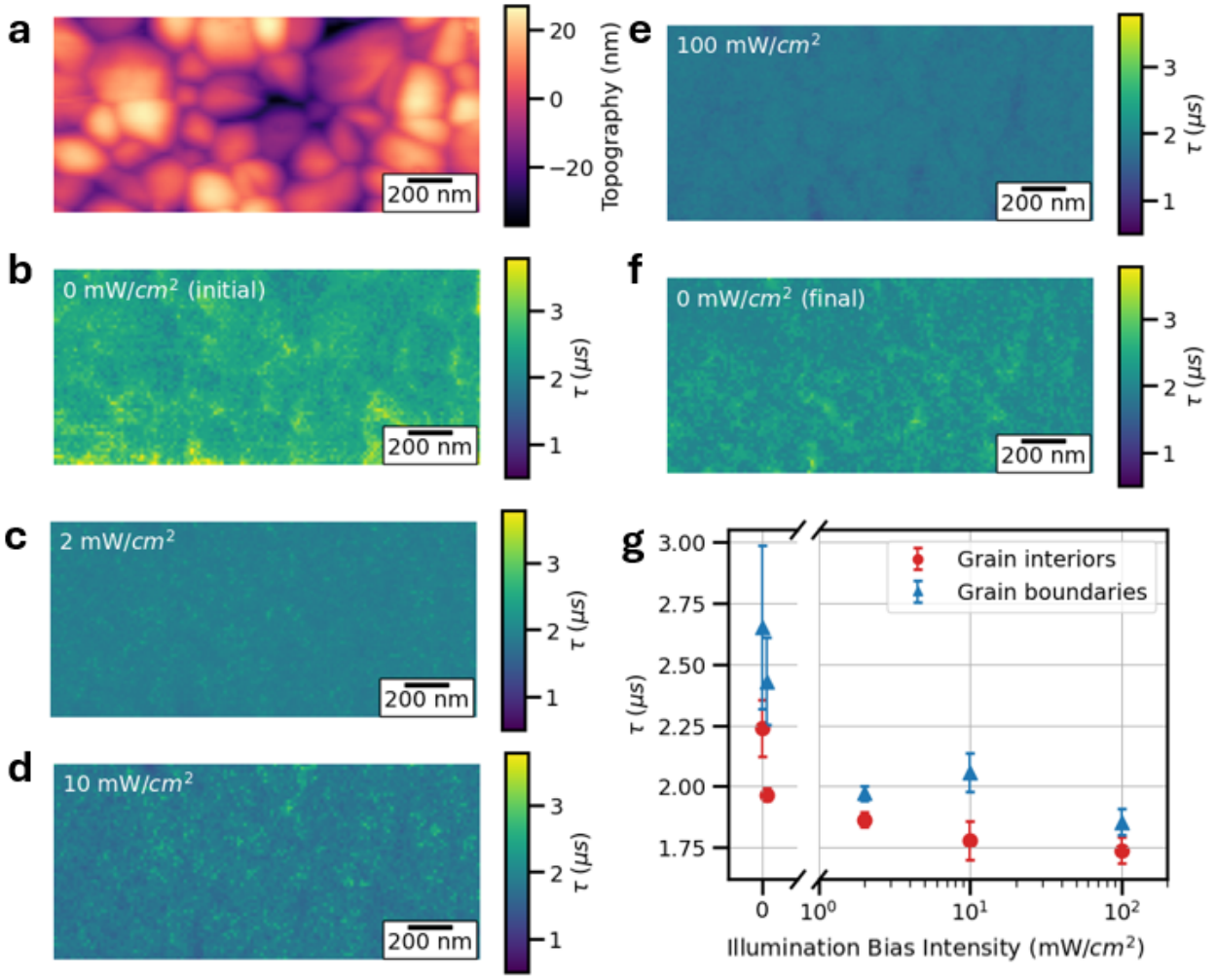

(a) Representative topography of second ROI, showing nanoscale morphology; **(b)-(e)** trEFM surface potential equilibration time images of the same ROI with increasing 660 nm bias illumination intensity ranging from 0 mW/cm2 to 100 mW/cm2, where a fast 405 nm laser at 110 mW/cm2 was used for trEFM excitation; **(f)** reproduced trEFM surface potential equilibration time image at 0 mW/cm2 showing return to unbiased time constants; **(g)** average grain interior and boundary trEFM surface potential equilibration times with respect to illumination bias intensity, error bars show standard deviation of masked pixel selection. Appendix C Fig. 11 shows binary mask used to extract grain boundary and interior data. Mean grain interior trEFM surface potential equilibration times decrease 22.1% at 100 mW/cm^2 with respect to unbiased image, and mean grain boundary trEFM time constants decrease 27.0%.

Appendix C Fig 13. Binary mask used to separate grain interiors and boundaries for third region of interest.

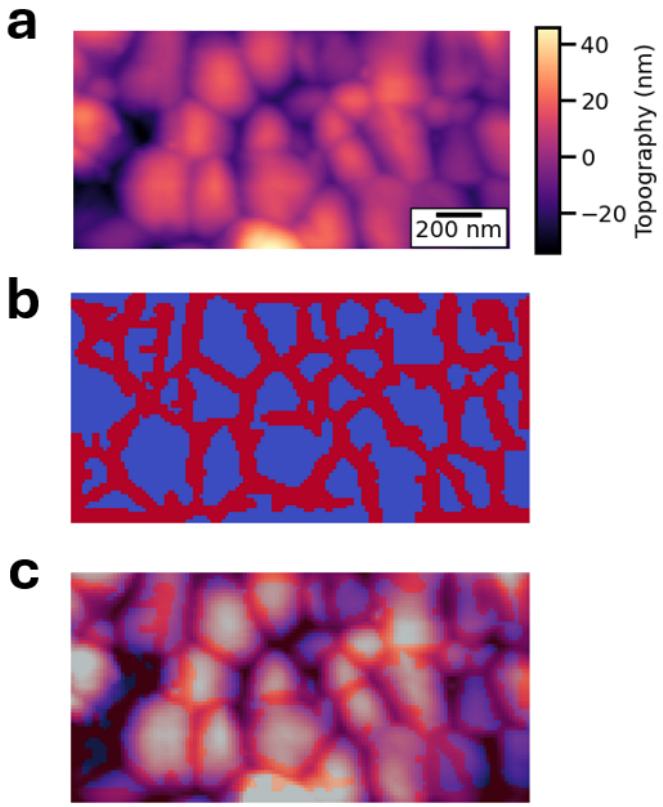

(a) Representative topography of illumination bias *third* region of interest where sample was biased with variable intensity 455 nm light and excited with the fast 405 nm laser (see Appendix C Fig. 14); **(b)** binary mask calculated from topography representing grain boundaries (red) and grain interiors (blue); and **(c)** binary mask overlaid on topography

Appendix C Fig 14. Illumination bias data for third region of interest.

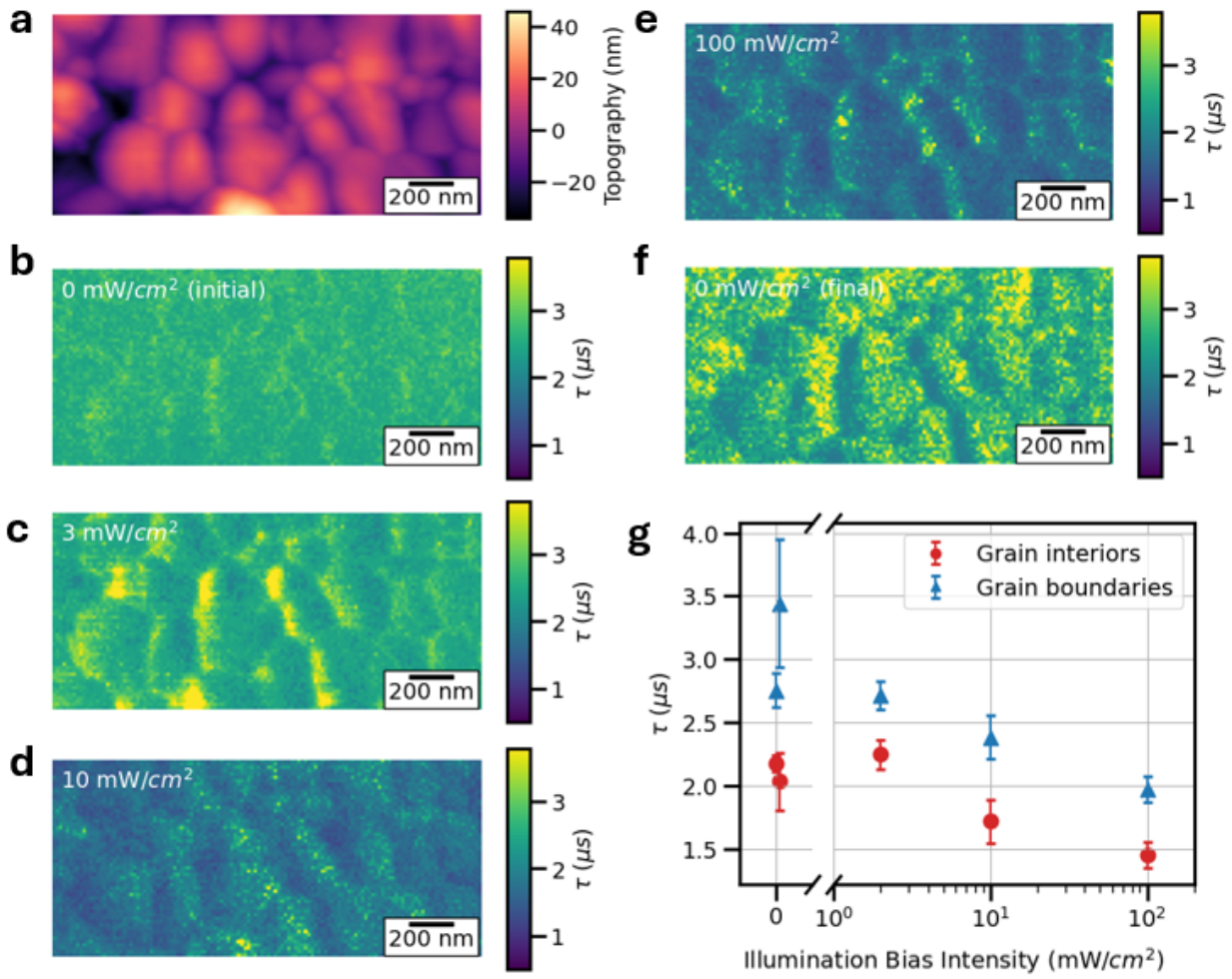

(a) Representative topography of third ROI, showing nanoscale morphology; **(b)-(e)** trEFM surface potential equilibration time images of the same ROI with increasing 455 nm bias illumination intensity ranging from 0 mW/cm2 to 100 mW/cm2, where a fast 405 nm laser at 110 mW/cm2 was used for trEFM excitation; **(f)** reproduced trEFM surface potential equilibration time image at 0 mW/cm2 showing return to unbiased surface potential equilibration times; **(g)** average grain interior and boundary trEFM surface potential equilibration times with respect to background illumination bias intensity, error bars show standard deviation of masked pixel selection. Appendix C Fig. 13 show the mask used for grain boundary and interior analysis. Mean grain interior trEFM surface potential equilibration times decrease 17.6% at 100 mW/cm^2 with respect to unbiased image, and mean grain boundary trEFM surface potential equilibration times decrease 31.2%.

Appendix C Fig 15. Excitation intensity dependent trPL lifetimes.

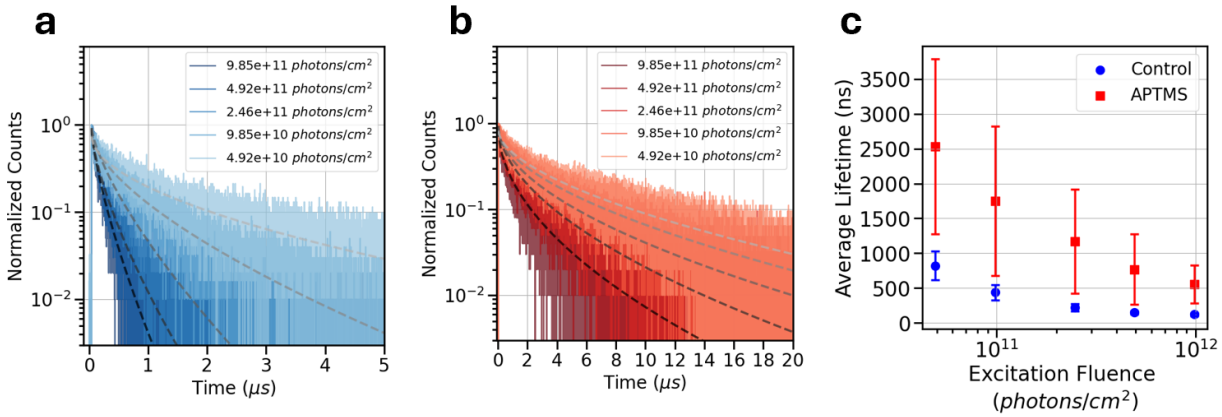

(a) Representative measured trPL decays for a $Cs_{0.22}FA_{0.78}Pb(I_{0.85}Br_{0.15})_3$ half-stacks before and **(b)** after APTMS passivation with varied excitation fluences. Stretched exponential fits are shown with the dashed lines. **(c)** Average trPL lifetime measured as a function of the excitation intensity of a 640 nm laser for a set of $Cs_{0.22}FA_{0.78}Pb(I_{0.85}Br_{0.15})_3$ half-stacks before and after passivation. The average value is calculated from measurements made on three separate samples and the error bars represent the standard deviation of those three samples. See Appendix C Table 4 for fitting parameters. We expect carrier lifetimes to decrease at higher excitation fluences because of the increased contribution of higher order recombination rates.

Appendix C Fig 16. Excitation intensity dependent trEFM measurements.

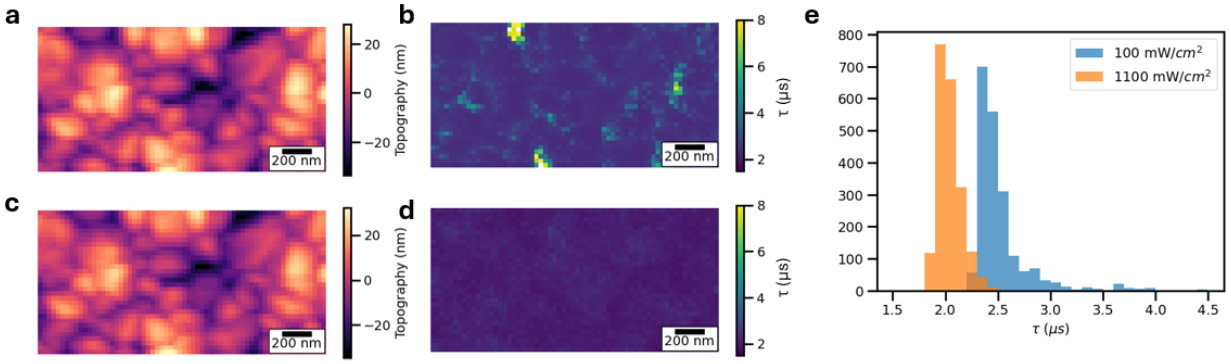

(a) Representative topography of a $Cs_{0.22}FA_{0.78}Pb(I_{0.85}Br_{0.15})_3$ half-stack showing nano-scale grains; **(b)** trEFM surface potential equilibration time map from 100 mW/cm^2 excitation with 405 nm laser showing slower dynamics at grain boundaries, as expected (see main text Fig. 2d); **(c)** topography of the same region of interest; **(d)** trEFM surface potential equilibration time map from image taken with 1100 mW/cm^2 405 nm excitation, showing no observed contrast at grain boundaries and faster dynamics overall; and **(e)** histogram of these two trEFM surface potential equilibration time images validating our observation of faster (and lower contrast) surface potential equilibration dynamics captured with higher excitation intensity; at higher excitation intensity, higher order recombination dynamics have a higher contribution to overall electronic carrier recombination, meaning the sample reaches its equilibrium condition at earlier times. These results are consistent with the trend we observed in intensity dependent carrier lifetimes measured by trPL in Appendix C Fig. 15.

Appendix C Fig 17. IonMonger excitation intensity simulations.

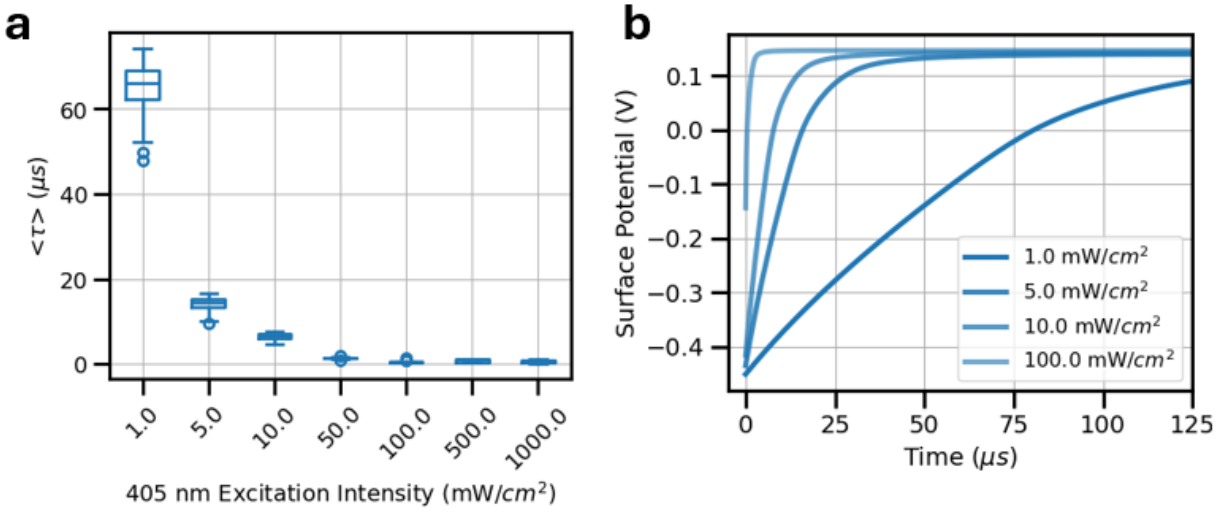

(a) Boxplot showing <τ> values calculated from tri-exponential fits of simulated surface potential dynamics plotted against excitation intensity with 405 nm excitation, showing faster dynamics when absorber is excited with higher intensity light; (b) shows example surface potential traces with varied excitation intensities, demonstrating faster dynamics with higher excitation intensity and validating our experimental observations using trEFM in Appendix C Fig. 16. For full simulation details, see Appendix C Table 3, where primary parameter swept was Illumination Intensity (scalar).

Appendix C Fig 18. Wavelength dependent trEFM measurements.

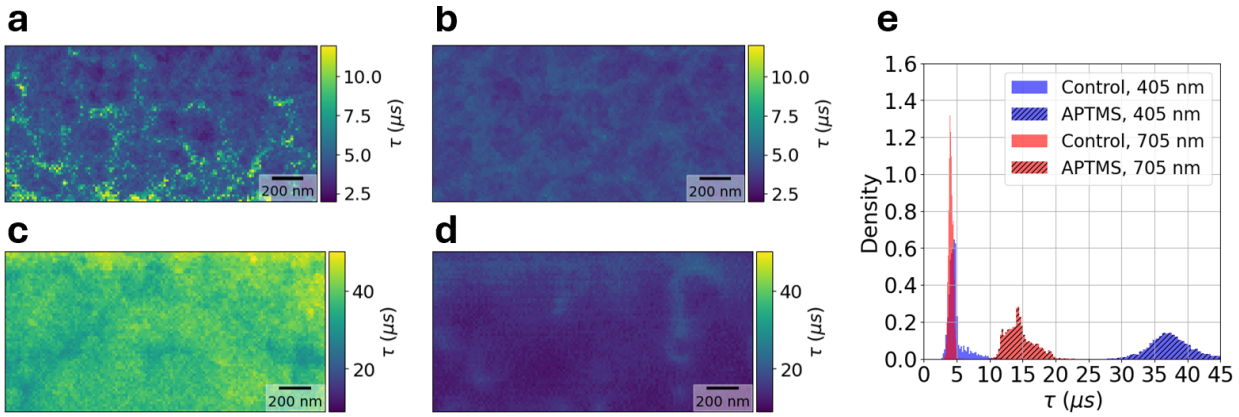

(a) Representative trEFM surface potential equilibration time images for $Cs_{0.22}FA_{0.78}Pb(I_{0.85}Br_{0.15})_3$ control half-stacks excited with 405 nm and **(b)** 705 nm fast lasers. **(c)** Representative trEFM surface potential equilibration time images for APTMS-treated half-stacks excited with 405nm and **(d)** 705 nm fast lasers. All images were collected with an incident intensity of ~150 mW/cm^2. Note that **(a)** and **(b)** share a color bar and **(c)** and **(d)** share a color bar to show the difference observed with different wavelengths. **(e)** Histogram representations of all images where 405 nm excitation, 705 nm excitation, and APTMS-treatment correspond to blue, red, and hashed appearance, respectively. Excitation with 705 nm light yields faster surface potential equilibration times compared to excitation with 405 nm light. We hypothesize since we are exciting the sample through the substrate and measuring the perovskite surface with trEFM, excitation with longer wavelengths results in an increased generation of carriers near the perovskite surface due to a deeper penetration depth, which increases the contribution of SRV to the surface potential equilibration.

Appendix C Fig 19. IonMonger wavelength dependence simulations.

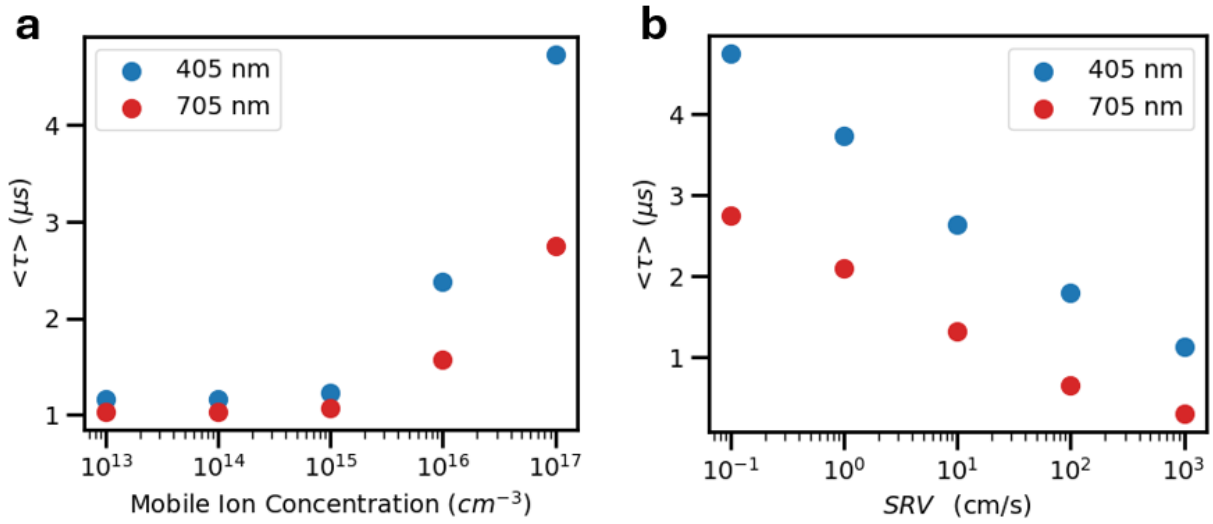

(a) <τ> values calculated from a tri-exponential fit to simulated surface potential evolution, plotted against variable mobile ion concentrations for 405 nm and 705 nm excitation, showing 705 nm excitation consistently results in faster surface equilibration dynamics; and **(b)** showing that at varied surface recombination velocities, 705 nm excitation still results in faster equilibration dynamics than 405 nm excitation. This validates our experimental observations and rationale shown in Appendix C Fig. 18. For full simulation details, see Appendix C Table 3, where the primary parameters swept were mobile ion concentration and surface recombination velocity, with all other parameters held constant.

Appendix C Table 4. Excitation fluence dependent stretched exponential fitting parameters for Glass/ITO/Me-4PACz/$Cs_{0.22}FA_{0.78}Pb(I_{0.85}Br_{0.15})_3$ half-stack samples before and after passivation with APTMS. Representative for Appendix C Fig 15a,b.

Sample, Fluence (photons/cm^2)	τ_C (ns)	β-factor
Control, 9.85e11	92	0.72
Control, 4.92e11	118	0.69
Control, 2.46e11	209	0.72
Control, 9.85e10	390	0.65
Control, 4.92e10	566	0.54
APTMS, 9.85e11	504	0.52
APTMS, 4.92e11	853	0.54
APTMS, 2.46e11	1261	0.54
APTMS, 9.85e10	1929	0.57
APTMS, 4.92e10	2483	0.57

Appendix C Figure 20. Recreation of Figure 1 (main text) using convolutional neural network processing workflow.

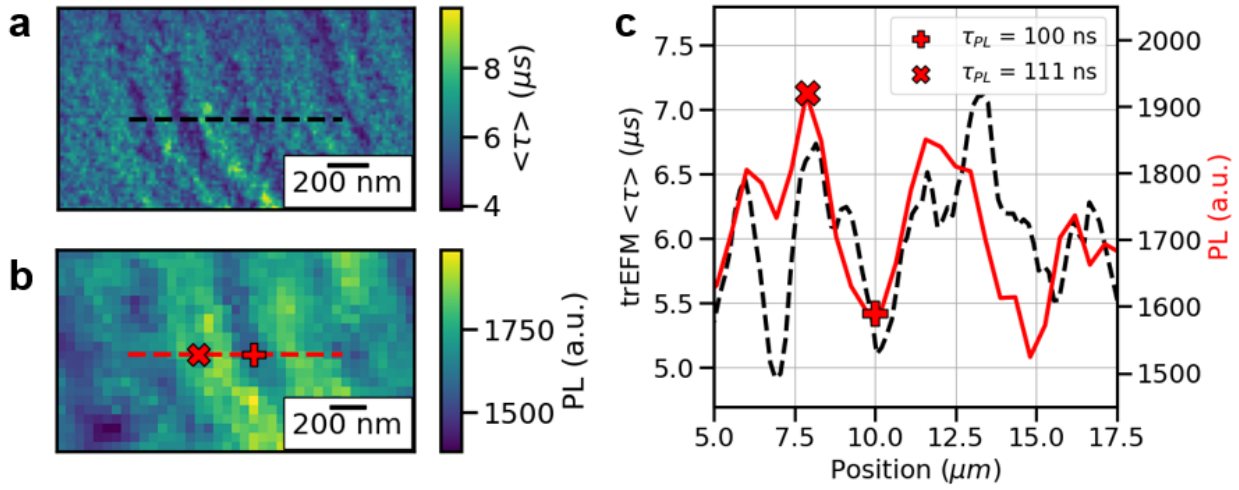

(a) Average trEFM <τ> values (error bars are standard deviation) 17.6×10 μm region of interest collected using 705 nm excitation at an incident intensity of 100 mW/cm^2; black dotted line corresponds to the line trace shown in (c). (b) Correlated PL map of the same ROI, taken using 60× objective, NA=0.7, using a 640 nm laser at a fluence of 105 nJ/cm^2. (c) Correlated line traces from the dotted lines shown in (a) and (b), where the trEFM line trace was smoothed to reduce pixel-to-pixel noise. Markers on (c) indicate positions shown in (b) where time-correlated single photon counting histograms were collected and fit with a stretched exponential (see Appendix C Note 2) to extract carrier lifetimes shown in legend. All <τ> values were obtained by fitting the instantaneous frequency signals at each pixel using a cantilever-independent convolutional neural network as shown in Breshears, et al. (2025).[27] All trends are preserved. We attribute the slight

variation in exact <τ> values to the convolutional neural network's ability to fit slower processes that manifest later in the signal.

Appendix C Figure 21. Recreation of Figure 2 (main text) using convolutional neural network processing workflow.

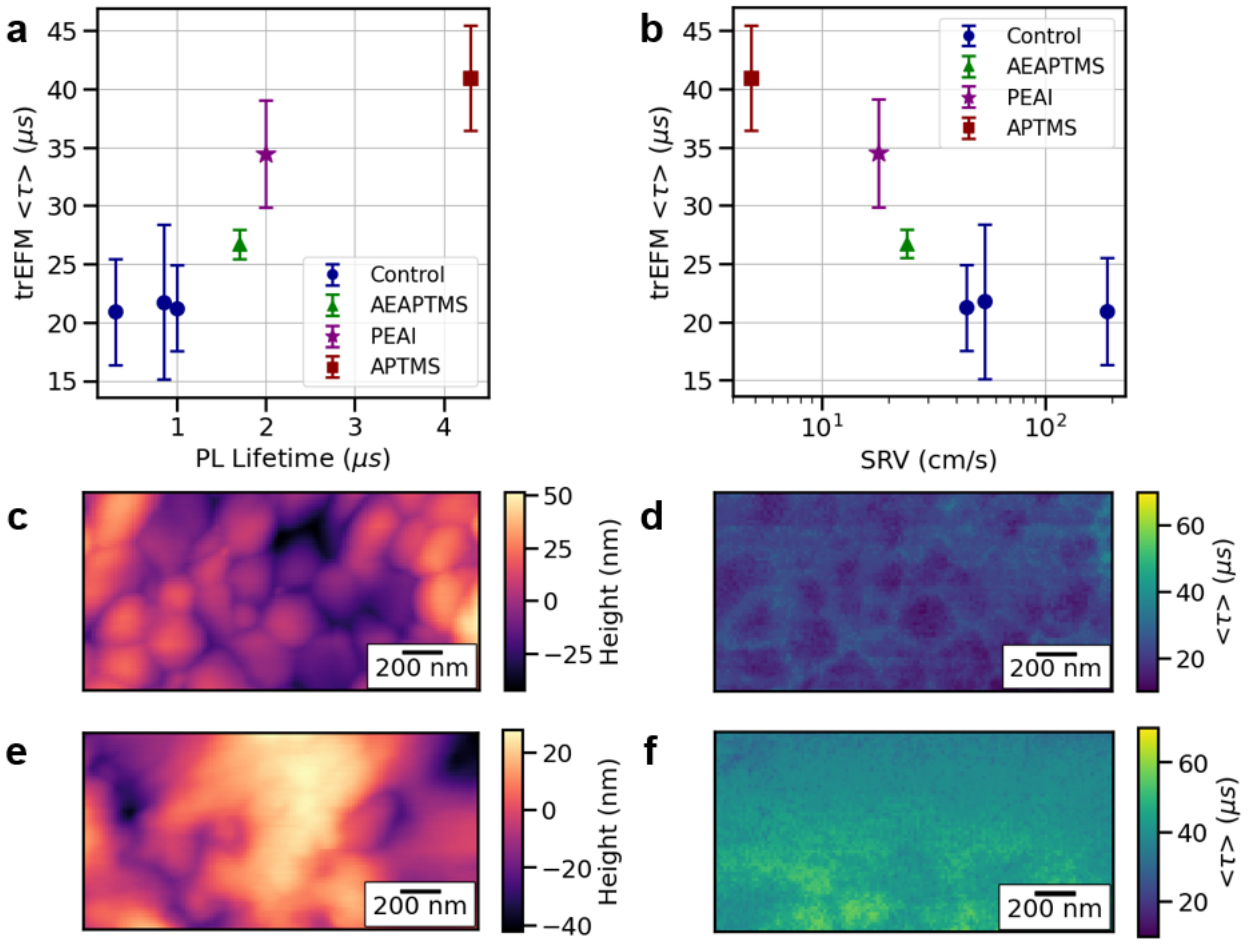

(a) Average trEFM <τ> values (error bars are standard deviation) for control and passivated samples plotted against the PL lifetime as presented in Figure 2 of the main text. (b) Average trEFM <τ> values (error bars are standard deviation) for control and passivated samples plotted against the calculated SRV (see Appendix C Note 3). (c) Topography of unpassivated, control sample showing nanoscale grains, and (d) corresponding trEFM <τ> map. (e) Topography of APTMS-passivated sample and (f) corresponding trEFM <τ> map. All <τ> values were obtained by fitting the instantaneous frequency signals at each pixel using a cantilever-independent convolutional neural network as shown in Breshears, et al. (2025).[27] All trends are preserved. We attribute the slight variation in exact <τ> values to the convolutional neural network's ability to fit slower processes that manifest later in the signal.

Appendix C Figure 22. Recreation of Figure 4 (main text) using convolutional neural network processing workflow.

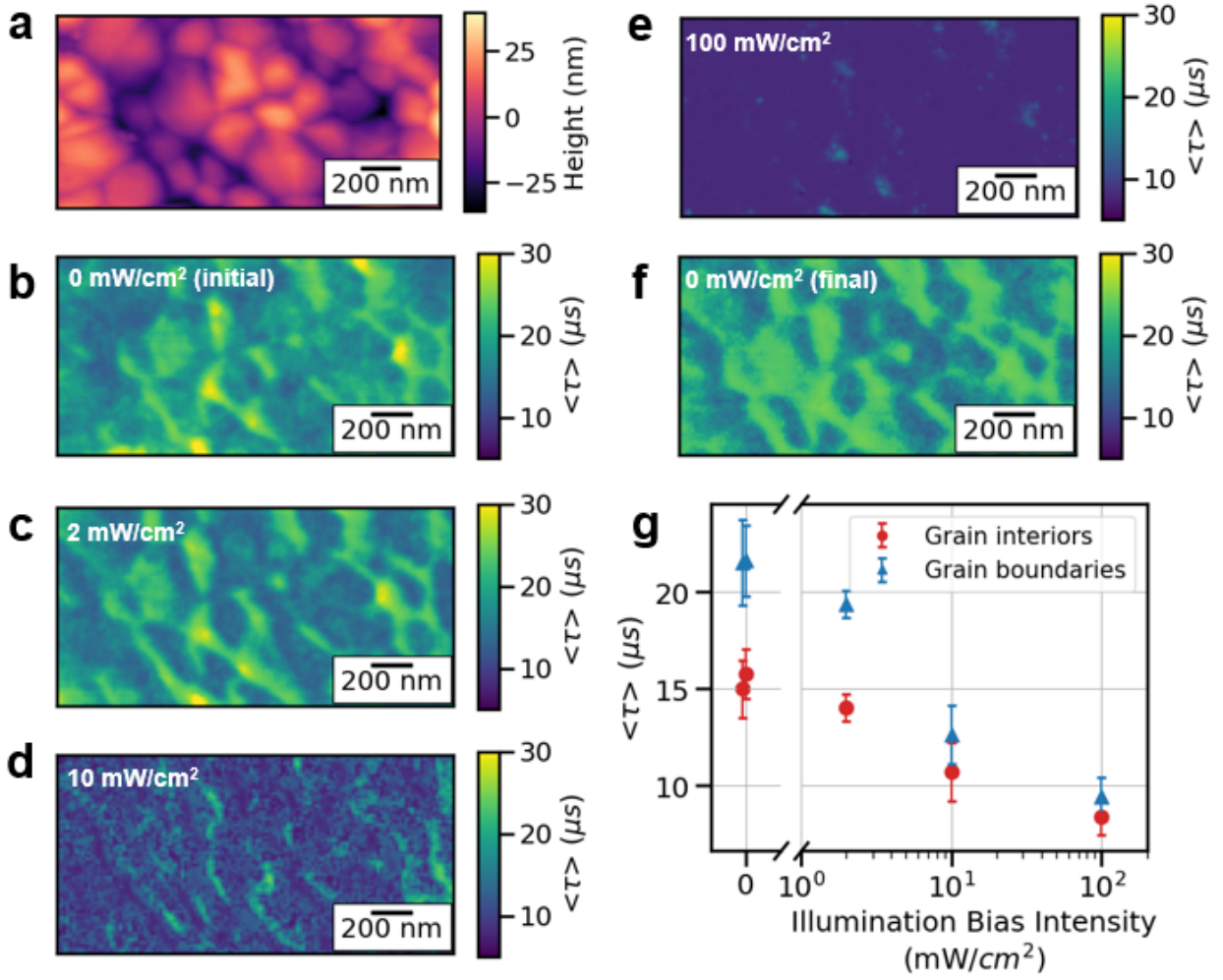

(a) Topography of an unpassivated sample in a 2x1 μm region showing nanoscale grains. (b)-(e) Corresponding trEFM <τ> maps (surface potential equilibration time constants) with additional illumination bias (as described in the main text) with illumination bias intensities ranging from 0 mW/cm^2 to 100 mW/cm^2, with a step-edge 405 nm laser at 110 mW/cm^2 used for trEFM excitation. (f) Reproduced trEFM <τ> image at 0 mW/cm^2 showing return to unbiased time constants and contrast. (g) Average grain interior and boundary trEFM <τ> values with respect to background illumination bias intensity, error bars show standard deviation of masked pixel selection (Appendix C Fig. 10). All <τ> values were obtained by fitting the instantaneous frequency signals at each pixel using a cantilever-independent convolutional neural network as shown in Breshears, et al. (2025).[27] All trends are preserved. We attribute the slight variation in exact <τ> values to the convolutional neural network's ability to fit slower processes that manifest later in the signal.

References.

1. Giridharagopal, R. *et al.* Submicrosecond time resolution atomic force microscopy for probing nanoscale dynamics. *Nano Lett.* **12**, 893–898 (2012).

2. Karatay, D. U., Harrison, J. S., Glaz, M. S., Giridharagopal, R. & Ginger, D. S. Fast time-resolved electrostatic force microscopy: Achieving sub-cycle time resolution. *Rev. Sci. Instrum.* **87**, 053702 (2016).

3. Tirmzi, A. M., Dwyer, R. P., Jiang, F. & Marohn, J. A. Light-Dependent Impedance Spectra and Transient Photoconductivity in a Ruddlesden-Popper 2D Lead-Halide Perovskite Revealed by Electrical Scanned Probe Microscopy and Accompanying Theory. *J. Phys. Chem. C* **124**, 13639–13648 (2020).

4. Shea, D. E., Giridharagopal, R., Ginger, D. S., Brunton, S. L. & Kutz, J. N. Extraction of Instantaneous Frequencies and Amplitudes in Nonstationary Time-Series Data. *IEEE Access* **9**, 83453–83466 (2021).

5. Yazdanian, S. M., Marohn, J. A. & Loring, R. F. Dielectric fluctuations in force microscopy: Noncontact friction and frequency jitter. *J. Chem. Phys.* **128**, 224706 (2008).

6. Rajiv Giridharagopal. FFTA. *GitHub repository, https://github.com/rajgiriUW/ffta* (2021).

7. Taddei, M. *et al.* Interpreting Halide Perovskite Semiconductor Photoluminescence Kinetics. *ACS Energy Lett.* **9**, 2508–2516 (2024).

8. Jiang, Q. *et al.* Surface passivation of perovskite film for efficient solar cells. *Nat. Photonics* **13**, 460–466 (2019).

9. Jariwala, S. *et al.* Reducing surface recombination velocity of methylammonium-free mixed-cation mixed-halide perovskites via surface passivation. *Chem. Mater.* **33**, 5035–5044 (2021).

10. Wang, J. *et al.* Reducing Surface Recombination Velocities at the Electrical Contacts Will Improve Perovskite Photovoltaics. *ACS Energy Lett.* **14**, 222–227 (2019).

11. Courtier, N. E., Cave, · J M, Walker, · A B, Richardson, · G & Foster, · J M. IonMonger: a free and fast planar perovskite solar cell simulator with coupled ion vacancy and charge carrier dynamics. *J Comput Electron* **18**, 1435–1449 (2019).

12. Courtier, N. E., Richardson, G. & Foster, J. M. A fast and robust numerical scheme for solving models of charge carrier transport and ion vacancy motion in perovskite solar cells. *Appl. Math. Model.* **63**, 329–348 (2018).

13. Courtier, N. E., Cave, J. M., Foster, J. M., Walker, A. B. & Richardson, G. How transport layer properties affect perovskite solar cell performance: insights from a coupled charge transport/ion migration model. *Energy Environ. Sci* **12**, 396–409 (2019).

14. Lin, Y. H. *et al.* Bandgap-universal passivation enables stable perovskite solar cells with low photovoltage loss. *Science (1979)* **384**, 767–775 (2024).

15. Riquelme, A. J. *et al.* Understanding equivalent circuits in perovskite solar cells. Insights from drift-diffusion simulation. *Phys. Chem. Chem. Phys* **24**, 15657 (2022).

16. Yang, D., Ming, W., Shi, H., Zhang, L. & Du, M.-H. Fast Diffusion of Native Defects and Impurities in Perovskite Solar Cell Material CH 3 NH 3 PbI 3. **28**, 4349–4357 (2016).

17. Peng, W. *et al.* Quantification of Ionic Diffusion in Lead Halide Perovskite Single Crystals. *ACS Energy Lett.* **3**, 1477–1481 (2018).

18. Futscher, M. H. *et al.* Quantification of ion migration in CH3NH3PbI 3 perovskite solar cells by transient capacitance measurements. *Mater. Horiz.* **6**, 1497–1503 (2019).

19. Mcgovern, L. *et al.* Reduced Barrier for Ion Migration in Mixed-Halide Perovskites. *Appl. Energy Mater.* **4**, 13431–13437 (2021).

20. Yun, J. S. *et al.* Critical Role of Grain Boundaries for Ion Migration in Formamidinium and Methylammonium Lead Halide Perovskite Solar Cells. *Adv. Energy Mater.* **6**, 1600330 (2016).

21. Siekmann, J., Ravishankar, S. & Kirchartz, T. Apparent Defect Densities in Halide Perovskite Thin Films and Single Crystals. *ACS Energy Lett.* **6**, 3244–3251 (2021).

22. Eames, C. *et al.* Ionic transport in hybrid lead iodide perovskite solar cells. *Nat. Commun.* **6**, 7497 (2015).

23. Wu, N., Walter, D., Fell, A., Wu, Y. & Weber, K. The Impact of Mobile Ions on the Steady-State Performance of Perovskite Solar Cells. *J. Phys. Chem. C* **124**, 219–229 (2020).

24. Bertoluzzi, L. *et al.* Mobile Ion Concentration Measurement and Open-Access Band Diagram Simulation Platform for Halide Perovskite Solar Cells. *Joule* **4**, 109–127.

25. Sun, Q., Zhang, X., Zhao, C., Tian, W. & Jin, S. Carrier Transport in Lead Halide Perovskites. *J. Phys. Chem. C* **127**, 22868–22879 (2023).

26. Shi, Y. *et al.* (3-Aminopropyl)trimethoxysilane Surface Passivation Improves Perovskite Solar Cell Performance by Reducing Surface Recombination Velocity. *ACS Energy Lett.* **7**, 4081–4088 (2024).

27. Breshears, M. D., Giridharagopal, R. & Ginger, D. S. Multi-Output Convolutional Neural Network for Improved Parameter Extraction in Time-Resolved Electrostatic Force Microscopy Data. *Preprint* (2025), arXiv:2502.03572.